THE DEVELOPMENT OF

A VIBRATING WIRE VISCOMETER

AND

A MICROWAVE CAVITY RESONATOR

FOR THE MEASUREMENT OF VISCOSITY, DEW POINTS, DENSITY, AND LIQUID VOLUME FRACTION AT HIGH TEMPERATURE AND PRESSURE

A thesis submitted in partial fulfilment of the
requirements for the degree of

Doctor of Philosophy

Mohamed Kandil 2005

ACKNOWLEDGMENTS

This thesis has been made possible by the contribution of many other people not included in this section. However, in these few sentences I can not describe the full effect of the following people on my life and on this thesis.

I am very indebted to my supervisor Professor Ken Marsh who has given me the chance to take part in this intensive and challenging research project. His boundless resources and contacts sustained this project and alleviated many difficult matters, and don't believe him when he says "no no no, that should be easy"… it has never been 'that' easy.

I like to express my sincere appreciation to my associate supervisor Dr Tony Goodwin for his invaluable experience, advice, and exceptional support. The close cooperation with Dr Goodwin has led to different joint publications and initiated sponsorship from Schlumberger Technology Corporation and Schlumberger Oil Phase.

I would like to thank the members of our department especially the technical support team, Mr. Frank Weert, Mr. Bob Gordon, Mr. Trevor Berry, and Mr. Tony Allen who always gave my work a special attention and care. And thanks also to Prof. Bryce E. Williamson, Dept of Chemistry, and Dr Tony Green, Dept of Electrical Engineering, for helping me in setting up the lock-in amplifier and the microwave network analyser used in this project.

I would also like to thank Derek Caudwell for providing support and advice with the programming of the lockin amplifier.

I’m very grateful to Dr Peter Vander Gulik for his guidance and inspiration in designing one of the smallest and accurate vibrating wire viscometers.

Special thanks to Dr Allan Harvey and Dr Eric Lemmon from NIST; Dr Sergei Kiselev, Colorado School of Mines; and Dr Marco Satyro, Virtual Materials Group Inc., for providing important calculations for this thesis.

I would also like to thank Schlumberger Technology Corporation and Schlumberger Oil Phase for their sponsorship and financial support to this project.

I wish to thank my wife Hanan, with love and appreciation. She has been thoughtfully and cheerfully backing me up during a long hard time while I was completing this thesis. I wish I can do more for her, rather than just writing a few words.

Finally, this work is dedicated to our children Salma and Ahmed, challenging them to accept nothing less than their dreams.

SUMMARY

This thesis describes the development and testing of two apparatuses; a vibrating wire viscometer to measure the viscosity of fluids over a wide range of temperature and pressure; and a microwave cavity resonator to measure dew points, gas phase densities, and liquid drop out volumes.

Viscosity and density of downhole fluids are very important properties as their values can determine the economic viability of a petroleum reservoir. A vibrating wire viscometer has been developed with an electrically insulating tensioning mechanism. It has been used with two wires, of diameters (0.05 and 0.150) mm, to measure the viscosity of methylbenzene and two reference fluids with viscosities of (10 and 100) mPa·s at T = 298 K and p = 0.1 MPa, at temperatures in the range (298 to 373) K and pressures up to 40 MPa, where the viscosity covers the range (0.3 to 100) mPa·s, with a standard uncertainty < 0.6 %. The results differ from literature values by < ± 1 %. The results demonstrate that increasing the wire diameter increases the upper operating viscosity range of the vibrating wire viscometer, a result anticipated from the working equations.

For the microwave cavity resonator, the method is based on the measurements of the resonance frequency of the lowest order inductive-capacitance mode. The apparatus is capable of operating at temperatures up to 473 K and pressures below 20 MPa. This instrument has been used

to measure the dew pressures of {0.4026CH_4 + 0.5974C_3H_8} at a temperature range from 315 K up to the cricondentherm ≈ 340 K. The measured dew pressures differ by less than 0.5 % from values obtained by interpolation of those reported in the literature, which were determined from measurements with experimental techniques that have quite different potential sources of systematic error than the radio-frequency resonator used here. Dew pressures estimated from both NIST 14 and the Peng-Robinson equation of state lie within < ± 1 % of the present results at temperature between (315 and 337) K while predictions obtained from the Soave-Redlich-Kwong cubic equation of state deviate from our results by 0.4 % at T = 315 K and these differences increase smoothly with increasing temperature to be –2.4 % at T = 337 K.

Densities derived from dielectric permittivity measurements in the gas phase lie within < 0.6 % of the values calculated from the Soave-Redlich-Kwong cubic equation of state and about 1 % from values obtained with the Harvey and Prausnitz correlation based on a mixture reduced density. The calculations with Kiselev and Ely parametric crossover equation of state (based on Patel-Teja EOS) gave deviations < 0.7 %.

Liquid volume fractions, in the 2-phase region, were measured from (0.5 to 7) cm^3 in a total volume of about 50 cm^3 at different isochors. The measured liquid volume fractions differ from values obtained with the Soave-Redlich-Kwong cubic equation of state by between 0 and 3 % at T <

326 K and about 8 % on approach to the critical region. The large deviations observed in the critical region were anticipated because of the known poor performance of the cubic equations of state with regard to the calculation of the liquid density in the vicinity of the critical temperature.

TABLE OF CONTENTS

PART I: The Vibrating Wire Viscometer

PART II: The Microwave Cavity Resonator

LIST OF FIGURES:

LIST OF TABLES

Chapter 1

GENERAL INTRODUCTION

1.1 Thesis layout:

For the sake of clarity, this thesis has been ordered in three discrete parts: (I), is specific to the vibrating wire viscometer; (II), is specific to the cavity resonator; and (III), includes conclusions and recommendations, references and bibliography, and published papers on this work. Chapter 1 gives a general introduction and a brief history to the project. References for the cavity resonator were kept in a contiguous order, starting from ref [93].

1.2 Aim and a brief history:

This thesis describes the development of two novel instruments; a vibrating wire viscometer, and a microwave cavity resonator. The vibrating wire viscometer developed in this project was used to measure the viscosity of methylbenzene and two standard fluids at η up to 200 mPa·s at temperature between (298 to 373) K and pressure up to 40 MPa, while the microwave cavity resonator was used to measure the dew points, dielectric permittivity, gas phase density, and liquid volume fractions for a methane + propane mixture at temperature between (315 to 345) K and pressure up to 7 MPa.

This project was first started, in 2000, with the idea of applying these devices to measurements on hydrofluorocarbon refrigerants (HFC) and their compatible lubricants. The limited solubility of the HFC refrigerants in mineral oils, traditionally used with chlorofluorocarbons (CFC), has led to the introduction of new synthetic lubricants for refrigeration use; hence, it was deemed essential to obtain data on those replacement refrigerants and their recently developed synthetic lubricants oils. Therefore, the International Union of Pure and Applied Chemistry (IUPAC) Thermodynamics Commission Task Group and the Thermophysical Properties Division of NIST had identified that the properties of mixtures of lubricants with replacement HFC refrigerants should be a high priority research area, and that there was a need to develop methods to predict compatibility regimes and properties. It was planned to use the apparatus to study the separation of the oils from the (HFC refrigerant + mineral oil) mixture under evaporator conditions. If the oil migrates in small quantities from the compressor reservoir to the condenser then to the evaporator, where it could separate and accumulate, the compressor becomes starved for oil and a break down is possible. The use of synthetic oils has solved this problem because they are more soluble in HFC, but they create other serious problems because, as explained in details by Kandil and Marsh [1], most of them are hygroscopic and, besides, their cost is high compared to mineral oils. In particular, the measurement of the liquid drop out volume was expected to provide accurate data for the separation behaviour, in

addition to the measurements of density, dew points, and relative permittivity. Moreover, the vibrating wire viscometer was expected to be suitable for obtaining high quality data over a wide range of temperature and pressure for synthetic oils and their mixtures with HFC's.

The study of these refrigeration fluids extended for almost one year and a thorough literature review [1] was published on this subject. However, the project moved in a different direction when sponsorship was received from Schlumberger and measurements were conducted on (methane + propane), methylbenzene, and two certified reference materials for viscosity. Two papers have been published on these fluids [2, 3] and one more paper is under preparation as discussed in the conclusions chapter.

1.3 Viscosity measurements:

1.3.1 Methods of measurements:

There are numerous methods by which viscosity can be measured, and these have been reviewed in detail in ref [4] where they are grouped into 4 types: capillary, falling body, oscillating body, and vibrating viscometers. Most viscometers of the first two types, capillary and falling body viscometers, are considered 'absolute' viscometers, which mean they rely on rigorous working equations. However, they still require calibration with a fluid with known viscosity at a specified temperature and pressure in order to determine correction factors included in the equations. These factors correct for effects that could contribute systematic errors to the

measurements. These include the kinetic energy effect and the end effect in the capillary viscometers, and also wall effects in falling body viscometers. This limits their accuracy in absolute viscosity measurements (if no calibration made) to ±3 %, however, they can provide considerably more accurate measurements when suitably calibrated. Capillary viscometers are the most used type due to their simple design and operation.

On the other hand, oscillating body and vibrating object viscometers do not require correction factors because under specific restraints the working equations are complete. A measurement in vacuum is used to determine the 'self' damping of these viscometers. As shown in Table 1.1, the oscillating body and vibrating object viscometers can also, simultaneously, measure density. Indeed, these devices have simple electrical circuits and are easy to automate.

Table 1.1: Qualities of the main absolute viscometer types. CP = capillary, FB = falling body, OB = oscillating body, VV= vibrating viscometers.

Criterion	CP	FB	OB	VV
suitable for gases	yes	no	yes	yes
measure density	no	no	yes	yes
correction factors	yes	yes	no	no
calibration fluid	yes	yes	no[†]	no[†]
design	simple	complex	complex	simple
equation	simple	simple	complex	simple
automation	complex	complex	simple	simple
sample size	larger	larger	smaller	smaller

[†] require a measurement in vacuum to determine the self damping.

Vibrating wires are of simple construction and have working equations that are relatively simpler than those for oscillating body viscometers. They also require a significantly smaller fluid volume than traditional methods, and do not require bulk motion of the fluid, and hence they are compact. The well-founded underlying equations with clear practical constraints hold up the vibrating wire as a primary viscometer providing measurements with an uncertainty 'claimed' as less than 0.3 %.

Vibrating wire viscometers have been used for measurements on a wide range of fluids over an extended range of temperature and pressure. As shown in Table 2.1, vibrating wire viscometers have been used to measure viscosities ranging from (0.009 to 200) mPa·s in both liquids and gases over a temperature range from 1.1 K [57] up to 455 K [16], and at pressures up to 1 GPa [50].

1.3.2 Concept of Viscosity:

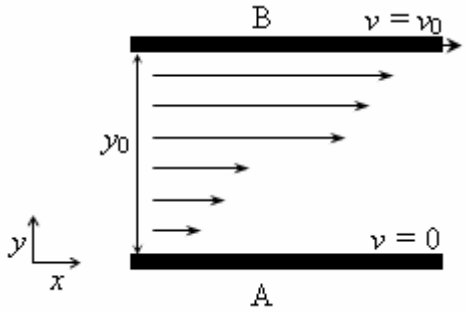

Figure 1.1: Sketch showing the velocity gradient in a fluid contained between one stationary plate and another moving plate with velocity v_0.

Viscosity describes the extent to which the relative motion of adjacent fluid layers are retarded in response to deformation of the fluid. It represents the dissipative (irreversible) portion of the dynamic response, unlike Young's modulus which represents the elastic or recoverable part of the response.

The viscosity can be demonstrated by suspending two horizontal, parallel plates A and B, as shown in Figure 1.1, in a liquid so that they are separated by a very small distance y_0. If the lower plate is kept stationary while the upper plate is moved in the x-direction with velocity v_0 the layer of liquid next to this plate will also start to move. At steady-state conditions, as shown in Figure 1.1, the velocity of the fluid layer in contact with the stationary plate A will also be zero, while the uppermost layer, in contact with the moving plate B, will be moving with velocity v_0. The velocity distribution across the intermediate fluid layers changes linearly with the distance y from the stationary plate according to:

$$v = v_0 \frac{y}{y_0}. \tag{1.1}$$

The shear stress $\tau_{y,x}$ obtained by dividing the horizontal force (applied in the opposite direction to maintain the lower plate stationary) by the surface area of the plate, is proportional to the velocity of the upper plate, and inversely proportional to the distance between the two plates, and is given by:

$$\tau_{y,x} = -\eta \frac{dv_x}{dy}, \tag{1.2}$$

which is known as Newton's Law of viscosity. The subscript *y* on the shear stress denotes the area over which the shear stress acts (an area perpendicular to the y-axis and at a distance *y* from the origin); the second subscript *x* represents the direction in which the shear stress acts. The negative sign expresses the fact that the shear stress is applied from a region of higher velocity to a lower one.

By dividing and multiplying the second term of eq 1.2 by the fluid density ρ gives:

$$\tau_{y,x} = -\frac{\eta}{\rho}\left(\frac{\rho dv_x}{dy}\right), \tag{1.3}$$

and for incompressible fluid flow:

$$\tau_{y,x} = -\frac{\eta}{\rho}\left(\frac{d\rho v_x}{dy}\right), \tag{1.4}$$

which shows momentum flux is proportional to the negative value of the gradient of mass flux,

$$\tau_{y,x} = -\nu\left(\frac{d\rho v_x}{dy}\right), \tag{1.5}$$

where $\nu = \eta/\rho$ is the kinematic viscosity that, by analogy, can be referred to as the momentum diffusivity of the fluid, i.e. the ability of the fluid to transport momentum.

Thus, viscosity is the principal factor resisting motion in laminar flow. However, when the velocity is increased to a turbulent flow regime, pressure differences resulting from eddy currents rather than viscosity provide the major resistance to motion. Fluids that perform in this manner, called non-Newtonian fluids, are not considered further in this study and details can be found in Holland and Bragg [5].

1.3.3 Viscosity correlation for methylbenzene:

Methylbenzene was used in this project because it is widely accepted as an alternative reference liquid to water. Its wide temperature range in the liquid phase (178 to 384) K makes it an ideal reference liquid for viscosity calibration purposes. The International Association for Transport Properties (IATP) has recommended the use of methylbenzene as a reference fluid in viscosity measurements. It has also been used widely by different research groups, and a reference correlation for viscosity and density was reported by Assael et al. [23]. This correlation covers the temperature range from (213 to 373) K at pressures up to 250 MPa encompassing the ranges used in this project.

Since the viscosity of methylbenzene is a function of density, a Tait-type equation was used from [23] to correlate the density as:

$$\rho = \rho_0 \left\{ 1 - C \log_{10} \left(\frac{B + p/\mathrm{MPa}}{B + p_0/\mathrm{MPa}} \right) \right\}^{-1}, \tag{1.6}$$

where $p_0 = 0.1$ MPa, C is a constant, and ρ_0 and B are given by:

$$\rho_0 = \sum_{i=0}^{2} a_i (T)^i, \tag{1.7}$$

and

$$\mathrm{B} = \sum_{i=0}^{3} b_i \Theta^i, \tag{1.8}$$

where Θ = 1- (T/T_c), and T_c = 591.8 K is the critical temperature of methylbenzene [23]. The viscosity correlation reported by Assael et al [23] is an optimised version of a hard-sphere equation developed by Assael et al. and reported in a series of 5 papers [6, 7, 8, 9, 10], where the viscosity coefficient η is given by:

$$\eta = \eta^* \left\{ 6.035 \cdot 10^8 V^{2/3} (MRT)^{-0.5} \right\}^{-1} \tag{1.9}$$

where V is the molar volume, M is the molar mass (M = 0.09214 kg·mol^{-1}), R the gas constant (R = 0.831447 MPa·cm^3·mol^{-1}·K^{-1}), and η^* is a dimensionless viscosity given by:

$$\frac{1}{\eta^*} = \sum_{i=0}^{3} d_i \left(\frac{V}{V_0} \right)^i , \tag{1.10}$$

In eq 1.10, the characteristic molar volume V_0 is given as function of temperature T by:

$$V_0 \cdot 10^6 = \sum_{i=0}^{3} e_i T^i . \tag{1.11}$$

The parameters of eqs 1.6 to 1.11 are given in Table 1.2.

Table 1.2: Parameters for methylbenzene equations of density and viscosity

parameters	value
a_0/ kg·m^{-3}	1188.631
a_2/ kg·m^{-3}·K^{-1}	-1.49777
a_2/ kg·m^{-3}·K^{-2}	0.002158
a_3/ kg·m^{-3}·K^{-3}	-2.69·10^{-6}
b_0	-4.1
b_1	82.4043
b_2	198.1896
b_3	-6.61293
b_4	307.6237
C	0.216
d_0	0.524367
d_1	-1.34765
d_2	1.081113
d_3	-0.25609
e_0/ m^3·mol^{-1}	129.770
e_1/ m^3·mol^{-1}·K^{-1}	-0.2793623
e_2/ m^3·mol^{-1}·K^{-2}	6.7699·10^{-4}
e_3/ m^3·mol^{-1}·K^{-3}	-6.36347·10^{-7}

1.4 *VLE* measurements:

The optimal recovery of naturally occurring hydrocarbons mixtures depends on a knowledge of the physical properties of the porous media and the fluid contained within, including its phase boundaries, density, and viscosity. Dew and bubble temperatures can be determined experimentally or estimated with an equation of state; the latter requiring as input temperature, pressure and chemical composition, which may be obtained from gas chromatography coupled to a mass spectrometer. For retrograde condensates (or natural gas) the dew temperature curve and ratio of liquid-to-gas volumes within the (liquid + gas) two-phase region, often referred to as the quality line, are the most significant thermodynamic properties for the exploitation of natural hydrocarbons. For multi-component mixtures, predicted dew pressures near the critical region are often considered unreliable and need to be measured. In this project, the dew points, density of gas phase, and liquid volume fractions of (gas + liquid) phase, were measured for the mixture $\{0.4026CH_4 + 0.5974C_3H_8\}$. The range of measurements extended to temperatures close to the cricondentherm and the results have been compared with different equations of state (EOS).

1.4.1 General methods of measurements:

Experimentally, dew curves are often determined by visual observation of the first onset of liquid condesation. Often, but not always, the techniques used by industry to determine dew points have volumes of about 1 L.

Although the results obtained from visual methods are known to suffer systematic errors that arise from blind regions and dead volumes, and these sources of error have, to a lesser or greater extent, been reduced by refinements to the method, the visual method remains the most prevalent in the petroleum industry. Non-visual methods, that require small (<100 cm^3) samples and are particularly suited to automation, have been developed to determine the presence of a phase transition. These include measurements of refractive index by employing fibre-optic cables [93], evanescent waves at GHz frequencies [94], and relative permittivity [95,96,97,98]. The latter, determined with a radio frequency (RF) cavity resonator, was previously used by Goodwin et al. [98] to determine phase behaviour and is the subject of this work.

The most important features of this technique are: (1) on-line measurements can be made; (2) microwaves can penetrate all fluids (depending on their electrical conductivity) giving representation to the volume not only the surface; (3) it provides higher resolution and sensitivity with temperature changes compared to other techniques. However, calibration with a reference material is necessary to compensate for changes in dimensions of the cavity with pressure and temperature.

1.4.2 RF/microwave resonator:

The term Radio Frequency (RF) refers to a wide portion of the electromagnetic radiation spectrum that extends from about 9 kHz to about

300 GHz and includes different frequency bands, and, as shown in Figure 1.2, the portion of the RF Spectrum that starts at 100 MHz is referred to as the microwave spectrum. The resonator developed in this project has a fundamental resonant frequency ≈ 350 MHz, hence its designation as a 'microwave' cavity resonator.

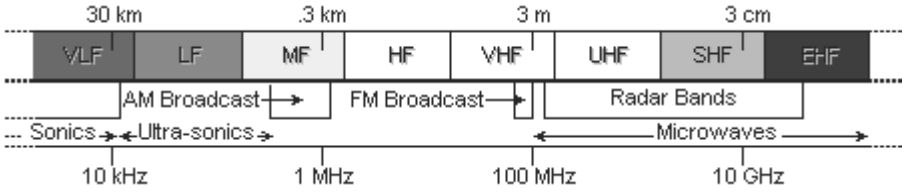

Figure 1.2: RF electromagnetic spectrum

1.4.3 Concept of resonators:

A resonator is a structure that can store energy such that it is continuously converted with a specific rate between two kinds of energy. When the resonator oscillates, energy is converted from one kind to another and back. If more energy is fed to the resonator at the same frequency and in phase with the oscillations, energy will be absorbed and stored in the oscillator. If energy is continuously fed into a resonator, the amount of energy stored will grow until energy is dissipated with the same rate as new energy is stored. If the excitation of a resonator stops, the amplitude of oscillation will decrease exponentially at a rate determined by the quality factor $1/Q$.

In a microwave resonator, used in this work and shown schematically in Figure 1.3, electromagnetic waves travel back and forth between reflecting

points resulting in a standing wave pattern, where the energy pulsates between electric and magnetic energy.

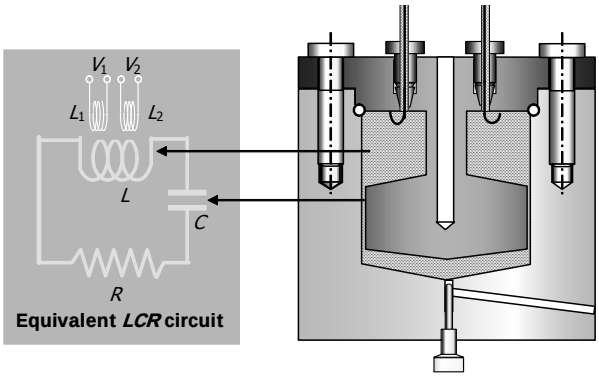

Figure 1.3: Sketch for the microwave cavity resonator developed in this work, showing the coupling loops at the top, drainage valve at the bottom, and analogous *LC* circuit to the left.

The field in the resonator is excited by the external circuit by means of a coupling structure, which radiates the wave into the resonator, and can be, for example, an aperture (small hole), a coupling probe, or a coupling loop, as in this work. The resonant frequency is mainly determined from the size and shape of the structure and the dielectric properties of the medium where the microwaves propagate. Thus, the dielectric properties (relative permittivity) of a medium within a resonator can be determined from the measurements of the resonant frequency. In Chapter 7, Theory and Working Equations, a discussion is included on how the relative permittivity can be determined from the measurement of resonant frequency, and how the density can be determined from the relative permittivity.

1.4.4 VLE prediction and EOS:

Among many equations proposed for predicting phase behaviour such as cubic, virial, and empirical equations of state, the cubic equations of state (CEOS) have been widely used because of their simplicity, accuracy, applicability over a wide range of pressures and temperatures, and most importantly its capability of describing substances in both liquid and vapour phases. Among cubic equations of state, Peng-Robinson (PR) [105] and Soave-Redlich-Kwong (SRK) [106] are the most widely used in the refinery and gas processing industries for the prediction of vapour-liquid equilibria (*VLE*) for systems containing non-polar components. The SRK EOS has been very successful in extending the applicability of CEOS to systems that contain non-polar and slightly polar components, as used in this work. In this work, the PR and SRK EOS have been used as reference correlations to compare with the experimental results. A comprehensive review on the SRK EOS can be found in ref [107], and extensive details of other EOS are found in ref [108], while only a summary of PR and SRK formulations is given in this section.

A generalised CEOS can be described by:

$$p = \frac{RT}{v-b} - \frac{a(T)}{v^2 + ubv + wb^2} \tag{1.12}$$

where R is the gas constant, v is the molar volume, and the parameters u, w, b and $\alpha(T)$ are listed in Table 1.3 [108].

Table 1.3: Parameters for PR and SRK EOS

PR	SRK
$u = 2$	$u = 1$
$w = -1$	$w = 0$
$b = \frac{0.07780\ RT_c}{p_c}$	$b = \frac{0.08664\ RT_c}{p_c}$
$a(T) = \frac{0.45724\ R^2T_c^2}{p_c}\left[1 + f_\omega\left(1 - \sqrt{T_r}\right)\right]^2$ $f_\omega = 0.37464 + 1.54226\ \omega - 0.26992\ \omega^2$	$a(T) = \frac{0.42748\ R^2T_c^2}{p_c}\left[1 + f_\omega\left(1 - \sqrt{T_r}\right)\right]^2$ $f_\omega = 0.48 + 1.574\,\omega - 0.176\,\omega^2$

where ω is the Pitzer acentric factor [109], a substance-specific constant that reflects the geometry and polarity of a molecule and is defined as:

$$\omega = -1 - \log(p_r^{sat})_{T_r=0.7} \tag{1.13}$$

where $p_r^{sat} = \frac{p^{sat}}{p_c}$ is the vapour pressure reduced by p_c, the critical pressure, and $T_r = \frac{T}{T_c}$ is the reduced temperature where T_c is the critical temperature.

While this work investigates the performance of the microwave resonator, it also examines the applicability of these two equations of state to systems that contain non-polar and slightly polar components and may provide insight to one of the most frequently asked questions by engineers: “which

equation of state, PR or SRK, should be selected for *VLE* prediction for petroleum fluids?"

Part I

The Vibrating Wire Viscometer

Nomenclature:

A	Area
B	Magnetic field strength
c	Speed of sound
c_p	Specific heat
D	Diameter; Drag force
E	Young's modulus of elasticity
F	Force
f	Frequency
G	Shear modulus of elasticity
g	Gravitational acceleration; Half width of resonance curve
I	Current
I_a	Area moment of inertia
J	Mass moment of inertia
K_0, K_1	Modified Bessel functions
L	Length
m	Mass
M	Bending moment
Ma	Mach number
p	Pressure
Q	Quality factor of resonance curve
r	Radius
R	Radius; Resistance
Re	Reynolds number
T	Temperature; Tension

t	Time
u	Deflection of the wire in the lateral direction (y)
V	Volume; Shear force; Voltage
v	Velocity
x, y, z	Rectangular co-ordinates
r, θ, z	Cylinderical co-ordinates

Greek Symbols:

β	Dimensionless added mass due to fluid displaced by the wire
β'	Dimensionless damping due to fluid viscosity
γ	Shear angle (loss of φ due to shear effect)
Δ_0	Self damping of the wire (measured in vacuum)
ε	Dimensionless displacement
η	Viscosity
κ_s, κ_T	Isentropic and Isothermal compressibility of the fluid
λ	Coefficient of heat transfer
Λ	Amplitude in eq 3.55
ν	Kinematic viscosity
ρ	Density
σ	Dimensionless radial coordinate
σ^*	Dimensionless radius of container
τ	Shear stress
$\tilde{\tau}$	Dimensionless time
φ	Angle of rotation around x-direction
Φ	Dimensionless stream function
χ	Shape factor of wire cross section
ψ	Stream function
ω	Angular frequency
Ω	Dimensionless quantity closely related to Reynold's number

Definition of subscripts

0	In vacuum
B	Magnetic field
c	Container; Critical
calc	Calculated
exp	Experimental
f	Fluid
r	Resonance
s	Solid wire
x, y, z	In direction of rectangular co-ordinates
r, θ, z	In direction of cylindrical co-ordinates

Boldface denotes a vector quantity.

Chapter 2

LITERATURE REVIEW

The motion of an oscillating wire in a dense fluid was first described in 1828 by Bessel [11] when he noted the need for an added mass correction to the motion of pendulum in air. This added mass effect had been discovered independently by Du Buat [12] in 1786, but it was not until after the appearance of Bessel's memoir that Du Buat's work attracted attention. In 1850, Stokes [13] derived the dependence of the added mass on the viscosity of the surrounding fluid. The practical and theoretical development of the use of the vibrating wire in viscosity measurements is summarized in Table 2.1. The first to use the vibrating wire to measure the viscosity of fluid, to the author's knowledge, are Tough et al. [58] in early 1960. Since then, vibrating wire viscometers were developed widely with different wire materials, diameters, lengths, clamping devices, and with forced or transient modes of oscillation.

As shown in Table 2.1, the vibrating wires have been fabricated from tungsten, stainless steel, chromel, and NbZr alloy. Tungsten is the preferred material because both its Young's modulus and density are high relative to those of other materials, providing a stable resonance and sensitivity with respect to the fluid surrounding it. Further details on the design are discussed in Chapter 4.

Table 2.1 also shows that different wire diameters D of a range from (0.007 to 0.3) mm have been used depending on the measured viscosity range. Smaller diameters are normally used for gases and low viscosity liquids and larger diameters are used for more viscous fluids. Different wire lengths have also been used, in order to satisfy the ratio between the length L and the radius R as $L/R >> 1$. The working equations are discussed in details in Chapter 3.

Different methods for clamping the vibrating wire have been included in Table 2.1. Wires with a single clamp at one end and a buoyant mass at the other end (BM) have been used where the density and viscosity are simultaneously measured as the tension on the wire changes with buoyancy changes. Wires with two clamps at both ends (2C) have been used where only viscosity is measured. Another clamp type with constant tensioning system (CTS) has been used to minimise the changes in the wire tension resulting from the changes in the temperature in the wires using the two clamps (2C) design.

Two modes of oscillations, shown in Table 2.1, have been used in driving the vibrating wire: the forced mode (FR) and the transient mode (TR). The forced mode operates in the frequency domain where a constant ac current drives the wire over a frequency range covering its first harmonic and viscosity is calculated from the width of the resonance signal. The transient mode takes place in the time domain where the wire is driven for a short

time at a frequency near to its resonance then the driving current is switched off and the viscosity is calculated from the decay time. The forced mode requires a simple electronic setup; however, care should be taken to keep the frequency sweep time as short as possible to avoid any rise in the wire temperature.

To the author's knowledge, all but three of the instruments included in Table 2.1 have been used to measure viscosity in the range from (0.008 to 6) mPa·s. The three exceptions are as follows: Charles et al. [48] reported measurements of the viscosity of glycol at about 53 mPa·s; Gourgouillon et al. [34] measured supercritical fluid-saturated polymer (PEG 400) with a viscosity of about 20 mPa·s; and Caetano et al. [27] in 2004 reported measurements of diisodecylphthalate with a viscosity up to 120 mPa·s. In this research, a vibrating wire viscometer has been developed to measure viscosities for standard reference fluids at viscosity up to about 200 mPa·s. The wire is clamped at both ends, with an electrically insulating mechanism. The novel features of this rugged instrument are: the internal volume is small, only 10 cm^3, obtained by reducing the separation between the magnets; the magnets are located within the fluid and, therefore, the dimensions of the magnets required for providing a particular flux at the wire is small. This ultimately reduces the diameter of the complete instrument. This vibrating wire viscometer is considered one of the smallest of its kind as described with more details in Chapter 4.

This viscometer has been used to measure the viscosity of methylbenzene and two reference fluids with nominal viscosities of (14 and 232) mPa·s at T = 298 K and p = 0.1 MPa at temperatures in the range from (298 to 373) K at pressure below 40 MPa. The measured viscosities range from (0.3 to 100) mPa·s. The results obtained differ from literature values by less than 1 %, and measurements show that, as anticipated from the working equations, increasing the wire diameter to 0.150 mm allows the measurements to be performed with fluids of viscosities up to 200 mPa·s with values within 2 % of the reference values. This difference is within the uncertainty of the measurement, which, at that viscosity, was estimated as 3 %. Results are discussed in more details in Chapter 5.

Table 2.1: Review of the literature reporting the development of a vibrating wire to determine fluid viscosity η along with maximum pressures p, temperature range T, estimated uncertainty u, wire material S, wire diameter D, wire length L, clamped at one end with a buoyant mass (BM), clamped at both ends (2C), clamped with a constant tension system (CTS), and operated in either forced (FR) or transient (TR) mode.

ref	$T_{min} - T_{max}$ / K	p / MPa	fluid	η_{min} to η_{max} / mPa·s	$\pm 100u$	S	D / μm	L / mm	clamp	mode	comments
14											theory
15											theory
16	240 to 455	165	natural gas mixtures	0.009 to 0.02	1	W	7			TR	
17	210 to 370	0.1	methylbenzene	0.3 to 2.7	0.5	W			BM	TR	
18	210 to 370	30	methylbenzene	0.3 to 2.7	0.5	W	100	56	BM	TR	
19	303 to 348	250	heptane	0.2 to 2	3	W	100	56	BM	TR	
20	303 to 348	300	heptane	0.2 to 2 3	3	W	100	56	BM	TR	
21	298	70	hexane	0.3 to 0.53	0.5	W	100	54	CTS	TR	
22	303 to 323	80	Benzene, methylbenzene, *m*-xylene	0.42 to 0.89	0.5	W	100	54	CTS	TR	
23	213 to 373	250	methylbenzene		2.5						ref. correlation
24 25			1,1,1,2-tetrafluoroethane (R134a)								IUPAC Round Robin Project
26	303 and 323	70	Methylbenzene, heptane	0.42 to 0.89	0.5	W	100	54	CTS	TR	
27	288 to 308	0.1	diisodecylphthalate	120	1	W	200	60	2C	TR	

Table 2.1 continued

ref	$T_{min} - T_{max}$ / K	p / MPa	fluid	η_{min} to η_{max} / mPa·s	$\pm 100u$	S	D / μm	L / mm	clamp	mode	comments
28	213 to 298	20	methylbenzene	0.55 to 3.3	1.5	W	100	40	CTS	TR	
29	298 to 473	200	dodecane, octadecane	0.22 to 6.7	2	W	100	32	BM	FR	
30	298 to 393	75	mixture of methane and decane	0.08 to 1.65	3	W	100	28	BM	FR	
31	303 to 423	50	mixture of hexane and 1-hexanol	0.2 to 6.7	4	W	100	28	BM	FR	
32	298 to 383	100	pentane	0.1 to 0.43	2.5	W	100	28	BM	FR	
33	222 to 348	80	methylbenzene	0.3 to 2.2	3	W	100	40	BM	FR	
34	313 to 348	25	supercritical CO_2-saturated PEG	20	4	W	100	40	BM	FR	
35	198 to 348	100	2,2,4-trimethylpentane (isooctane)	0.29 to 6	3	W	100	40	BM	FR	
36	199 to 298	100	1,1,1,2-tetrafluoroethane (R134a)	0.2 to 0.8	2.5	W	100	40	BM	FR	
37	197 to 348	40	cyclohexane, 1,1,1,2-tetrafluoroethane, 2,2,4-trimethylpentane	0.2 to 3	2	W	100	40	BM	FR	
38	260 to 300	100	CO_2(l)	0.06 to 0.24	0.5	W	100	56	BM	FR	
39											theory
40	298 and 323	10	methylbenzene	0.422 to 0.6	0.4 FR 0.8 TR	W	100	40	BM	FR & TR	
41	231 to 343	5.1	R32, R125	0.06 to 0.25	1	W	7.5	140	BM	TR	
42	223 to 343	4.8	R134a, R32, R125	0.01 to 0.015	2	W	7.5	140	BM	TR	
43	303 to 348	250	methylbenzene, pentane, hexane, octane, and decane	0.18 to 5.9	0.5	W	100	56	BM	TR	
44	235 to 343	50	R134a	0.11 to 0.24	0.6	W	100	56	BM	TR	

Table 2.1 continued

ref	$T_{min} - T_{max}$ / K	p / MPa	fluid	η_{min} to η_{max} / mPa·s	±100u	S	D / μm	L / mm	clamp	mode	comments
45	298 to 423	20	C_3H_4 (g)	0.008 to 0.07	3		25	90	BM	TR	chromel wire
46	298 to 423	20	Ar, Kr, C_3H_8	0.022 to 0.04	3		25	90	BM	TR	chromel wire
47	298 to 500	40			0.2						theory
48	80 to 323		H_2O, glycol, CS_2, O_2(l), Ar(g)	0.024 to 53	0.13	W	100	50	2C	TR	
49	223 to 323	779	Ar	0.11 to 0.33		W	50	20	2C	TR	
50	273	1000	CH_4	0.01 to 0.415		W	50	20	2C	TR	
51	220 to 280	450	CO_2(l)	0.5	0.5	W	50	20	2C	TR	
52	174.45	470	Ar	0.61	2.5	W	50	15	2C	TR	
53	243 to 393	3.5	1,1-difluoroethane (R152a)	0.012 to 0.34	2.8	W	50	15	2C	TR	
54											theory
55											theory
56	174	471	Ar								
57	2.18 to 1.1		^{3}He (l)	0.026	5	W	25	50	2C	TR	
58											theory
59	1.8 to 3.2	2.5	^{4}He	0.023 to 0.07		SS	80	50	2C	TR	
60											theory
61											theory
62	0.0013		^{3}He				300				NbZr wire

Chapter 3

THEORY AND WORKING EQUATIONS

The complete theory of a viscometer based on measurements of the resonance frequency of a circular section rod performing steady transverse oscillations in the fluid has been presented by Retsina et al. [14, 15]. This theory was established as a result of a detailed analysis of the fluid flow around the rod, as well as the mechanical motion of the rod. The theory is valid over a range of conditions that includes those used for the vibrating wire viscometer developed in this research. This chapter contains, in addition to the working equations, an overview of the theory with emphasis on the constraints and limitations over which the working equations are valid.

The equations in this chapter are grouped into three main categories: (1) the mechanical motion of the wire; (2) the motion of the fluid surrounding the wire; and (3) the equations relating the viscosity of the fluid to the measurement of the induced electromotive force (emf) arising from the motion of the wire with an applied current within a magnetic field.

3.1 The mechanical motion of a wire:

The mathematical model of the motion of the wire is based on the elastic beam theory with the following assumptions for the beam:

(1) is essentially an elastic solid in which one dimension is predominant over the others, i.e. its length is much longer than its thickness,

(2) is prismatic, i.e. the cross sections are the same,

(3) is homogeneous, i.e. with constant material characteristics,

(4) is straight, i.e. its axis is a part of a straight line,

(5) and is untwisted, that is the principle axes of elasticity of all sections are equally directed in space.

The simplest and best-known models for straight, prismatic beams are: the Euler-Bernoulli theory, also called classical beam theory [63], which is based on the added assumptions that both shear deformation and rotational inertia of the cross sections are negligible if compared with bending deformation and translational inertia; and the Timoshenko beam theory [64] which incorporates a correction for transverse shear effects and rotational inertia of the cross sections, usually referred to as the 'Timoshenko Beam'.

3.1.1 Simple lateral vibration of the wire:

As illustrated in Figure 3.1 (a), the lateral vibration of the wire in the *yz* plane when the deflection $u(z, t)$ is assumed due to the bending moment only, as the

Euler-Bernoulli beam, the displacement u in the y direction and the rotation φ around the x direction are linked with the relation:

$$\varphi_x = \frac{\partial u}{\partial z}, \tag{3.1}$$

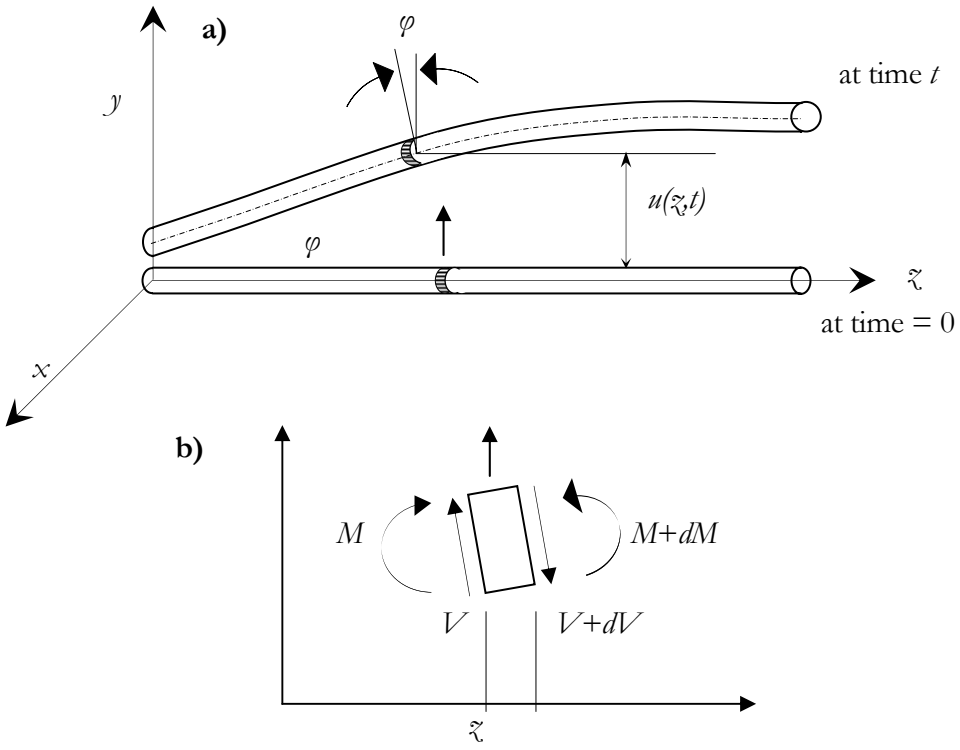

Figure 3.1: Flexural behaviour of a straight beam in the yz plane.

and the dynamic force equation on the element shown in Figure 3.1 (b) is:

$$m_s \frac{\partial^2 u}{\partial t^2} \partial z = -\left(V + \frac{\partial V}{\partial z} \partial z \right) + V \,, \tag{3.2}$$

i.e the inertia force equation is.

$$m_s \frac{\partial^2 u}{\partial t^2} = -\frac{\partial V}{\partial z}. \tag{3.3}$$

where m_s is the mass per unit length and V is the shear force, and by summing the moments M about any point on the right surface of the element (at $z + dz$) gives:

$$\frac{\partial M}{\partial z} dz - V dz = 0, \tag{3.4}$$

i.e.

$$\frac{\partial M}{\partial z} = V, \tag{3.5}$$

Substituting for V in eq 3.3, gives:

$$m_s \frac{\partial^2 u}{\partial t^2} = -\frac{\partial^2}{\partial z^2}(M), \tag{3.6}$$

from elementary strength of materials, the wire curvature and the moment M are related by:

$$EI_a \frac{\partial^2 u}{\partial z^2} = M, \tag{3.7}$$

where E represents the extensional Young's modulus of elasticity for the rod material, I_a is the second moment of inertia, then substituting in eq 3.6

$$m_s \frac{\partial^2 u}{\partial t^2} = -\frac{\partial^2}{\partial z^2}\left(EI_a \frac{\partial^2 u}{\partial z^2} \right), \tag{3.8}$$

if the product EI_a which represents the flexural stiffness of the wire is constant, then the equation reduces to :

$$m_s \frac{\partial^2 u}{\partial t^2} + EI_a \frac{\partial^4 u}{\partial z^4} = 0 . \tag{3.9}$$

The above equations are based on the assumption of negligible shear deformation and rotary inertia and do not include the effect of axial tension force which is calculated in the following section.

3.1.2 Effect of axial force loading:

The vibrating wire under the effect of an axial tension force T oscillates in a fashion very similar to a taut string. In Figure 3.2 (a) the lateral, sometimes called transverse, deflection u is a function of position z and time t, and by applying Newton's second law on the element shown in Figure 3.2 (b), assuming small deflection u and φ, the equation of motion is:

$$m_s dz \frac{\partial^2 u}{\partial t^2} = T\left(\varphi + \frac{\partial \varphi}{\partial z} dz \right) - T\varphi , \tag{3.10}$$

since the flexural stiffness in the wire cannot be ignored, as in the case of the string model, additional inertia forces from eq 3.3 to eq 3.10 to give:

$$m_s dz \frac{\partial^2 u}{\partial t^2} = T\left(\varphi + \frac{\partial \varphi}{\partial z} dz\right) - T\varphi - \left(V + \frac{\partial V}{\partial z} dz\right) + V\,, \tag{3.11}$$

or

$$m_s \frac{\partial^2 u}{\partial t^2} = T \frac{\partial^2 u}{\partial z^2} - \frac{\partial V}{\partial z}\,, \tag{3.12}$$

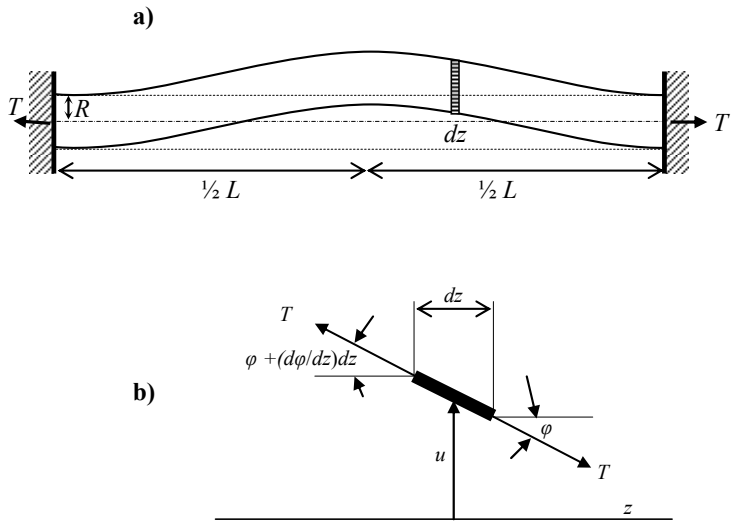

Figure 3.2: Lateral vibration of the wire with axial tension T

substituting eqs 3.5 and 3.7 in eq 3.12, we obtain:

$$m_s \frac{\partial^2 u}{\partial t^2} = T \frac{\partial^2 u}{\partial z^2} - \frac{\partial^2}{\partial z^2}\left(EI_a \frac{\partial^2 u}{\partial z^2}\right), \tag{3.13}$$

Since the bending stiffness of the wire EI_a is constant, then

$$EI_a \frac{\partial^4 u}{\partial z^2} - T \frac{\partial^2 u}{\partial z^2} + m_s \frac{\partial^2 u}{\partial t^2} = 0 . \tag{3.14}$$

which is the vibrating wire equation under the effect of the axial tension loading with the assumption of ignoring the effect of rotary inertia and shear deformation which is discussed in the following section .

3.1.3 Effect of rotary inertia and shear deformation

By including the effect of the shear deformation, as in Timoshenko beam, the slope of the centre line of the wire will diminish by the shear angle γ, hence eq 3.1 yields:

$$\frac{\partial u}{\partial z} = \varphi - \gamma , \tag{3.15}$$

with φ is the slope due to the bending and γ is the loss of that slope due to the shear effect calculated as:

$$\gamma = \frac{V}{\chi AG} , \tag{3.16}$$

where A is the cross sectional area, G the modulus of elasticity in shear, and χ is a shape factor of the cross section, for a circular beam a value of 0.9 was reported by Cowper [65] and the wire curvature $\frac{\partial \varphi}{\partial z}$ can be expressed as:

$$\frac{\partial \varphi}{\partial z} = \frac{M}{EI_a}, \tag{3.17}$$

by adding the rotary inertia, a dynamic moment equation is introduced in addition to the dynamic force eq 3.12 as:

$$m_s \frac{\partial^2 u}{\partial t^2} = T \frac{\partial^2 u}{\partial z^2} - \frac{\partial V}{\partial z}, \quad \text{and} \quad J \frac{\partial^2 \varphi}{\partial t^2} = \frac{\partial M}{\partial z} - V, \tag{3.18}$$

where J is the mass rotary inertia per unit length of the wire in the yz plane, which has an effect equivalent to an increase in the mass, hence decreasing the natural frequency of the wire. This effect has more influence at the higher frequencies and on the higher modes of oscillations.

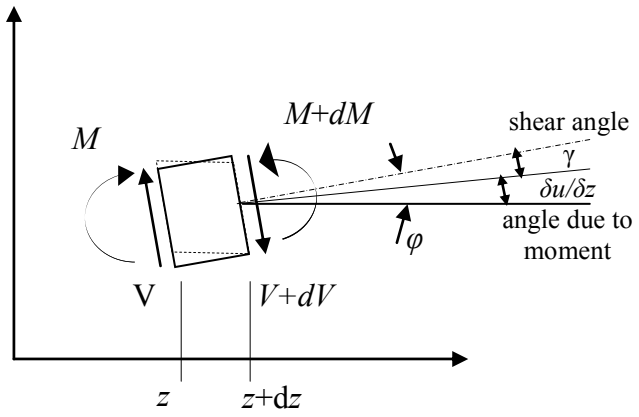

Figure 3.3: lateral vibration of the wire with rotary inertia and shear deformation.

Combining eq 3.15 to 3.18 gives the equilibrium equation for the translation motion in the y direction, and the rotation around the x axis:

$$EI_a \frac{\partial^4 u}{\partial z^4} - T\frac{\partial^2 u}{\partial z^2} + m_s \frac{\partial^2 u}{\partial t^2} - (J + \frac{EI_a m_s}{\chi AG})\frac{\partial^4 u}{\partial z^2 \partial t^2} + \frac{Jm_s}{\chi AG}\frac{\partial^4 u}{\partial t^4} = 0 . \qquad (3.19)$$

Substituting for $m_s = \rho_s A$, and $J = \rho_s I$ where ρ_s is the wire density gives:

$$EI_a \frac{\partial^4 u}{\partial z^4} - T\frac{\partial^2 u}{\partial z^2} + m_s \frac{\partial^2 u}{\partial t^2} - \rho_s I_a (1 + \frac{E}{\chi G})\frac{\partial^4 u}{\partial z^2 \partial t^2} + \frac{\rho_s^2 I}{\chi G}\frac{\partial^4 u}{\partial t^4} = 0 . \qquad (3.20)$$

The last two terms in the above equation are due to the effect of the shear deformation and the rotary inertia and if the wire undergoes a periodic transverse oscillation under the influence of an applied force per unit length, $F(z,t)\mathrm{e}^{\mathrm{i}\omega t}$, where ω is the angular frequency of oscillation, then eq 3.20 becomes:

$$EI_a \frac{\partial^4 u}{\partial z^4} - T\frac{\partial^2 u}{\partial z^2} + m_s \frac{\partial^2 u}{\partial t^2} - \rho_s I_a (1 + \frac{E}{\chi G})\frac{\partial^4 u}{\partial z^2 \partial t^2} + \frac{\rho_s^2 I}{\chi G}\frac{\partial^4 u}{\partial t^4} = F(z,t)\mathrm{e}^{\mathrm{i}\omega t} . \qquad (3.21)$$

3.1.4 The effect of the surrounding fluid:

The presence of the fluid around the wire modifies its natural frequency of oscillation observed in vacuum, as well as the width of resonance peak during its course of forced oscillation. The modification of the resonance frequency is attributed to the fluid density, which presents as the added mass m_f in the equation of motion of the wire. While the modification of the width of the resonance peak is attributed to the fluid viscosity as an added additional drag

force D_f to the internal damping of the wire material D_0 which is proportional to the velocity of the wire. Hence, the most general form of the differential equation governing the motion of the wire surrounded by the fluid is:

$$EI_a\frac{\partial^4 u}{\partial z^4}-T\frac{\partial^2 u}{\partial z^2}+(m_s+m_f)\frac{\partial^2 u}{\partial t^2}+(D_f+D_0)\frac{\partial u}{\partial t}-\rho_s I_a(1+\frac{E}{\chi G})\frac{\partial^4 u}{\partial z^2\partial t^2}+\frac{\rho_s^2 I}{\chi G}\frac{\partial^4 u}{\partial t^4}=F(z,t)\mathrm{e}^{\mathrm{i}\omega t} \tag{3.22}$$

Providing that the displacement of the wire u is very small compared to its radius R, and the length of the wire L is much larger than its radius, then the distortion arising from the shear deformation has negligible effect on the wire motion, and eq 3.22 reduces to:

$$EI_a\frac{\partial^4 y}{\partial z^4}-T\frac{\partial^2 y}{\partial z^2}+(m_f+m_s)\frac{\partial^2 y}{\partial t^2}+(D_f+D_0)\frac{\partial y}{\partial t}=F(z,t)\mathrm{e}^{\mathrm{i}\omega t}, \tag{3.23}$$

with the second moment of area given by:

$$I_a=\frac{1}{2}\pi R^4,$$

the wire mass per unit length by:

$$m_s=\rho_s\pi R^2,$$

the added mass due to the surrounding fluid by:

$$m_f = \rho \pi R^2 k ,$$

the coefficient of internal damping of the wire material by:

$$D_0 = 2\rho_s \pi R^2 \omega \Delta_0 ,$$

and the added damping due to surrounding fluid by:

$$D_f = \rho \pi R^2 \omega k' .$$

The parameter Δ_0 is the damping coefficient of the wire determined from measurements in vacuum, and the parameters *k*, and *k'* are determined from the fluid mechanics as functions of the frequency of oscillation, as discussed in the following section.

3.2 Analysis of the fluid mechanics:

Since the problem of the fluid mechanics around the vibrating wire has been reported in detail with a complete derivation in [14, 15], only the main equations are included in this section with a focus on the constraints and the assumptions used in the derivation.

As shown in Figure 3.4, the motion of the fluid is contained in a container with a circular cross section, of radius R_c, coincident with the initial position of the wire at rest. From the previous assumption that the wire is infinitely long ($L >>$

R), and since the wire ends are clamped, hence no motion, the effect of the end clamps on the fluid is negligible, and consequently, the only significant motion of the fluid occurs in the *r*-θ plane.

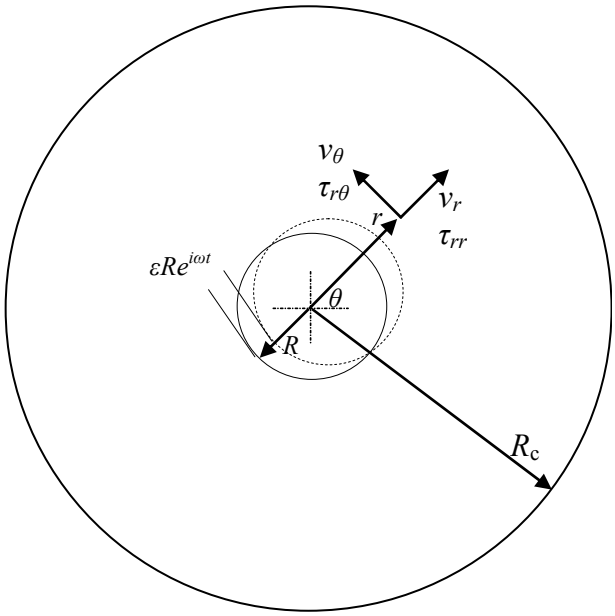

Figure 3.4: Vibrating wire with radius *R* contained within a cylindrical container surface of radius R_c coincident with the wire position at rest.

The effect of the fluid compressibility is also ignored in this analysis; therefore another limitation is that the fluid is assumed to be an incompressible Newtonian fluid, thus introducing the following constraint on the Mach number:

$$Ma = \frac{\omega \varepsilon R}{c} << 1\,, \tag{3.24}$$

where c is the speed of sound in the fluid, and $\varepsilon = u/R$ is a dimensionless amplitude of oscillation where u and R are the wire displacement and radius respectively.

In that case, after combining the gravitational effects into the pressure p, the mass conservation equation becomes:

$$\frac{1}{r}\frac{\partial}{\partial r}(rv_r)+\frac{1}{r}\frac{\partial v_\theta}{\partial \theta}=0, \tag{3.25}$$

and the radial momentum (r-momentum) conservation equation is:

$$\begin{aligned}&\rho\left[\frac{\partial v_r}{\partial t}+v_r\frac{\partial v_r}{\partial r}+\frac{v_\theta}{r}\frac{\partial v_r}{\partial \theta}-\frac{v_\theta^2}{r}\right]=\\&\frac{-\partial p}{\partial r}+\eta\left[\frac{\partial}{\partial r}\left(\frac{1}{r}\frac{\partial}{\partial r}\left(rv_r\right)\right)+\frac{1}{r^2}\frac{\partial^2 v_r}{\partial \theta^2}-\frac{2}{r^2}\frac{\partial v_r}{\partial \theta}\right],\end{aligned} \tag{3.26}$$

and the angular momentum (θ-momentum) conservation equation is:

$$\begin{aligned}&\rho\left[\frac{\partial v_r}{\partial t}+v_r\frac{\partial v_\theta}{\partial r}+\frac{v_\theta}{r}\frac{\partial v_\theta}{\partial \theta}-\frac{v_r v_\theta}{r}\right]=\\&\frac{-1}{r}\frac{\partial p}{\partial \theta}+\eta\left[\frac{\partial}{\partial r}\left(\frac{1}{r}\frac{\partial}{\partial r}\left(rv_\theta\right)\right)+\frac{1}{r^2}\frac{\partial^2 v_\theta}{\partial \theta^2}-\frac{2}{r^2}\frac{\partial v_r}{\partial \theta}\right],\end{aligned} \tag{3.27}$$

where v_r and v_θ are the components of the fluid velocity in the radial and angular directions respectively and equals:

$$v_r = \mathrm{i}\omega\varepsilon R\mathrm{e}^{\mathrm{i}\omega t}\cos\theta\,, \tag{3.28}$$

and

$$v_\theta = -\mathrm{i}\omega\varepsilon R\,\mathrm{e}^{\mathrm{i}\omega t}\sin\theta\,, \tag{3.29}$$

at

$$r = \varepsilon R\,\mathrm{e}^{\mathrm{i}\omega t}\cos\theta + R\sqrt{1-\varepsilon^2\mathrm{e}^{2\mathrm{i}\omega t}\sin^2\theta}\,, \tag{3.30}$$

which represents the position of the vibrating wire, as shown in Figure 3.4, and

$$v_r = v_\theta = 0 \quad \text{at} \quad r = R_c\,, \tag{3.31}$$

representing v_r and v_θ in terms of the stream function Ψ:

$$v_r = \frac{1}{r}\frac{\partial\Psi}{\partial\theta} \quad , \quad v_\theta = \frac{-1}{r}\frac{\partial\Psi}{\partial r}\,. \tag{3.32}$$

Combining eqs 3.26 and 3.27 can give a single equation for Ψ by cross differentiation and elimination of p. Introducing the dimensionless parameters:

for stream function : $\Phi = \dfrac{\Psi}{\varepsilon\omega R^2}$,

for frequency based on ρ : $\Omega = \dfrac{\rho\omega \mathrm{R}^2}{\eta}$,

for radial coordinate : $\sigma = \dfrac{r}{R}$, (3.33)

for radius of the container : $\sigma^* = \dfrac{R_c}{R}$,

and time : $\tilde{\tau} = \dfrac{t\eta}{\rho R^2}$.

a single equation is obtained as:

$$\begin{aligned}&\frac{1}{\sigma}\frac{\partial^3\Phi}{\partial\theta^2\partial\tilde{\tau}}+\frac{\partial^2\Phi}{\partial\sigma\partial\tilde{\tau}}+\sigma\frac{\partial^3\Phi}{\partial\sigma^2\partial\tilde{\tau}}+\varepsilon\Omega[\frac{1}{\sigma^2}\frac{\partial\Phi}{\partial\theta}\frac{\partial^3\Phi}{\partial\sigma\partial\theta^2}-\frac{2}{\sigma^3}\frac{\partial^2\Phi}{\partial\theta^2}\frac{\partial\Phi}{\partial\theta}\\&-\frac{1}{\sigma^2}\frac{\partial\Phi}{\partial\sigma}\frac{\partial^3\Phi}{\partial\theta^3}-\frac{1}{\sigma}\frac{\partial^2\Phi}{\partial\sigma\partial\theta}\frac{\partial\Phi}{\partial\sigma}+\frac{\partial\Phi}{\partial\theta}\frac{\partial^3\Phi}{\partial\sigma^3}-\frac{\partial\Phi}{\partial\sigma}\frac{\partial^3\Phi}{\partial\sigma^2\partial\theta}+\frac{1}{\sigma}\frac{\partial\Phi}{\partial\theta}\frac{\partial^2\Phi}{\partial\sigma^2}\\&-\frac{1}{\sigma^2}\frac{\partial\Phi}{\partial\theta}\frac{\partial\Phi}{\partial\sigma}]=\frac{2}{\sigma}\frac{\partial^4\Phi}{\partial\theta^2\partial\sigma^2}-\frac{2}{\sigma^2}\frac{\partial^3\Phi}{\partial\sigma\partial\theta^2}+\frac{1}{\sigma^3}\frac{\partial^4\Phi}{\partial^4\theta}+2\frac{\partial^3\Phi}{\partial\sigma^3}+\sigma\frac{\partial^4\Phi}{\partial\sigma^4}\\&-\frac{1}{\sigma}\frac{\partial^2\Phi}{\partial\sigma^2}+\frac{1}{\sigma^2}\frac{\partial\Phi}{\partial\sigma}+\frac{4}{\sigma^3}\frac{\partial^2\Phi}{\partial\theta^2}\end{aligned} \tag{3.34}$$

Since the Reynold's number, defined as the ratio of inertial to viscous forces, $Re = \rho\omega\varepsilon \mathrm{R}^2/\eta$, the dimensionless quantity Ω in eq 3.33 can equal $\Omega = Re/\varepsilon$, or $Re = \varepsilon\Omega$, and because this Reynolds number, which is based on the wire displacement, is small, since $\varepsilon << 1$, then the inertial terms in eq 3.34 which are nonlinear in Φ (inside the square brackets) may be neglected. However, Ω should not be so small in order to retain the viscous and the linear inertial effects, therefore, the solution is only valid by the restriction that:

$$\Omega \approx 1 \text{ and } \mathrm{Re} \approx \varepsilon << 1, \tag{3.35}$$

so that eq 3.34 reduces to:

$$\begin{aligned} &\frac{1}{\sigma}\frac{\partial^3\Phi}{\partial\theta^2\partial\tilde{\tau}} + \frac{\partial^2\Phi}{\partial\sigma\partial\tilde{\tau}} + \sigma\frac{\partial^3\Phi}{\partial\sigma^2\partial\tilde{\tau}} = \frac{2}{\sigma}\frac{\partial^4\Phi}{\partial\theta^2\partial\sigma^2} - \frac{2}{\sigma^2}\frac{\partial^3\Phi}{\partial\sigma\partial\theta^2} + \frac{1}{\sigma^3}\frac{\partial^4\Phi}{\partial^4\theta} \\ &+2\frac{\partial^3\Phi}{\partial\sigma^3} + \sigma\frac{\partial^4\Phi}{\partial\sigma^4} - \frac{1}{\sigma}\frac{\partial^2\Phi}{\partial\sigma^2} + \frac{1}{\sigma^2}\frac{\partial\Phi}{\partial\sigma} + \frac{4}{\sigma^3}\frac{\partial^2\Phi}{\partial\theta^2} \end{aligned} \tag{3.36}$$

with the boundary conditions:

$$\begin{aligned} &\frac{\partial\Phi}{\partial\theta} = \sigma \mathrm{i} e^{i\Omega\tilde{\tau}}\cos\theta, \quad \frac{\partial\Phi}{\partial\sigma} = \mathrm{i}e^{\mathrm{i}\Omega\tilde{\tau}}\sin\theta \ \text{ at } \ \sigma = 1 \\ &\text{and } \ \Phi = 0 \ \text{ at } \ \sigma = \sigma^* \end{aligned} \tag{3.37}$$

Motivated by the boundary conditions, a solution for eq 3.36 is assumed of the form:

$$\Phi = \mathrm{e}^{\mathrm{i}\Omega\tilde{\tau}} f(\sigma)\sin\theta, \tag{3.38}$$

substituting eq 3.37 into eq 3.36 gives:

$$\left(\frac{d^2}{d\sigma^2} + \frac{1}{\sigma}\frac{d}{d\sigma} - \frac{1}{\sigma^2} - \mathrm{i}\Omega\right)\left(\frac{d^2 f}{d\sigma^2} + \frac{1}{\sigma}\frac{df}{d\sigma} - \frac{1}{\sigma^2}f\right) = 0, \tag{3.39}$$

with boundary conditions:

$$f = \mathrm{i} \ \text{ and } \ \frac{df}{d\sigma} = \mathrm{i} \ \text{ at } \sigma = 1, \ \text{ and } \ f = 0 \ \text{ at } \sigma = \sigma^*, \tag{3.40}$$

and the solution to eq 3.39 becomes:

$$f = \frac{A}{\sigma} - D\mathrm{i}K_1\left(\sigma\sqrt{\mathrm{i}\Omega}\right). \tag{3.41}$$

In eq 3.41, K_1 is the modified Bessel function of the second kind, with the parameters A and D determined from the boundary conditions eq 3.40:

$$A = \mathrm{i}\left[1 + \frac{2K_1\left(\sqrt{\mathrm{i}\Omega}\right)}{\sqrt{\mathrm{i}\Omega}K_0\left(\sqrt{\mathrm{i}\Omega}\right)}\right], \quad D = \frac{-2}{\sqrt{\mathrm{i}\Omega}K_0\left(\sqrt{\mathrm{i}\Omega}\right)}. \tag{3.42}$$

In order to evaluate the added mass and drag force (represented later by the parameters k and k') introduced in the wire mechanical motion, the force per unit length $\tilde{F}$ that the wire exerts on the fluid can be written as:

$$\tilde{F} = -\int_0^{2\pi}\left\{\left(-p + \tau_{rr}\right)\cos\theta - \tau_{r\theta}\sin\theta\right\} r d\theta\Big|_{r=R}, \tag{3.43}$$

where p is given by eq 3.27 and the radial normal and shear stress components τ_{rr} and $\tau_{r\theta}$ are given by:

$$\begin{aligned} \tau_{rr} &= 2\eta\frac{\partial v_r}{\partial r}, \\ \text{and} \quad \tau_{r\theta} &= \eta\left[r\frac{\partial}{\partial r}\left(\frac{v_\theta}{r}\right) + \frac{1}{r}\frac{\partial v_r}{\partial\theta}\right]. \end{aligned} \tag{3.44}$$

The $\tilde{F}$ in eq 3.43 can be written as:

$$\tilde{F} = \eta\omega\varepsilon R\pi\Omega e^{i\omega t}\left(1+2iA\right), \tag{3.45}$$

and also expressed in the form:

$$\tilde{F} = \rho\pi R^2\left(-\omega^2\varepsilon R e^{i\omega t}k + i\omega\varepsilon R e^{i\omega t}k'\right), \tag{3.46}$$

where the term ($-\omega^2\varepsilon R e^{i\omega t}$) represents the acceleration and the term ($i\omega\varepsilon R e^{i\omega t}$) represents the velocity. By eq 3.45 to eq 3.46, the parameters k and k' can be found as:

$$k = -1+2\Im(A),\ k' = 2\Re(A). \tag{3.47}$$

where the symbols $\Re$ and $\Im$ represent the real and imaginary components of A respectively, which can be found from eq 3.42.

The equations used to calculate the viscosity from the measurement of the induced voltage signal are discussed in the next section.

3.3 The working equations:

The wire is clamped under tension between two fixed supports and placed in a magnetic field (assumed uniform), while driven in steady state transverse oscillations by passing through it an alternating current. In that case, the complex voltage $\boldsymbol{V}$ across the wire is given by:

$$\boldsymbol{V} = \boldsymbol{V}_1 + \boldsymbol{V}_2, \tag{3.48}$$

where $\boldsymbol{V}_1$ is the voltage arising from the electrical impedance of the effectively stationary wire and $\boldsymbol{V}_2$ represents the motional emf. $\boldsymbol{V}_1$ is represented empirically by:

$$\boldsymbol{V}_1 = a + \mathrm{i}b + \mathrm{i}cf\,, \tag{3.49}$$

where f is the frequency at which the wire is driven and a, b, and c account for the electrical impedance of the wire and absorb the offset used in the lock-in amplifier to ensure that the voltage signal is detected in the most sensitive range. a, b, and c are adjustable parameters determined by regression.

The complex induced voltage $\boldsymbol{V}_2$ is proportional to the velocity of the wire v and magnetic field strength B from Faraday's Law of induction and can be averaged along the length of the wire as:

$$\boldsymbol{V}_2 \approx \frac{2}{L}\int_0^L Bv\,dz\,. \tag{3.50}$$

In eq 3.50, B is the magnetic flux and v the velocity of the wire which is given in refs [14, 15] as:

$$v = \frac{fF_{\mathrm{B}}\mathrm{i}}{\pi^2\rho_s R^2\left[f_0^2 - (1+\beta)f^2 + \left(\beta' + 2\Delta_0\right)f^2\mathrm{i}\right]}\,, \tag{3.51}$$

where F_B is the magnetic force per unit length $F_B \approx BI$ assumed to be uniform and distributed evenly along the wire length, and I is the amplitude of the current. Substituting eq 3.51 into eq 3.50 gives $\boldsymbol{V}_2$ as:

$$\boldsymbol{V}_2 = \frac{2ILB^2 f\mathrm{i}}{\pi^3 \rho_s R^2 \left[f_0^2 - (1+\beta)f^2 + (\beta' + 2\Delta_0)f^2\mathrm{i}\right]},$$

or (3.52)

$$\boldsymbol{V}_2 = \frac{\Lambda f\mathrm{i}}{f_0^2 - (1+\beta)f^2 + (\beta' + 2\Delta_0)f^2\mathrm{i}},$$

where $\Lambda = 2ILB^2/\pi^3\rho_s R$, corresponds to the amplitude, f_0 the resonance frequency in vacuum, Δ_0 the internal damping of the wire, β the added mass arising from the fluid displaced by the wire, and β' the damping due to the fluid viscosity. The added mass and damping have been calculated in eq 3.23 as (m_f, and D_f) but β and β' are rendered dimensionless here as:

$$\beta = k\frac{\rho}{\rho_s} \quad \text{and} \quad \beta' = k'\frac{\rho}{\rho_s}, \tag{3.53}$$

where k and k' are given as function of Ω in eq 3.47, where Ω is related to the viscosity from the relation:

$$\Omega = \frac{2\pi f \rho R^2}{\eta}, \tag{3.54}$$

and the equation of the total voltage replicating the measured voltage can be given as:

$$\boldsymbol{V} = \frac{\Lambda f \mathrm{i}}{f_0^2 - (1+\beta) f^2 + \left(\beta' + 2\Delta_0\right) f^2 \mathrm{i}} + \mathrm{i}cf + \mathrm{i}b + c\,. \tag{3.55}$$

Chapter 4

APPARATUS AND EXPERIMENTAL PROCEDURE

The general design and the construction of the apparatus, developed in this project, are described in this chapter. The calibration methods for pressure and temperature measurements are also reported here with more details included in the appendix. The data acquisition system and the measurement procedure are described at the end of this chapter.

4.1 Design limitations:

The design of this instrument is based on the limitations discussed in the previous chapter. These limitations and assumptions are: (1), the radius of the wire R must be small in comparison with the length L of the wire, in our case this ratio (R/L) = 0.0006 for the 0.05 mm diameter wire and 0.0018 for the 0.15 mm diameter wire; (2), the compressibility of the fluid is negligible with $Ma \ll 1$, in our case $Ma \approx 7 \cdot 10^{-5}$ based on measurements of sound speed in methylbenzene reported in ref [66], however, this can not be considered a practical constraint as this method can also be applied to gases where $Ma \approx 50 \cdot 10^{-7}$; (3), the inner radius of the body containing the fluid R_c is large in comparison to that of the wire R (in our case R_c/R = 150 for the 0.05 mm diameter wire and 50 for the 0.15 mm diameter wire). A detailed treatment [15,

67, 68] revealed that the uncertainty in the viscosity arising from the location of the boundary relative to the wire is less than 0.5 % for R_c/R = 33; and (4), the relative amplitude of oscillation $\varepsilon << 1$, in our case ε is estimated to be < 0.03. A maximum value of 0.08 was allowed by Mostert et al. [55]. All of these conditions must be satisfied in the design and in the remainder of this chapter it will be shown that these are satisfied for the viscometer described here.

4.2 The vibrating wire assembly:

4.2.1 The vibrating wire:

As mentioned earlier, two vibrating wires were constructed in this research, with nominal diameters (0.05 and 0.15) mm, and both are of nominal length 40 mm. A cross section schematic is illustrated in Figure 4.1.

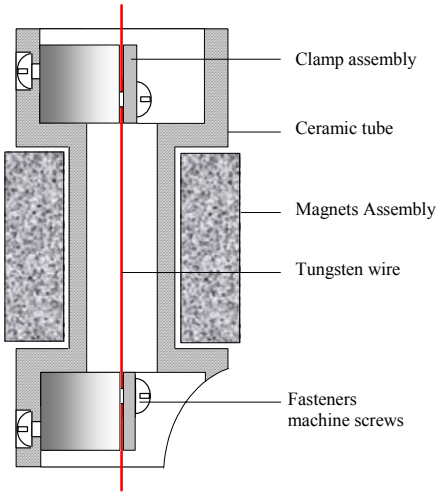

Figure 4.1: Schematic cross section of the vibrating wire viscometer showing the holder tube, magnet blocks, and the nonmagnetic wire clamps.

The wires used were tungsten that, despite its surface roughness, is the preferred material because both Young's modulus $E \approx 411$ GPa and density $\rho_s \approx 19300$ kg·m^{-3} [69] are high relative to other materials. The former provides a stable resonance while the latter provides sensitivity to the fluid around it, through the ratio ρ/ρ_s in eq 3.51. The effect of surface roughness is negligible provided the amplitude of vibration is small and Reynolds number less than 100 as reported by Wilhelm et al. [47]. The wires used in this experiment were obtained from Goodfellow™, Cambridge, UK, with a mass fraction purity > 99.95 %. The wire was cold drawn and, consequently, the cross-section had elliptical rather than circular symmetry, which results in the resonance appearing as a doublet but that effect was reduced by tuning the magnetic field as discussed next.

4.2.2 The end clamps:

The position at which the wire is clamped needed to be geometrically well-defined because rotation can give rise to additional resonance frequencies. Therefore, clamps were used that restrict, as much as possible, motion to one plane that is perpendicular to the magnetic field. Each clamp, shown in Figure 4.2, was fabricated from austenitic stainless steel grade 316 as two pieces, one semi-cylindrical with a diameter of 8 mm and a height of 8 mm, and the other

a flat plate. Both clamping surfaces were polished. To restrict the motion to one plane the wire was clamped within a slot. The magnetic field was then aligned so as to both preferentially excite one of the two components arising from non-circular symmetry and to vibrate the wire in a plan perpendicular to the slot.

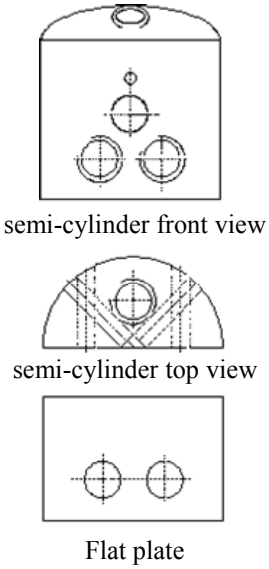

Figure 4.2: Schematic of the two clamp parts fabricated from non-magnetic austenitic stainless steel type 316.

The wire was clamped between the two plates at one end with two stainless steel screws M1.5. The other end of the wire passed through the second open clamp and was attached to a mass for about 24 h after which time the lower clamp was carefully tightened and the mass removed. The selection of tension

mass was based on the desired fundamental resonance frequency f_r neglecting the wire stiffness, that was estimated from:

$$f_r \approx \frac{1}{2L}\sqrt{\frac{mg}{\rho_s \pi R^2}}\,. \qquad (4.1)$$

where m is the mass, g the local acceleration of free fall and L the wire length. The tension mass was selected to both determine the fundamental resonance frequency and maintain the tension between (20 and 50) % of its tensile yield stress, ≈ 720 MPa, in order to preserve the consistency of the physical properties of the wire [19]. The resonance frequency was estimated to be about 1.5 kHz from eq 4.1 for $m \approx 500$ g and tungsten wire diameter of 0.15 mm.

4.2.3 The holding tube:

The two clamps were separated from each other by a tube fabricated from Macor® (a machinable glass ceramic) obtained from Wesgo™ Ceramics, Hayward, US. The electrical resistivity of this material is > 10^{16} Ω·m and the linear thermal expansion coefficient was $13 \cdot 10^{-6}$ K^{-1} which is about 4 times that of tungsten at T = 298 K. Two tubes were fabricated both with an outer diameter of 10 mm, one with an inner diameter of 5 mm that was used with the 0.05 mm diameter wire, and the other an internal diameter of 7.5 mm that was used with the 0.150 mm diameter wire to maintain adherence to assumption (3). A step was machined at each end of the tube, as shown in Figure 4.1, to

locate and retain the wire clamp, beside a cut at the bottom corner to allow access to fasten the machine screws of the clamps.

4.2.4 The magnet assembly

A magnetic field of 0.3 T was provided by two rectangular magnets, each with a length L_B = 31 mm located symmetrically along the wire of length L so that the ratio L/L_B = 1.3 was sufficient to suppress the second and third harmonics as reported by Wilhelm et al. [47]. The magnets were supplied by Magnet Sales & Services™, UK, fabricated from $Sm_2(Co, Fe, Cu, Zr, Hf)_{17}$ (known commonly as Sm2Co17 or 2:17) for which the Curie temperature is about 1098 K and the maximum operating temperature about 623 K with a very low reversible temperature coefficient of induction ≈ -0.0004 K^{-1} [70]. Thus, compared with other magnets materials, both the upper operating temperature is higher (by about 100 K) and the rate at which the field decreases with increasing temperature is lower.

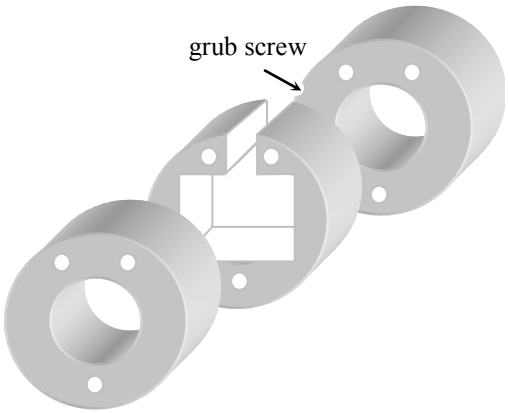

Figure 4.3: Schematic cross section of the rare earth permanent magnet envelop, constructed from type 413 stainless steel, consisting of one centre piece with a rectangular cutaway to accommodate the magnet blocks and two end rings to secure it with the tube.

The magnet blocks were encapsulated in an envelope assembly constructed from three martensitic stainless steel (grade 413) rings. As shown in Figure 4.3, these consists of one centre-piece, with a rectangular cut-away, to accommodate the two magnet blocks, and two end rings that clamp it to both the tube and wire holder.

To tune the vibrating wire with the magnetic field, frequency is swept at room temperature, in air, then any superimposed peaks can be eliminated by rotating the tube, while located inside the magnet assembly, until having a single smooth resonance peak, usually the highest one, as shown in Figure 4.4, then fixing the tube in position using a grub screw located on one of the outer rings.

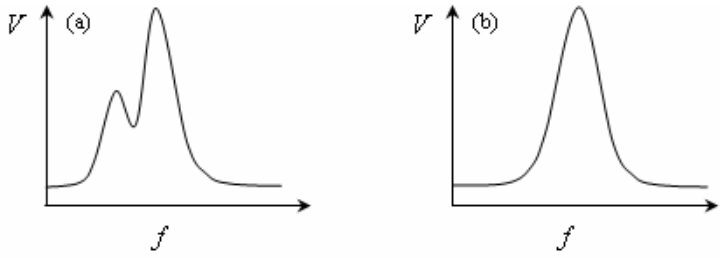

Figure 4.4: (a) signal before tuning; (b) signal after tuning.

4.3 Experimental setup:

As shown in Figure 4.5, the assembled vibrating wire was placed in a pressure vessel, fabricated from non-magnetic austenitic stainless steel grade 316, with a maximum operating pressure of up to 60 MPa at the highest operating temperature. The fluid flowed into and out of the apparatus through two ports located at the bottom and top of the vessel, respectively. The vessel was placed in an oil-filled stirred bath whose temperature was controlled with a precision of ± 0.01 K. The electrical connection through the pressure vessel to the vibrating wire was made with a Conax Buffalo™ electrical feedthrough shown in Figure 4.6. More details on vessel design equations and guidelines are included in ref [142].

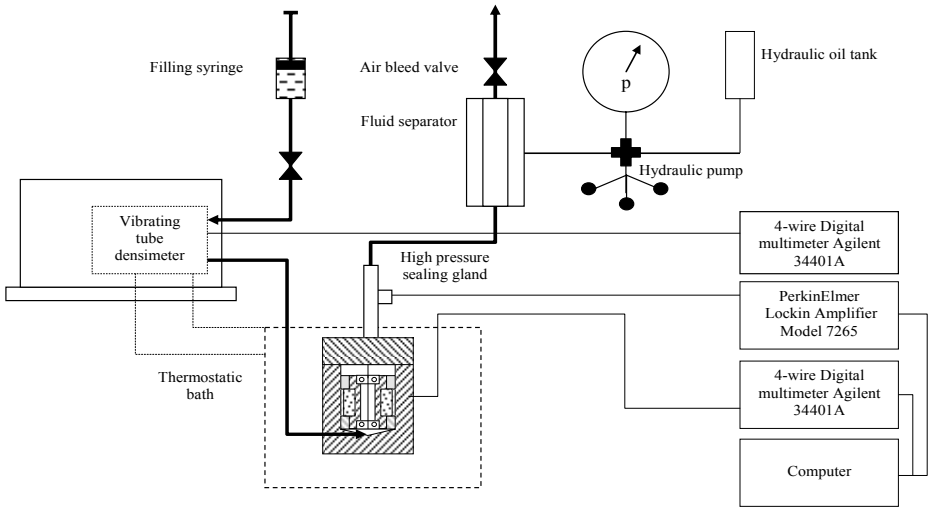

Figure 4.5: Experimental setup for viscosity measurements, including a high pressure densimeter for potential simultaneous measurements

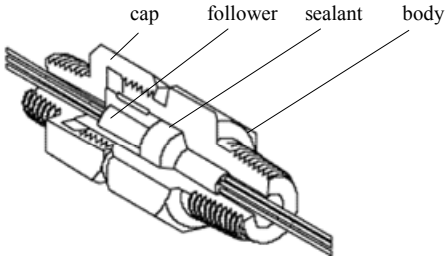

Figure 4.6: Schematic cross section of the high pressure sealing gland used for electrical feedthrough of the pressure vessel.

4.3.1 Temperature measurement:

The temperature of the pressure vessel was determined with a 4-wire industrial 25 Ω platinum resistance thermometer inserted in a well located in the pressure vessel. This thermometer had been calibrated against a 25 Ω standard platinum resistance thermometer made by Sensing Devices™ Ltd., UK that had been calibrated on ITS-90 by the Measurement Standard Laboratory of New Zealand in 2000. The resistance at the triple point of water R(273.15 K) of this standard thermometer was determined using a water triple point cell described by Goodwin et al. [71], as shown in Figure 4.7. More details on the calibration parameters are included in the appendix.

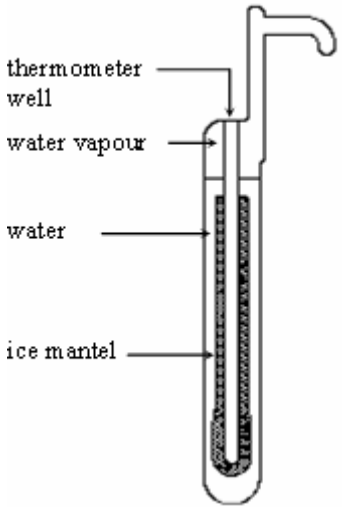

Figure 4.7: The cell used for calibrating the standard thermometer at the triple point of water.

The resistance of the measuring thermometer was determined with a digital multimeter Agilent™ 34401A, as shown in Figure 4.5, and converted to temperature with an uncertainty, including the calibration, $\delta T \approx \pm 0.01$ K.

4.3.2 Pressure measurement:

Pressure was generated with a hydraulic pump, as shown in Figure 4.5, and measured in the range (0.1 to 40) MPa, with a transducer that was calibrated against a force balance dead weight gauge (Desgranges et Huot™ model 21000). The uncertainty of pressure measurements has been determined as $\delta p \approx \pm 0.05$ MPa.

4.4 Fluid samples:

Three fluids were used for the measurements. Methylbenzene from Merck BDH™ Ltd had a mass fraction, determined by gas chromatography using both thermal conductivity and flame ionization detectors, of > 0.99917. There were two major impurities, benzene of mass fraction of 0.00031 and water of mass fraction 0.00023. Two certified reference materials for viscosity, N10 and N100 (nominal viscosities of (14 and 240) mPa·s at T = 298 K and p = 0.1 MPa) were obtained from Paragon Scientific™ Ltd U.K. with assigned lot numbers 531606 and 131202, respectively. The supplier measured the kinematic viscosity for both N10 and N100 at temperatures between (293 and 373) K using long-capillary Master viscometers according to ASTM D 2164. The supplier also provided density values at all temperatures measured in accordance with ASTM D 1480. The uncertainty in the kinematic viscosity was ± 0.25 % relative to water and the uncertainty in the density was ± 0.02 %.

4.5 Data acquisition and measurement procedure:

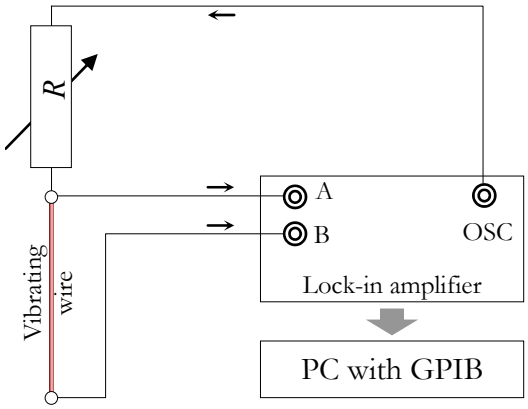

Figure 4.8: Electrical connection circuit of the vibrating wire to the lock-in amplifier.

The signal of the induced voltage was measured with a lock-in amplifier (PerkinElmer™ model 7265), as shown Figure 4.8, connected to a computer equipped with a general purpose interface board (GPIB) controlled by Agilent Vee™ data acquisition software.

The lock-in amplifier can detect and measure very small ac signals down to a few nanovolts and accurate measurements may be made even when the signal is obscured by noise sources a few thousand times larger than the measured signal. It uses a technique known as phase sensitive detection PSD to separate the components of the signal at a specific reference frequency and phase. Noise signals at frequencies other than the reference frequency are rejected and do not affect the measurements. A sinusoidal voltage generated by the lock-in amplifier's internal oscillator through the connector OSC, as shown in Figure

4.8, with a maximum output of 5 V ac, was passed through a variable resistance of about 1 kΩ connected in series to the tungsten wire so as to provide a constant current source. The induced ac voltage of the wire was measured as float through the connectors A and B on the lock-in amplifier.

The GPIB was also connected to the digital multimeter (Agilent™ 34401A) to measure the resistance of the 4-wire platinum thermometer and convert it to temperature via the computer software. The conversion equation and calibration parameters are included in the appendix. The pressure measurements were entered manually in the software as there was no convenient computer interface available to the Desgranges et Huot pressure gauge.

4.5.1 Frequency sweep:

The frequency generated by the lock-in amplifier synthesizer was stepped over the resonance frequency of the wire, and the in-phase and quadrature voltages $\boldsymbol{V}$ that included the motional emf $\boldsymbol{V}_2$ were determined with the lock-in amplifier over the frequency range ($f_r \pm 5g$), where g is half the resonance peak width at a frequency 0.707 times that of the maximum amplitude. The frequency sweep started at ($f_r - 5g$) with positive frequency steps to ($f_r + 5g$) and then with negative increments back to ($f_r - 5g$). It took about 200 s to finish this (forward and backward) sweep. Prior to acquiring $\boldsymbol{V}$, the majority of the

contribution arising from drive voltage $\boldsymbol{V}_1$ was removed by setting the lock-in amplifier offset voltage at $f < (f_r - 5g)$. The temperature was measured at each acquisition frequency and then averaged at the end of each forward and backward scan. The resonance peak was found with a quick sweep over a wide range, and then with a finer sweep over the selected range.

The lock-in amplifier can resolve frequencies to 0.01 Hz, but that would require increasing the delay after each step to around 10 s, hence increasing the sweep time which was not recommended in this experiment. However, the program was designed to perform frequency sweeps with a variable frequency step and delay in order to produce faster measurements in the region of the signal tails, and intense data in the region around the peak. A 'normalized' Lorentzian type equation [72] was used to calculate the expected amplitude of displacement, f_r, and g, hence determine the appropriate sweep width ($5g$).

4.5.2 Driving current:

The voltage was varied between (0.005 and 2000) mV and the resistance was varied between (0.1 and 5) kΩ to maintain the amplitude of the wire motion, estimated from the applied force and viscosity, to be less than 10 % of its radius. Thus, for a wire with a diameter of 0.15 mm in vacuum a driving current of 5 μA was used where 0.1 mA current was required when immersed in methylbenzene; 0.5 mA, when immersed in N10; and 3 mA, when

immersed in N100. For the 0.05 mm diameter wire immersed in methylbenzene, a driving current of 0.4 mA was used.

4.5.3 Calculation of viscosity from regression:

For each fluid temperature and pressure, the viscosity was obtained from a regression analysis for the measured complex voltage sampled by the lock-in amplifier using eq 3.55, where $\boldsymbol{V}$ was replicated, in real and imaginary components, by adjusting the parameters Λ, f_0, a, b, and c. The parameter Λ represented the amplitude which absorbed the magnetic field strength and the wire length. The parameters a, b, and c accounted for the electrical impedance of the wire and absorbed the offset used in the lock-in amplifier and the parameter f_0 represented the resonance frequency in vacuum. The reason why f_0 was chosen to be a float parameter is discussed in the next chapter. The regression technique used was the Levenberg-Marquardt nonlinear error minimising method which is based on the estimation of the variation of the gradient of the errors with respect to the variables to be solved. More details on this regression technique can be found in ref [73].

4.5.4 Measurements in vacuum:

The vibrating wire viscometer is, in principle, an absolute device that, in theory, requires no calibration. However, in practice, the wire radius R and internal damping Δ_0 cannot be determined to sufficient accuracy by

independent methods; hence they are determined by calibration. A measurement of the resonance bandwidth in vacuum was used to obtain the internal damping Δ_0 while a measurement on methylbenzene at a temperature of 298.15 K and a pressure of 0.1 MPa was used with the viscosity and density values of methylbenzene obtained from Assael et al. [23] to calibrate the wire radius R. These measurements gave R = 0.0246 mm and $\Delta_0 = 4.9 \cdot 10^{-5}$ for the wire with nominal diameter 0.05 mm, whereas for the 0.15 mm nominal diameter wire, R = 0.0746 mm and $\Delta_0 = 12.2 \cdot 10^{-5}$.

Chapter 5

RESULTS AND DISCUSSION

The complex resonance frequency was measured with the wire immersed in methylbenzene at temperatures of (298, 323, and 348) K; for the 0.05 mm diameter wire, the measurements were performed at pressures in the range from (0.1 to 11) MPa, while for the 0.15 mm diameter wire measurements were made at pressure in the range from (0.11 to 40) MPa. Over these temperature and pressure ranges, the resonance frequency increased with increasing temperature and decreased with increasing pressure to span a range from (1.85 to 2.41) kHz for the 0.05 mm diameter wire and a range from (0.80 to 1.55) kHz for the 0.15 mm diameter wire.

5.1 Error Sensitivity Analysis:

The sensitivity analysis in this section gives a quantitative answer on how much the viscosity would deviate as a response to the variation, or the uncertainty, in the other input parameters. As shown in Table 5.1, the uncertainty in temperature measurements of ± 0.01 K gave < 0.1 % in the viscosity over the whole range of measurements and an uncertainty of ± 0.05 MPa in pressure gave < ± 0.01 % in the viscosity of methylbenzene resulting from the error in calculating the density, while an uncertainty of ± 0.1 % in the

estimation of density gave a variation of less than ± 0.1 % in the measured viscosity.

Table 5.1: Sensitivity of the viscosity to the key parameters.

Parameter	Nominal value	Variation ±	Sensitivity % at $\eta \approx 0.5$ mPa·s	Sensitivity % at $\eta \approx 200$ mPa·s
Measurement parameters				
T		0.01 K	0.002	0.1
$p^{\dagger}$		0.05 MPa	0.06	--
$\rho^{\ddagger}$		0.1 %	0.09	0.02
Design parameters				
R	0.075 mm	1 %	1.9	1.9
L	40 mm	1 %	$< 1 \cdot 10^{-3}$	$< 1 \cdot 10^{-3}$
ρ_s	19300 kg·m^{-3}	0.1 %	0.17	0.12
Δ_0	$12 \cdot 10^{-5}$	1 %	0.05	$< 1 \cdot 10^{-3}$
B	0.3 T	10 %	$< 1 \cdot 10^{-3}$	$< 1 \cdot 10^{-3}$

† included only in methylbenzene measurements.
‡ calculated with correlation in ref [23]

The wire radius seemed to be the most significant design parameter, adding about ± 2 % to the uncertainty in the viscosity from only a variation of ± 1 %. This sensitivity to the wire radius was the same at $\eta \approx 0.5$ mPa·s and at $\eta \approx 200$ mPa·s supporting the assumption that the wire radius is independent of the viscosity of the fluid used for its calibration. The effect of the uncertainty of the wire density if taken as ± 0.1 % leads to an uncertainty of less than ± 0.2 % in the viscosity, while a variation of 1 % in the internal damping coefficient Δ_0 yielded a variation of about ± 0.05 % at $\eta \approx 0.5$ mPa·s and less than ± 0.001 % at $\eta \approx 200$ mPa·s which is expected as the contribution from the self damping

becomes insignificant compared to viscous damping at higher viscosities. The effect from the above tolerances in the magnetic field B and the wire length L is negligible as the variation in viscosity was < 0.001 %.

5.2 Upper limit of measurement:

As the fluid viscosity increases, the resonance quality factor Q {= $f/(2g)$} decreases and the signal becomes flatter and eventually the resonance width representing the viscosity cannot be resolved.

For the 0.05 mm diameter wire, Q varied from 23 at η (298 K, 10 MPa) ≈ 0.6 mPa·s to 37 at η (348 K, 0.1 MPa) ≈ 0.33 mPa.s, whereas for the 0.15 mm diameter wire Q varied from 41 at η (298 K, 40 MPa) ≈ 0.75 mPa·s to 90 at η (348 K, 0.1 MPa) ≈ 0.33 mPa·s. The value of Q obtained from the 0.15 mm diameter wire was always larger than that of the 0.05 mm diameter wire. Solely on the basis of these values of Q, it is suggested that the upper operating viscosity of the 0.15 mm diameter wire is greater than that of the 0.05 mm diameter wire.

Measurements were made with the 0.15 mm wire to determine its upper limit of viscosity measurements using both standard fluids N10 and N100. These measurements were performed at a pressure of 0.1 MPa and at temperatures corresponding to the temperatures at which the density and viscosity were provided by the supplier. As shown in Figure 5.1, for N10 and N100, Q

decreased from 36, with N10 at 373 K and η (373 K, 0.1 MPa) ≈ 2 mPa·s, to 3.2, with N100 at η (313 K, 0.1 MPa) ≈ 99 mPa·s. Measurements were also performed with N100, where η (305.8 K, 0.1 MPa) ≈ 149 mPa·s and Q was found to be 2.3 and η (305 K, 0.1 MPa) ≈ 200 mPa·s and Q was found to be 1.9.

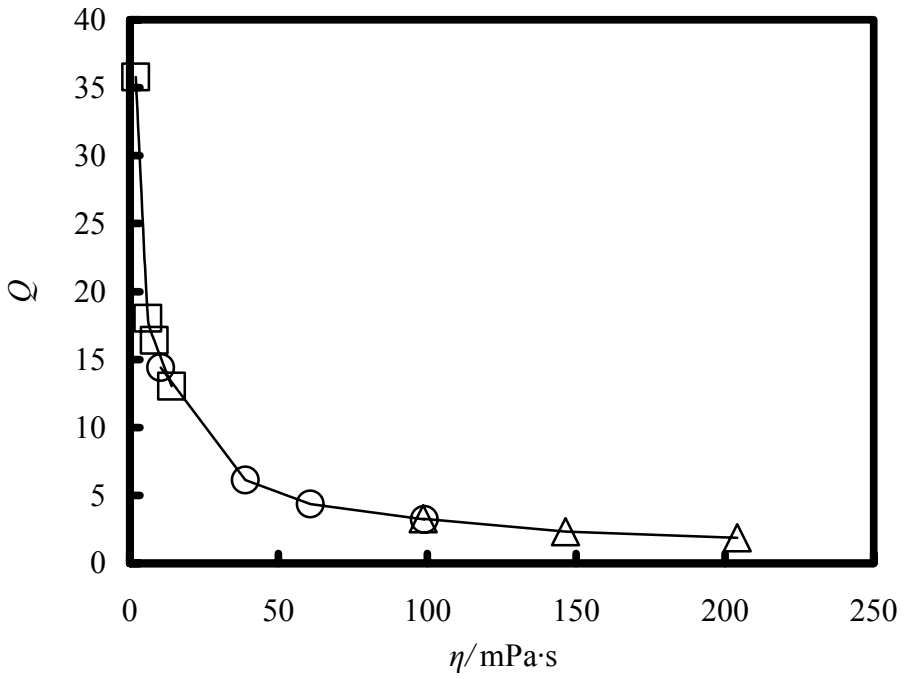

Figure 5.1: Quality factor Q decreases exponentially from (35 to 2) and becomes almost flat, as the viscosity increases from (2 to 200) mPa·s measured with 0.15 mm wire at: □, T = (373 to 298) K for fluid N10; ○, T = (373 to 313) K for fluid N100; △, T = (313 to 301) K for fluid N100.

These results demonstrate that increasing the wire diameter to 0.15 mm allowed the measurements to be performed with fluids of viscosities up to 200

mPa·s with results within 2 % of the reference value. This difference was within the uncertainty of the measurement, which, at $\eta \approx 200$, increased to 3 %.

5.3 Effect of sweep time and driving current:

When using this forced mode of oscillation, careful attention was given to the frequency sweep time and the driving current in order to keep the dissipated electrical energy as minimal as possible, thus avoiding a temperature rise in the fluid. For the W wire {c_p(W, 298 K) ≈ 133 J·kg^{-1}·K^{-1} and ρ(W, 298 K) ≈ 19300 kg·m^{-3}}, where c_p is the specific heat. A W wire of diameter 0.15 mm and mass $14 \cdot 10^{-6}$ kg has a resistance of order 1 Ω, and in vacuum, a current of 5 μA results in a temperature increase of < 3 μK over the 200 s data acquisition time. When the 0.15 mm diameter wire was immersed in N100 {c_p(298 K) ≈ 2 kJ·kg^{-1}·K^{-1}, ρ(298 K) ≈ 840 kg·m^{-3}, and λ ≈ 120 mW·m^{-1}·K^{-1}}, where λ is the coefficient of heat transfer, with the highest current of 3 mA, over the 200 s acquisition time, the estimated fluid temperature rise would be 0.7 mK {assuming that all electrical energy is dissipated into the fluid volume enclosed by the wire holder (about $1.8 \cdot 10^{-6}$ m^3)}, and the resulting error in viscosity at T = 313 K, where $\eta \approx 100$ mPa·s and $d\eta/dT \approx -3.8$ mPa·s·K^{-1}, would be ≈ 0.003 %. For both the other fluids and the 0.05 mm diameter wire, the estimated error in viscosity arising from self-heating is << 0.003 %. The temperature rise resulting from the wire motion within the fluid was always negligible.

5.4 Measurements in vacuum (Δ_0 and f_0)

Although values of f_0 and Δ_0 were determined experimentally, it was found that f_0 should not be given a fixed value, as will be explained next, hence was allowed to be a float parameter in the regression to eq 3.55. Had f_0 been fixed in the analysis to a value determined at $p = 0$ for each temperature as shown in Figure 5.2, the viscosities determined would have deviated from the literature values by up to 50 %.

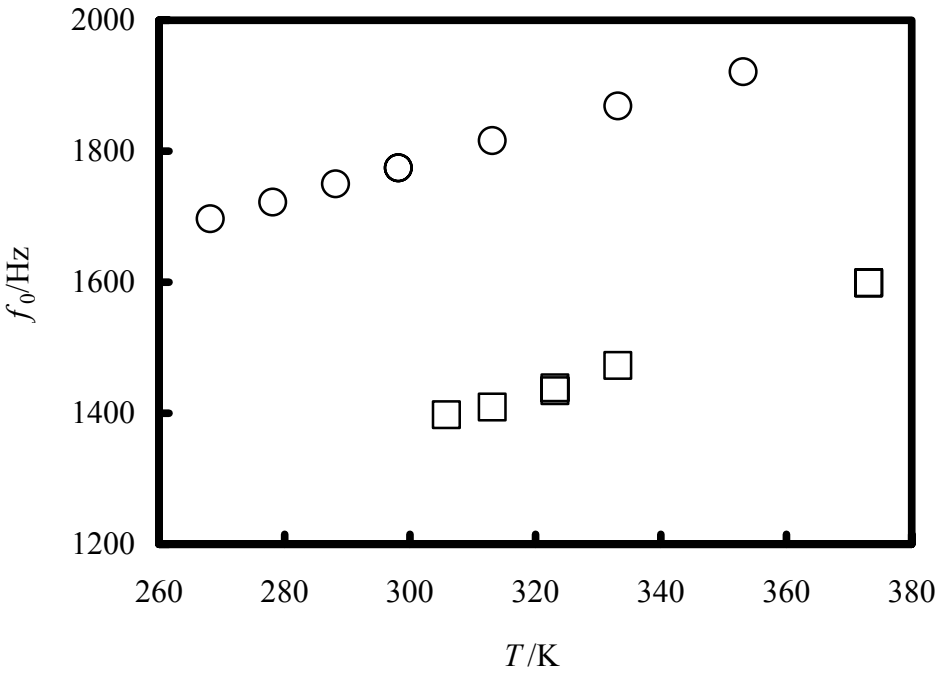

Figure 5.2: Change in vacuum resonance frequency f_0 with respect to T, using the 0.15 mm wire: ○, experimental f_0 measured in vacuum; □, calculated f_0 as a float parameter from regression to eq 3.55.

The values of f_0, the vacuum frequency of the wire determined from the regression analysis to eq 3.55, varied linearly with temperature for the 0.15 mm diameter wire of $(\partial f_0/\partial T)_p \approx 4$ Hz·K^{-1} , whereas for the 0.05 mm diameter wire we observed $(\partial f_0/\partial T)_p \approx 9$ Hz·K^{-1} . These values are about a factor of 2 less than the result anticipated solely from the variation in the wire tension that would arise from the difference in linear thermal expansion coefficients between tungsten and Macor® mentioned in Chapter 4.

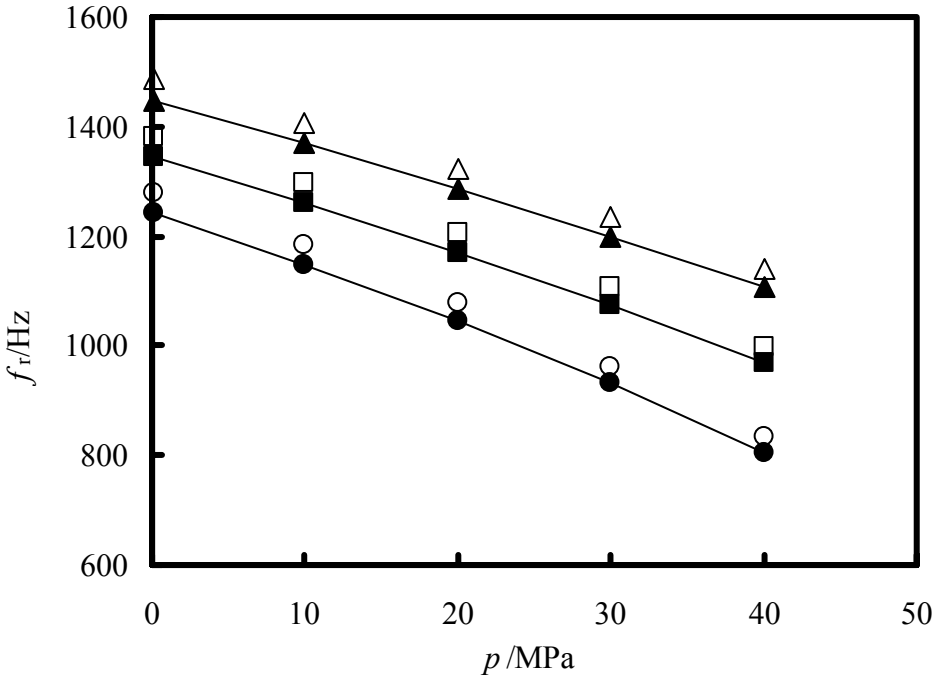

Figure 5.3: Change in resonance frequency f_r with pressure at different isotherms measured in methylbenzene: ▲, 348 K; ■, 323 K; ●, 298 K; and corresponding vacuum resonance frequencies f_0 obtained from regression as float parameters at the same isotherms, △, 348 K; □, 323 K; ○, 298 K.

The calculated values of f_0 decreased with increasing pressure with $(\partial f_0/\partial p)_T \approx$ -11 Hz·MPa^{-1} maintaining its difference from the resonance frequency almost constant as shown in Figure 5.3. No experiments were performed to identify the source of this observed variation; plausible sources include the rotation of one wire clamp relative to the other. Clearly, allowing f_0 to float in the regression is important for the accurate determination of viscosity and was included in our analysis.

5.5 Results for Methylbenzene:

The viscosities of methylbenzene obtained with both the (0.05 and 0.15) mm diameter wires are listed in Table 5.2 and Table 5.3, respectively, and are shown as deviations from the correlation of Assael et al. [23] in Figure 5.4. These results lie within ± 1 % of the values in ref 23. Figure 5.5 shows the same deviations for all of the literature values listed in Table 5.4. The literature values that were obtained with experimental techniques that utilized different principles and lie within ± 4 % of the values reported in ref [23]. Comparison with recent (2003) data from Avelino et al. [33] gave also good agreement, as shown in Figure 5.6.

5.6 Results for standard fluids:

For the two standard fluids, N10 and N100, a nominal wire diameter of 0.15 mm was used, and the results obtained with these fluids are listed in Table 5.5

along with the relative differences from the manufacturer's values, shown in Figure 5.7, that never exceeded ± 1 % for viscosities up to 100 mPa·s. The viscosities were obtained using R = 0.0747 mm determined from measurements with the standard fluid N10 at T = 373 K where $\eta \approx 2$ mPa·s. This value was 0.1 μm greater than that determined with methylbenzene, and had we used the lower value, the viscosities would have differed by < 0.7 % from those reported in Table 5.5. The measurements with N100 at a temperature of T = 301 K gave $\eta \approx 204.2$ mPa·s, which is 1.9 % above the value cited by the supplier, whereas at T = 305.8 K the vibrating wire gave $\eta \approx$ 146.5 mPa·s, which lies 2.2 % below a value interpolated from the supplier's values. These differences are within the uncertainty of the measurements, which, at these viscosities, was estimated to be 3 %. These results were used to determine the upper operating viscosity and are not reported in Table 5.5 or shown in Figure 5.7.

Table 5.2: Viscosity η of methylbenzene measured with the 0.05 mm diameter vibrating wire as a function of temperature T and pressure p along with values of density ρ determined from the correlation of Assael et al. [23]

T/K	p/MPa	ρ/kg·m^{-3}	η/mPa·s
298.15	0.1	862.6	0.555[a]
	2.11	864.1	0.565
	4.10	865.7	0.574
	6.10	867.2	0.585
	8.11	868.7	0.594
	10.11	870.1	0.602
323.15	0.1	839.2	0.419
	2.08	841.0	0.429
	4.11	842.8	0.435
	6.00	844.4	0.441
	8.12	846.2	0.449
	10.05	847.9	0.455
	12.21	849.6	0.464
	15.00	851.9	0.474
348.15	0.1	815.2	0.333
	2.12	817.3	0.338
	12.11	827.1	0.366
	15.21	830.0	0.376

[a] calibration point.

Table 5.3: Viscosity η of methylbenzene measured with a 0.15 mm diameter vibrating wire as a function of temperature T and pressure p along with values of density ρ determined from the correlation of Assael et al. [23]

T/K	p/MPa	ρ/kg·m^{-3}	η/mPa·s
298.15	0.1	862.6	0.555[a]
	10	870.1	0.600
	20	877.1	0.645
	30	883.6	0.695
	40	890.0	0.751
323.15	0.1	839.2	0.422
	10	847.8	0.457
	20	855.8	0.495
	30	863.2	0.531
	40	870.4	0.572
348.15	0.1	815.2	0.329
	10	825.2	0.358
	20	834.4	0.388
	30	842.7	0.417
	40	850.7	0.448

[a] calibration point.

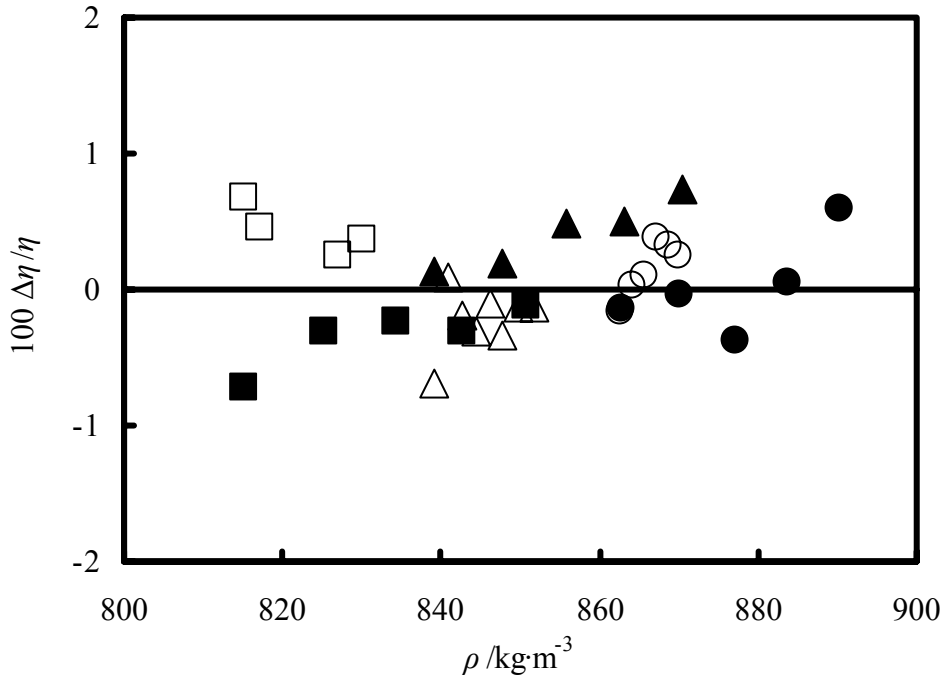

Figure 5.4: Fractional deviation $\Delta\eta/\eta = (\eta_{exptl} - \eta_{calc})/\eta_{calc}$ of the experimental viscosity for methylbenzene η_{exptl} measured as a function of T and p from the correlation of Assael et al. [23], η_{calc} as a function of density ρ. ○, T = 298.15 K with wire diameter ≈ 0.05 mm; ●, T = 298.15 K with wire diameter ≈ 0.15 mm; △, T = 323.15 K with wire diameter ≈ 0.05 mm; ▲, T = 323.15 K with wire diameter ≈ 0.15 mm; □, T = 348.15 K with wire diameter ≈ 0.05 mm; and ■, T = 348.15 K with wire diameter ≈ 0.15 mm. The scale of the ordinate axis is equal to the cited uncertainty of the correlation [23].

Table 5.4: Measurements of the viscosity η_{exptl} of methylbenzene reported in the literature and obtained with a vibrating wire (VW), oscillating disk (OD), falling body (FB), surface light scattering (SLS), rolling ball (RB), capillary (CP), and torsional vibrating crystal (TVC) viscometer over a temperature range T at maximum pressures p with estimated uncertainty u along with the source of the density and the maximum deviations ($\Delta\eta = \eta_{exptl} - \eta_{calcd}$) of η_{exptl} from the viscosity calculated with the correlation reported in ref [23]. η_{calcd} at temperatures T between (298 and 348) K and pressure $p < 40$ MPa that cover this work.

ref	T_{min} to T_{max} / K	p / MPa	$100\Delta\eta / \eta_{calc}$	±100u[1]	method	Density obtained from
33	222 to 348	80	1.1	3	VW	measured simultaneously with buoyant mass
17	201 to 370	0.1	0.64	0.5	VW	ref 74
18	210 to 370	30	1.12	0.5	VW	ref 23
28	213 to 298	20	0.71	1.5	VW	ref 23
22	303 and 323	70	0.52	0.5	VW	ref 75
43	303 to 348	250	2.34	0.5	VW	ref 75
76	298 to 373	200	[2]	0.5	TVC	ref 75
77	298 to 348	110	[2]	2	TVC	ref 77
78	298 and 323	375	0.65	2	FB	ref 78
79	298 to 423	30	0.66	0.5	OD	ref 75
80	263 to 383	0.1	0.57	1	SLS	ref 81
82	255 to 323	400	0.26	1	FB	pycnometer
83	298 to 368	0.1	1.19	0.5	CP	pycnometer
84	288 to 373	0.1	0.69	0.5	CP	pycnometer and volumeter
85	298 to 373	500	0.91	4	FB	ref 85
86	298 to 323	500	1.29	5	FB	ref 85
87	298 to 363	100	3.49	1	FB	Anton Paar densimeter
88	298 to 348	0.1	0.92	0.5	CP	ref 75
89	218 to 378	0.1	0.48	1.4	CP	ref 23
90	298 to 373	200	0.99	0.5	TVC	ref 75
91	303 to 333	0.1	3.51	--	CP	pycnometer
92	293 to 353	0.1	0.51	0.2	CP	pycnometer
[3]	298 to 348	40	0.69	0.6	VW	ref 23
[4]	298 to 348	40	0.74	0.6	VW	ref 23

[1] uncertainties (u) cited by authors of the original work,
[2] only smoothing equation provided,
[3] this work 0.05 mm wire,
[4] this work 0.15 mm wire.

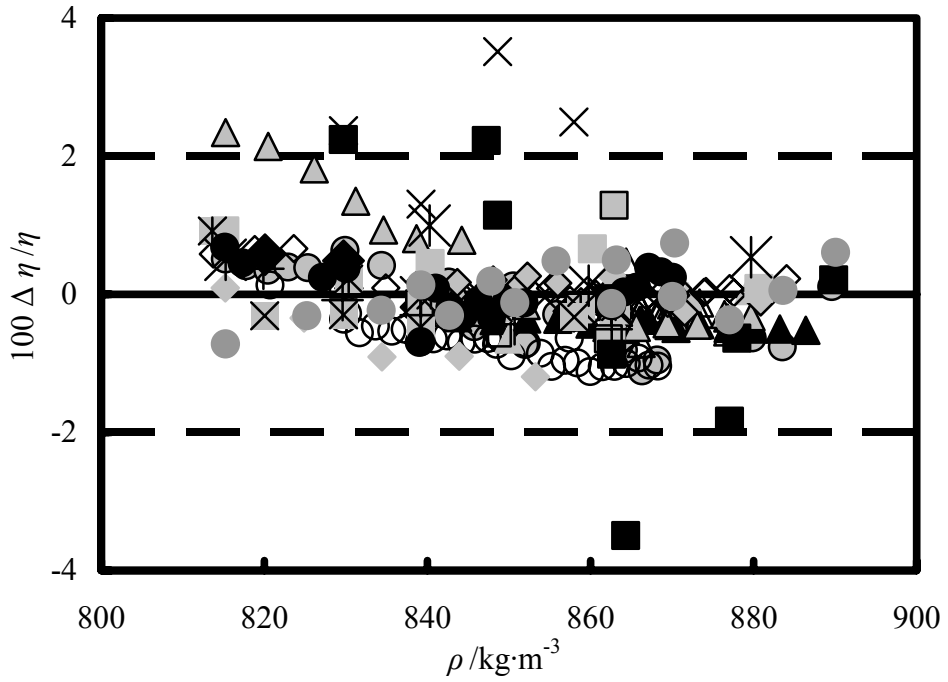

Figure 5.5: Fractional deviation $\Delta\eta/\eta = (\eta_{exptl} - \eta_{calc})/\eta_{calc}$ of the viscosity η_{exptl} for methylbenzene from the correlation reported by Assael et al. [23] η_{calc}, at T from (298 to 348) K and p from (0.1 to 40) MPa, as a function of density ρ. ●, our results with wire diameter ≈ 0.15 mm; ●, our results with wire diameter ≈ 0.05 mm; gray filled circle with black outline, ref [33]; ○, ref [18]; △, ref [28]; ▲, ref [22]; gray filled triangle with black outline, ref [43]; ▲, ref [78]; ◇, ref [79]; ♦, ref [80]; gray filled diamond with black outline, ref [82]; gray filled diamond, ref [83]; □, ref [84]; ■, ref [85]; gray filled square with black outline, ref [86]; ■, ref [87]; gray filled square containing cross, ref [88]; gray filled square containing x , ref [89]; cross, ref [90]; x, ref [91]; +, ref [92]. The dashed lines are the estimated uncertainty of ref [23].

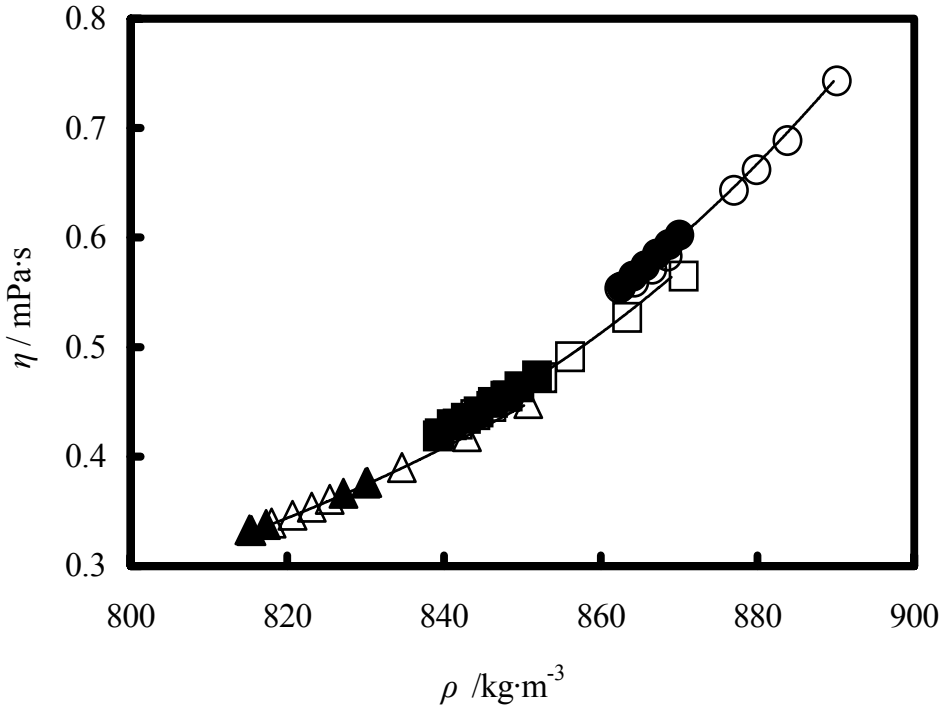

Figure 5.6: Viscosity η as a function of density ρ for methylbenzene. ●, This work, 298.15 K; ○, Avelino et al. [33] at $T = 298.15$ K; ■, this work $T = 323.15$ K; □, Avelino et al. [33] at $T = 323.15$ K; ▲, this work $T = 358.15$ K; △, Avelino et al. [33] at $T = 358.25$ K; and the lines ——, calculated from the correlation reported by Assael et al. [23].

Table 5.5: Experimental viscosity η_{exptl} of two standard fluids N10 and N100 determined with a vibrating wire viscometer with wire of nominal diameter of 0.15 mm, at p = 0.1 MPa along with fractional deviations $100(\eta_{exptl} - \eta_{calc})/\eta_{calc}$ from the manufacturer's values η_{calc} as a function of temperature

Fluid	T/K	η_{exptl}/mPa·s	$100\Delta\eta/\eta_{calc}$
N10	373.15	2.088	0.000[a]
	323.15	6.13	0.459
	313.15	8.25	0.258
	298.15	14.1	0.531
N100	373.15	10.5	-0.694
	333.15	38.8	0.036
	323.15	60.7	0.878
	313.15	99.0	0.013

[a] calibration point.

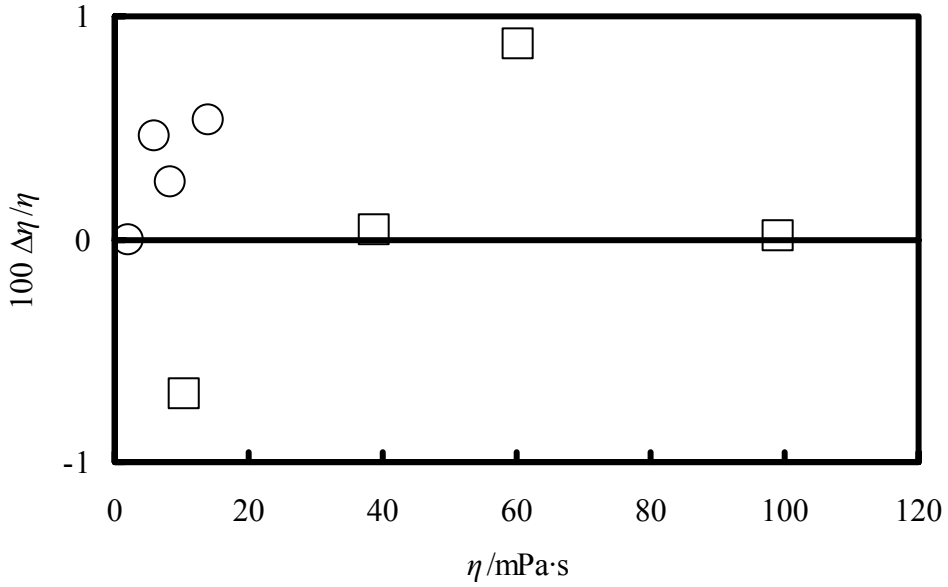

Figure 5.7: Fractional deviation $\Delta\eta/\eta = (\eta_{exptl} - \eta_{calc})/\eta_{calc}$ of the viscosity η_{exptl} for two fluids with η (298 K, 0.1 MPa) ≈ 14 mPa·s and η (298 K, 0.1 MPa) ≈ 240 mPa·s determined with the vibrating wire of diameter ≈ 0.15 mm η_{exptl} from the values provided by the supplier η_{calc} as a function of viscosity η_{calc}. For each fluid, the viscosity increases with decreasing temperature in the range from (298 to 373) K. □, η (298 K, 0.1 MPa) ≈ 240 mPa·s; ○, η (298 K, 0.1 MPa) ≈ 14 mPa·s.

Part II

The Microwave Cavity Resonator

Nomenclature:

C	Capacitance
C', C''	Capacitances associated with fringing fields at the upper and lower ends of the annular gap section
f	Frequency
g	Half width of resonance curve
k_B	Boltzmann's constant
k_{ij}	Binary interaction parameter
L	Length; Inductance
N_A	Avogadro's constant
p, p^d	Pressure; Dew pressure
Q	Quality factor of resonance curve
R	Resistance
S_{11}, S_{22}	Microwave Input and Output reflection coefficients
S_{12}, S_{21}	Microwave Reverse and Forward transmission coefficients
T, T^d	Temperature; Dew temperature
V	Volume
x	Mole fraction
Z	Impedance
Z', Z''	Impedances associated with the radial current flow in the upper and the lower surface of the inductive section.

Greek symbols:

β_1, β_2	Coupling coefficients
ε	Relative permittivity
Є	A function of ε representing the liquid volume fraction
μ	Dipole moment
$\wp$	Molar polarizability
ρ	Density
ω	Angular frequency

Definition of subscripts:

0	In vacuum
00	In vacuum at an arbitrary room temperature
c	Critical; Capacitive
c1, c2	T-equivalent parameters of wave guide for capacitive section
calc	Calculated
expt	Experimental
g	Gas
l	Liquid; Inductive
i, j	Components i and j
mix	Mixture
r	Resonance, Reduced
t	Toroidal section
t1, t2	T-equivalent parameters of wave guide for toroidal section
tot	Total cavity volume

Boldface denotes a vector quantity.

Chapter 6

LITERATURE REVIEW

6.1 Previous designs:

The non-visual methods used to determine phase behaviour and that are particularly suited to automation and require small sample volumes (<100 cm^3), are: measurements of the refractive index with fibre-optic cables [93], evanescent waves at GHz frequencies [94], and relative permittivity [95,96, 97,98] determined with a microwave cavity resonator. The latter method, the cavity resonator, has been used since Goodwin et al. [98] developed a rigorous model that relates the geometry of the cavity and the dielectric properties to the resonance frequency. The application of this method has been extended to electrically conducting liquids, such as water, using a two-lobe design [99,100] and a three-lobe design [101]. The multi-lobe design was primarily used to ensure that the measured relative permittivity was independent of frequency.

The basic single-lobe design by Goodwin et al. has been used with remarkable success for the measurements of phase boundaries [98] and the measurements of dipole moments [102] and its application has been extended to determine the density [103] in the single phase region. Prior to the start of this study, the method had not been used to measure the liquid volume fractions in the

coexisting gas-liquid phase region and its use has been limited to isochoric measurements. Recently, a modified version of the cavity resonator with a variable volume, capable of isothermal and isobaric measurements in addition to isochoric measurements, was developed by May et al. [104]. This apparatus was optimised to measure small liquid volume fractions in the coexisting gas-liquid phase. It was equipped with a post of 2 mm diameter protruding down from the tip of the bulb, into a well of 6 mm diameter centered on the bottom of the outer cylinder. The post terminated 0.2 mm above the bottom of the well. That 'mini' chamber was introduced to perform as a cylindrical capacitor sensitive to liquid volumes that build up at the bottom of the cavity. This apparatus was successful in the isothermal mode in providing fast measurements for the phase boundary and liquid volume compared to the 'relatively slow' isochoric mode. However, it suffered from problems with excessive liquid hold-up and deficiencies in drainage due to inadequate design of the re-circulation pump, resulting in the introduction of errors in liquid volume measurements.

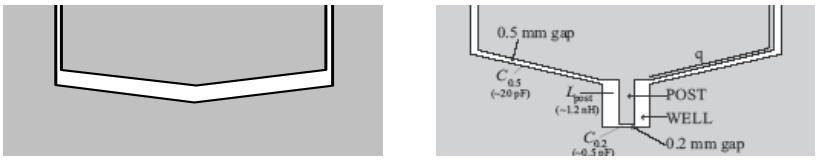

Figure 6.1: Schematic for the extra capacitor section developed at the cavity bottom in ref [104] as shown to the right, while the original design [98] is shown to the left.

The cavity resonator, developed in this project, has also been used to measure the liquid volume fractions, in the coexisting gas-liquid phase, but without introducing any extra capacitors to the design originated by Goodwin et al. [98]. The capacitor formed from the lower gap section located between the bulbous bottom surface and the outer cylinder, with a clearance of 5 mm, was found to provide sufficient information on the liquid volume fractions accumulated in the bottom of the cavity. The clearance of this capacitance was modified to 0.5 mm in May et al. [104], as shown in Figure 6.1 . The original design, with simple adaptation to the drainage system, has provided accurate measurements for small liquid volume fractions as discussed in Chapter 9.

Two main CEOS were used in this project to compare with the experimental results, Peng-Robinson (PR) [105] and Soave-Redlich-Kwong (SRK) [106] equations of state. These were selected because they are the most widely used cubic equations of state in the refinery and gas processing industries for the prediction of vapour-liquid equilibria. A recent review of advanced cubic equations of state, with emphasis on the strengths and limitations, given by senior developers from Aspen Technology, can be found in ref [107]. Parameters of PR and SRK equations of state (eq 1.12) were obtained from refs [108, 109] and are listed in Table 1.3.

6.2 Previous experimental results

The operation of the cavity resonator, developed in this project, was demonstrated with measurements of the dew pressures, gas phase densities, and liquid volume fractions in the coexisting vapour-liquid phase, for $\{0.4026CH_4 + 0.5974C_3H_8\}$ at temperatures in the range (315 to 340) K. There are eight publications, to the author's knowledge, [104, 110, 111, 112, 113, 114, 115, 116] that report the phase behaviour of $\{(1-x)CH_4 + xC_3H_8\}$ at temperatures in the range (273 to 363) K. References [111-116] report results obtained from (p, V, T, x) measurements, while reference [110] reports dew pressures obtained with a dual-sinker densimeter, and reference [104] used the cavity modified to optimise the determination of liquid drop-out-volume by May et al. [104]. The experimental data obtained from this work and those from previous work (at $T > 273.15$ K) have been plotted on the same chart shown in Figure 6.2 to demonstrate the covered range of measurements.

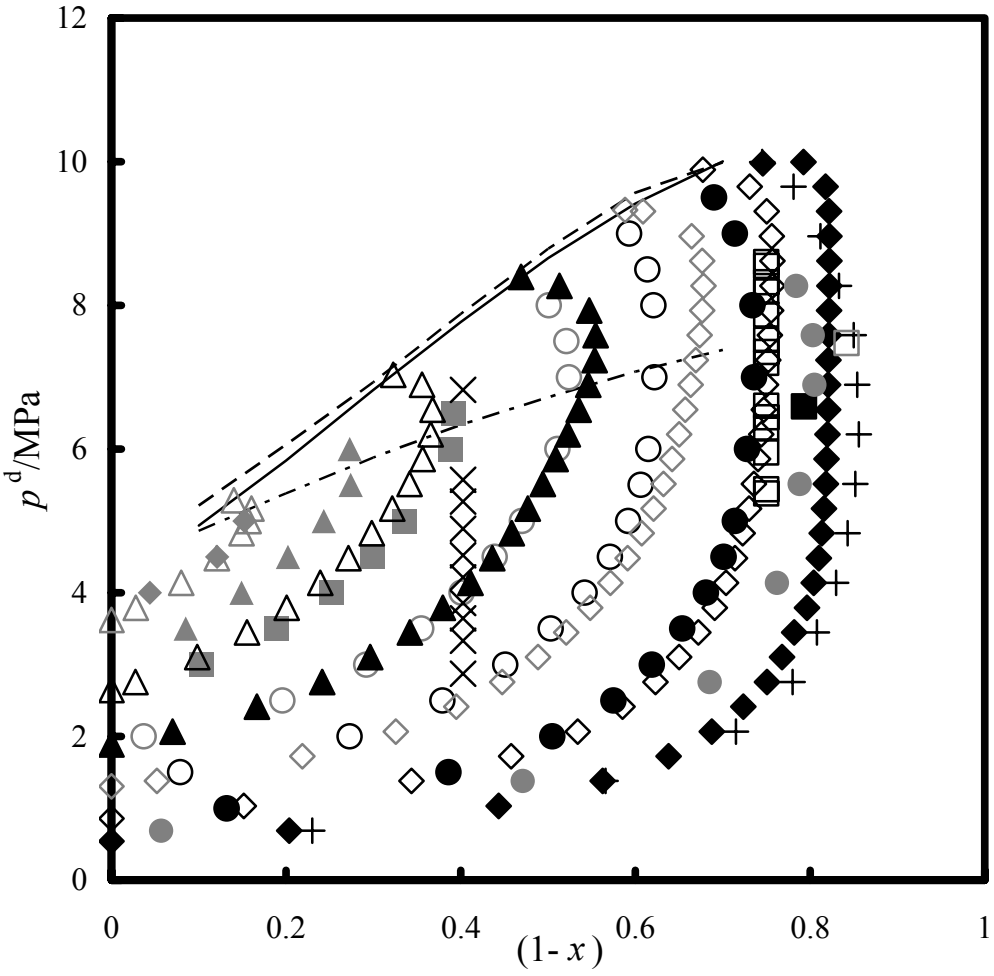

Figure 6.2: Dew pressure p^d for $\{(1 - x)CH_4 + xC_3H_8\}$ as a function of $(1 - x)$. X, this work; □, [104] microwave resonator; ■, [110] dual sinker densimeter at $T = 284.6$ K; □ (gray outline), [110] dual sinker densimeter at $T = 272.9$ K; ●, [111] $T = 293.15$ K; ○, [111] $T = 313.15$ K; ○ (gray outline), [111] $T = 328.15$ K; ■, [111] $T = 343.15$ K; ▲, [111] $T = 353.15$ K; ◆, [111] $T = 363.15$ K; ◆, [112] $T = 277.59$ K; ◇ (gray outline), [112] $T = 310.93$ K ; △, [112] $T = 344.26$ K; ▲, [112] $T = 327.59$ K; △ (gray outline), [112] $T = 360.93$ K; ◇, [112] $T = 294.26$ K; ●, [113] $T = 283.15$ K; +, [116] $T = 273.15$; — —, [111] critical data; ——, [112] critical data; — · —, [111] cricondentherm.

Chapter 7

THEORY AND WORKING EQUATIONS

This chapter includes the working equations used to determine the relative electric permittivity (dielectric constant, or relative permittivity) of a fluid within a microwave resonator from the measurements of the resonant frequency, and the equations relating the relative permittivity to thermodynamic properties. Dielectric theory is presented in detail in refs [117,118].

7.1 Simple *LC* oscillator model

From the analysis of the resonance *LCR* circuit, the resonance frequency f_r can be given as a function of inductance L and capacitance C as:

$$2\pi f_r = 1/\sqrt{LC}\,, \tag{7.1}$$

and a quality factor Q given by:

$$Q = 2\pi f_r L / R\,. \tag{7.2}$$

where R is the electrical resistance. When the re-entrant resonator is filled with an electrically non-conducting fluid of relative permittivity ε, it becomes

electrically equivalent to an *LCR* network with a resonance frequency f_r and half-width g given approximately by:

$$2\pi(f_r - ig) \approx \frac{1}{\sqrt{\varepsilon LC}} - \frac{1-i}{2L}R\,, \tag{7.3}$$

where R is an equivalent series resistance ≈ 0.040 Ω. The inductance L is determined from the toroidal volume denoted as L_t and the capacitance C is determined from the narrow annular gap denoted as C_1 since they have the largest LC product as shown in Figure 7.1.

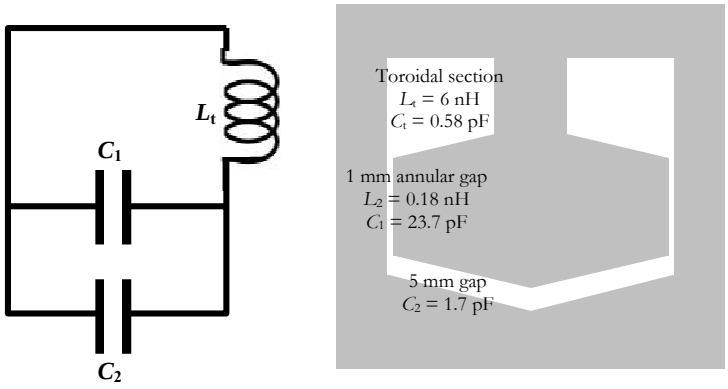

Figure 7.1: Schematic cross-section through the resonator represented as inductance toroidal volume L_t; annular gap section capacitance C_1, lower capacitance C_2.

This simple *LCR* model suffices for the purpose of determining phase boundaries from the change in the resonance frequency. However, for the calculation of density, the complete model developed by Goodwin et al. [98]

can be used to calculate accurate values for relative permittivity as discussed in the following section.

7.2 Wave guide model

7.2.1 Distributed-parameters model

The rigorous theoretical model, based on coaxial waveguide theory and developed by Goodwin et al. [98], accounted for all of the products L_iC_i including additional contributions from fringing fields, induction effects for the capacitors, and capacitive effects for the inductors, and contribution from the 5 mm gap at the bottom of the cavity. The cavity resonator was modelled as two sections of coaxial waveguide terminated at the lower end by a cylindrical capacitor illustrated Figure 7.2. The T-equivalent parameters Z_{t1} and Z_{t2} represent the toroidal section, and the parameters Z_{c1} and Z_{c2} represent the capacitive section. The capacitance associated with fringing fields at the upper ends of the capacitive section C' is calculated from Marcuwitz [119]. The terminal capacitance C_e is the sum of a similar fringing term C'' and the capacitance C_2 of the cylindrical capacitor at the bottom of the resonator. The impedances Z' and Z'' are associated with radial current flow in the upper and lower surfaces of the inductive section, respectively.

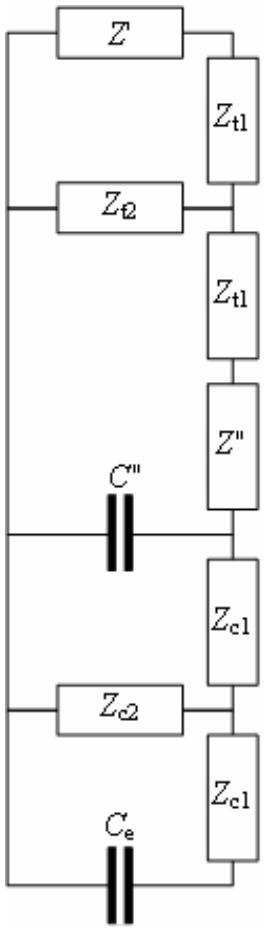

Figure 7.2: Schematic representation for the circuit parameters based on the wave guide model.

The inductance and capacitance of each section are calculated from the resonator dimensions using formulas from reference [98] as function of relative permittivity ε, and the condition of resonance is calculated from:

$$4\pi^2 (f_r + ig)^2 \approx \frac{1-(1-i)\omega R_t C_4}{L_t\left(C_4 + \frac{C_t}{3}\right) + L_c\left(C_e + \frac{C_1^2}{3C_4} - \frac{C_e C'}{C_4}\right)} \qquad (7.4)$$

where $C_4 = C_1+C'+C''+C_2$, which predicted a resonant frequency of 360 MHz in vacuum, very close to the experimental value of 350 MHz.

7.2.2 Lumped-parameter model

Instead of using the distributed-parameter model shown above, a lumped-parameter model, developed by Hamelin et al. [120, 121] has been used as recommended by NIST investigators where careful measurements for the cavity dimensions are no more required. Providing no corrections required for the effect of external coupling, due to the very weak coupling employed in this resonator, the relative permittivity is calculated as:

$$\varepsilon = \left(\frac{f_0 + \mathrm{i}\, g_0}{f_\mathrm{r} + \mathrm{i} g} \right)^2 \left(\frac{1 + (-1 + \mathrm{i}) Q^{-1}}{1 + (-1 + \mathrm{i}) Q_0^{-1}} \right) \tag{7.5}$$

where the quality factor $Q = f/2g$, and the subscript '0' denotes the vacuum condition. This equation can be applied to directly determine the relative permittivity from f_r, g, f_0, and g_0 measurements, as long as external coupling is sufficiently weak, fluid electrical conductivity is small, and Q is sufficiently large so that terms in Q^{-2} are negligible.

7.3 Measurement of the resonant frequency:

An Agilent™ vector network analyser (VNA) was used to measure the complex transmission of the cavity resonator by sampling the incident signal,

separating the transmitted and reflected waves, and then performing ratios that are directly related to the reflection and the transmission coefficients while sweeping the frequency to rapidly obtain real and imaginary components over the band of frequency of interest. The resonant frequency is related to the complex forward transmission coefficient known as $\boldsymbol{S}_{21}$, defined as the complex ratio of the voltage transmitted through the cavity to the voltage incident on it, for the lowest order non-degenerate *LC* mode. The measured real $\Re$ and imaginary $\Im$ components were fit, using the least squares error method, to the theoretical expression for the resonance [122] of the cavity given by:

$$\Re(\boldsymbol{S}_{21}) = \frac{2\sqrt{\beta_1\beta_2}\,(1+\beta_1+\beta_2)}{(1+\beta_1+\beta_2)^2 + \left(\frac{2\Delta f}{f_r}\right)^2 Q^2},$$

and (7.6)

$$\Im(\boldsymbol{S}_{21}) = \frac{-2\sqrt{\beta_1\beta_2}\left(\frac{2\Delta f}{f_r}\right)Q}{(1+\beta_1+\beta_2)^2 + \left(\frac{2\Delta f}{f_r}\right)^2 Q^2}.$$

where f_r is the resonance frequency of the *LC* mode, Q $\{=f_r/2g\}$ is the quality factor, g is half the resonance line-width, and $\Delta f = f - f_r$ where f is a frequency near f_r.

In eq 7.6, β_1 and β_2 are coupling factors given by:

$$\beta_1 = \frac{n^2 R}{R_s}, \qquad \beta_2 = \frac{m^2 R}{R_D}, \tag{7.7}$$

where R is the resistance of the resonator, R_S the resistance of the source, R_D the resistance of the detector and n and m are the effective turns ratio of the source and detector, respectively. The resonator is under coupled if $\beta < 1$, critically coupled if $\beta = 1$, and over coupled if $\beta > 1$. In this work, β_1 and β_2 are $<< 1$.

The $\boldsymbol{S}_{21}$ model, shown in eq 7.6, is different from what had been used before in previous work [98, 99, 100, 101, 102, 103] in which the constants are not presented as relevant physical parameters such as β_1 and β_2 in eq 7.6. Different methods [123, 124, 125, 126, 127, 128] can also be used to obtain the resonance frequency and the quality factor, however, the method used above was found to be the simplest and most reliable, with a typical fractional uncertainty of resonant frequency f_r and in line-width g about $2 \cdot 10^{-7}$ and $4 \cdot 10^{-4}$ respectively.

The values of f_r and g can be substituted in eq 7.5 to obtain the relative permittivity ε, but in order to use f_0 and g_0, calibration with a reference fluid is necessary to correct for the dilation of the dimensions of the cavity due to the

changes in T and p. The next section explains how f_0 and g_0 can be obtained from the cavity calibration.

7.4 Correction for dilation effects

The dimensions of the cavity are influenced by dilation due to the thermal expansion and the pressure of the fluid within the cavity; hence, a correction is required to account for the change in the spatial distribution of the electromagnetic field within the cavity between evacuated and filled conditions. These effects can be fully accounted for by measuring the resonant frequency of the cavity filled with a reference fluid over the range of operating temperatures and pressures. Thus, the expression for f_0 and g_0 becomes:

$$\begin{aligned} &f_0 = f_{00}(1-\alpha\theta)(1+\gamma p), \\ &\text{and} \\ &g_0 = g_{00}, \end{aligned} \tag{7.8}$$

where the terms $(1-\alpha\theta)$ and $(1+\gamma p)$ are correction factors for thermal expansion, and geometric dilation, and α is the volumetric coefficient of thermal expansion for stainless steel type 316 taken as $15.9\cdot10^{-6}$ K^{-1} [129], γ is a parameter signifying the elastic properties of the resonator, p the absolute pressure, f_{00} the vacuum resonance frequency at an arbitrary room temperature (289.95 K) and $\theta = (T/K - 289.95)$, obtained by forcing agreement between the relative permittivity calculated from literature and that obtained from

experimental data of calibration with methane. The methane used had a mass fraction purity quoted as 0.9999 with a mole fraction impurity of < 0.0001 ethane. The resonant frequencies were measured on an isotherm at a temperature of 50 °C, in order to use the data at the same temperature from Moldover and Buckley [130], at six pressures distributed equally from (3 to 9) MPa. The relative permittivity ε was calculated from the equation:

$$\frac{\varepsilon - 1}{\varepsilon + 2} = \rho\left(A_\varepsilon + B_\varepsilon \rho + C_\varepsilon \rho^2\right), \tag{7.9}$$

with dielectric virial coefficients A_ε = 6.5468 $cm^3 \cdot mol^{-1}$, B_ε = 7.33 $cm^6 \cdot mol^{-2}$, C_ε = -124 $cm^9 \cdot mol^{-3}$ taken from [130] at t = 50 °C, and densities taken from NIST REFPROP database [131] that uses the correlation of Setzmann and Wagner [132]. The parameters for eq 7.8, determined from least-squares fits, of the vacuum and methane data, are given in Table 7.1.

Table 7.1: Parameters for eq 7.8 determined by least-squares fits of vacuum and methane resonant frequencies

f_{00}/MHz	$10^6\,\gamma$/MPa^{-1}	g_{00}/MHz
344.553	104	0.585

Based on this calibration, the fractional uncertainty in the relative permittivity measurements was estimated as $\delta\varepsilon < 1 \cdot 10^{-4}$.

7.5 Correlation of density with relative permittivity

7.5.1 For the pure fluids:

Measurements of the relative permittivity of a fluid can be related to the density of non-polar fluids with the Clausius-Mossotti equation which relates the relative permittivity ε to the molar density ρ and the molar polarizability $\wp(p,T)$ as follows:

$$\wp(p,T) = \frac{\varepsilon - 1}{\varepsilon + 2}\frac{1}{\rho}, \tag{7.10}$$

and the expansion of the molar polarizability as a function of density is:

$$\wp(p,T) = A_\varepsilon(1 + b\rho + c\rho^2 + ...), \tag{7.11}$$

where A_ε, b, c are the first, second, and third dielectric virial coefficients respectively. The Clausius-Mossotti relation is useful for non-polar fluids, when the molar polarizability $\wp(p,T)$ has a slight dependency on density, temperature, and frequency. For example, for methane, $\wp(p,T)$ changed by only 0.7 % when the amount of substance density varied from (0.002 to 0.03) mol·cm^{-3} at temperatures between (100 to 300) K, and pressures p from (2 to 35) MPa [133].

The molar polarizability $\wp(p,T)$ has been measured by Schmidt and Moldover [134] for methane, and fit with a four-parameter expression [132]:

$$\wp_{CH_4}(p,T) = A_{\varepsilon,273}(1 + b\rho + c\rho^2) + A_\tau(\frac{T}{273.16\,K} - 1). \qquad (7.12)$$

For propane, the experimental data from [135] were represented by:

$$\wp_{C_3H_8}(p,T) = A_{\varepsilon,273\ K}(1 + b\rho) + \left(\frac{N_A \mu^2}{9\varepsilon_0 k_B T}\right). \qquad (7.13)$$

with two adjustable parameters $A_{\varepsilon,273\ K}$ and b.

Polar fluids, such as propane, $\wp(\rho,T)$ depends on density and temperature and the term $\left(\frac{N_A \mu^2}{9\varepsilon_0 k_B T}\right)$ represents the dipolar contribution to the polarizability. In eq 7.13, Avogadro's constant N_A = 6.0221367·10^{23} mol^{-1}, permanent dipole moment of propane μ = 2.82859·10^{-31} C·m {= 0.0848 D} from [136], permittivity of free space ε_0 = 8.8541878·10^{-12} J^{-1}·C^2·m^{-1}, Boltzmann's constant k_B = 1.380658·10^{-23} J·mol^{-1}·K^{-1}, and the parameters $A_{\varepsilon,273\ K}$, A_τ, b, and c are given in Table 7.2.

Table 7.2: Fitting parameters for eqs 7.12 and 7.13 determined for CH_4 from [132] and for C_3H_8 from [135]

	$A_{\varepsilon,273\ K}$	b	C	A_τ
	cm^3·mol^{-1}	cm^3·mol^{-1}	cm^6·mol^{-2}	cm^3·mol^{-1}
CH_4	6.54467	1.250	-44.7	0.00622
C_3H_8	15.8527	6.27		

7.5.2 For the mixture

Arranging eq 7.10, and taking the expression $\{(\varepsilon -1)/(\varepsilon + 2)\} = CM$ (for Clausius-Mossotti), the density for a mixture $\rho_{mix}(p,T)$ can be expressed as :

$$\rho_{\mathrm{mix}}(p,T) = \frac{CM}{\wp_{\mathrm{mix}}(p,T)}\,, \tag{7.14}$$

where $CM = \{(\varepsilon -1)/(\varepsilon + 2)\}$ is determined from measurements of the relative permittivity ε of the mixture, and $\wp_{\mathrm{mix}}(p,T)$ is the molar polarizability for the mixture.

Molar polarizability of liquid mixtures can be calculated with Oster's rule [137] as:

$$\wp_{\mathrm{mix}}(p,T) = \sum_{i=1}^{n} x_i \wp_{\mathrm{i}}(p,T)\,, \tag{7.15}$$

where x_{i} is the mole fraction of species i, and $\wp_{\mathrm{i}}(p,T)$ is the molar polarizability for pure component i at T and p and subscript mix refers to the mixture.

Assuming the same rule applies to gases, with zero volume change upon mixing, the molar polarizability of the mixture in this work $\{0.4026CH_4 + 0.5974C_3H_8\}$ can be calculated from:

$$\wp_{\mathrm{mix}}(p,T) = \left\{0.4026\,\wp_{\mathrm{CH_4}}(p,T) + 0.5974\,\wp_{\mathrm{C_3H_8}}(p,T)\right\}, \qquad (7.16)$$

with $\wp_{\mathrm{CH_4}}(p,T)$ and $\wp_{\mathrm{C_3H_8}}(p,T)$ are obtained from eqs 7.12 and 7.13.

A large volume change upon mixing can lead to significant errors. Thus, Harvey and Prausnitz [138] reported a mixing rule in which pure components are mixed isothermally at a constant temperature and a constant reduced density instead of a constant temperature and a constant pressure. This method can be used for either gases or liquids [139], and calculates the mixture relative permittivity as a function of temperature, composition and reduced density. Owing to the increasing demand for dielectric correlation for fluid mixture, the Harvey and Prausnitz rule [138] has been re-introduced in a recent paper by Harvey and Lemmon [140] with more details concerning the method of calculation.

The density of the mixture cannot be directly calculated from the Harvey and Prausnitz rule [138] because, while this method is mainly designed to calculate the dielectric relative permittivity, it requires the calculation of the dimensionless mixture reduced density $\rho_{\mathrm{r,mix}}$ which itself is calculated from the mixture molar density ρ_{mix} using:

$$\rho_{\mathrm{r,mix}} = \rho_{\mathrm{mix}} \sum_{i=1}^{n} \left(x_i \frac{1}{\rho_{\mathrm{c,i}}} \right), \qquad (7.17)$$

where $\rho_{c,i}$ is critical density for the component i.

An initial value for the density of the mixture can be used to accurately determine the density by minimizing the difference between the calculated and the measured relative permittivity using a least squares technique.

With the Harvey and Prausnitz rule [138], the expression CM is often replaced with KW for polar fluids, following the expression of Kirkwood and Onsager [141] given by:

$$KW = \frac{(\varepsilon - 1)(2\varepsilon + 1)}{9\varepsilon} \tag{7.18}$$

The difference between the two terms CM and KW only differ 'considerably' for $\varepsilon > 2$ [137]. In this work, the difference was $< 5 \cdot 10^{-3}$ where the maximum relative permittivity measured was $\varepsilon < 1.5$.

7.6 Calculation of liquid volume fraction

The liquid volume fraction was calculated in the 2-phase region (liquid + gas) from the relation with a normalised function $\epsilon = [\varepsilon - \varepsilon(g)]/[\varepsilon(l) - \varepsilon(g)]$ where ε is the measured relative permittivity for the mixture, $\varepsilon(g)$ is the relative permittivity of saturated gas, and $\varepsilon(l)$ is the relative permittivity of saturated liquid at the same temperature. The values of $\varepsilon(g)$ and $\varepsilon(l)$ can be determined

from the measurements or calculated from the Harvey and Prausnitz [138] or obtained from NIST REFPROP database [131] version 8.

The relationship between the function Є and the liquid volume fractions was determined at different liquid levels in the cavity resonator by calibration with a reference fluid. The details of the calibration and the results of ε(g) and ε(l) and the liquid volume fractions are discussed collectively in Chapter 9.

Chapter 8

EXPERIMENTAL DESIGN AND PROCEDURE

As shown in Figure 8.1, the overall experimental setup includes the microwave cavity resonator, a magnetically activated circulation pump, and a differential pressure gauge all of which are mounted within a circulated air thermostat and the temperature controlled to < ± 10 mK.

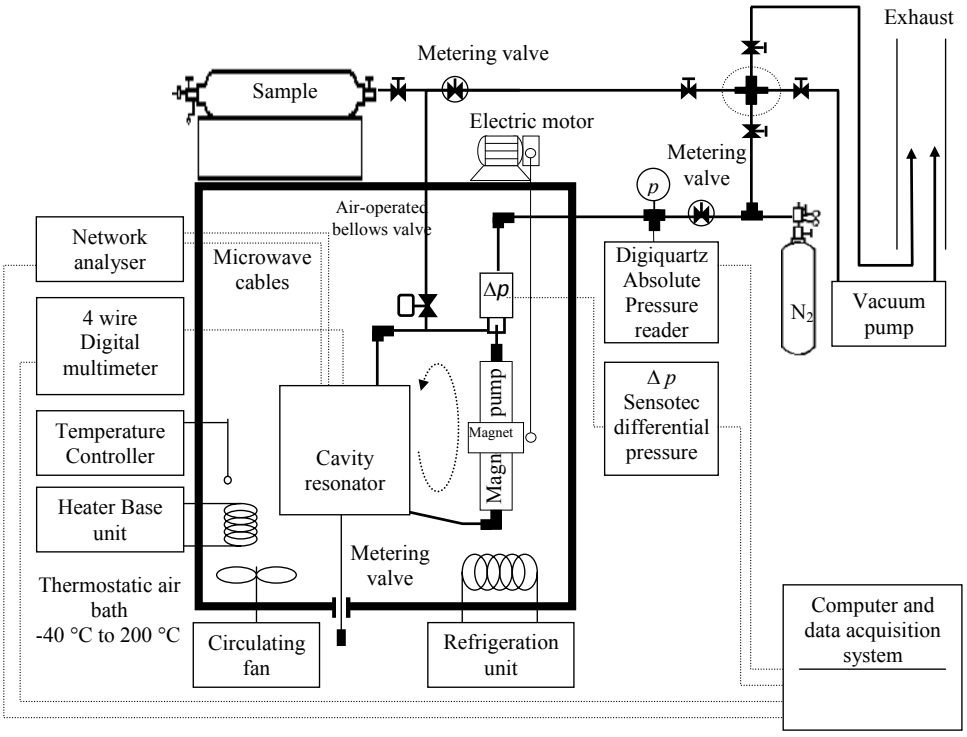

Figure 8.1: Schematic for the apparatus including microwave resonator, magnetically activated circulation pump, and differential pressure gauge all mounted within a circulated air-bath.

8.1 Cavity resonator assembly:

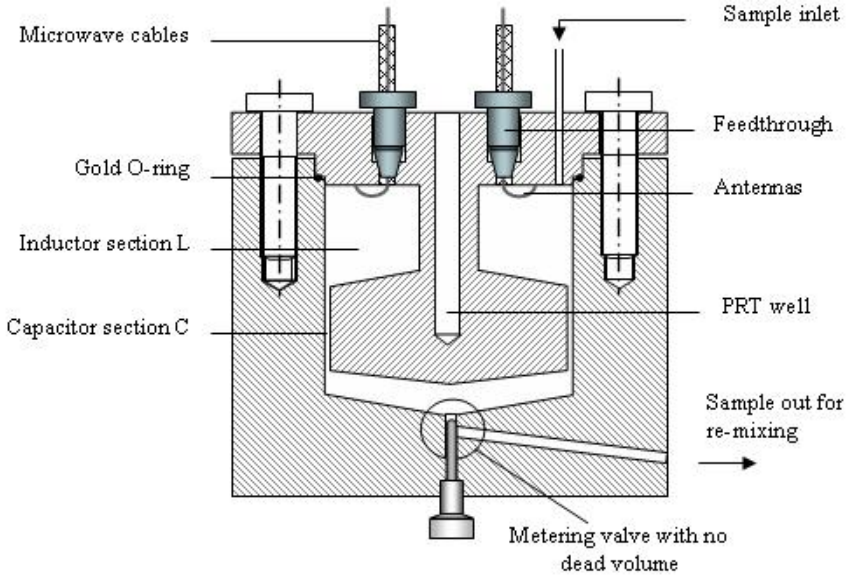

Figure 8.2: Cross-section through the microwave cavity resonator machined from type 316 stainless steel in two parts that were aligned at an interlocking step and sealed with an Au o-ring.

The cavity resonator, shown in Figure 8.2, was designed to be both the geometry required to form the *LC* resonator and to act as a pressure vessel capable of operating at temperatures up to 470 K and pressures below 20 MPa. The resonator, with the dimensions shown in Figure 8.3, was fabricated in two parts from a single cylindrical billet of {0.6585Fe + 0.0008C + 0.02Mn + 0.00045P + 0.0003S + 0.01Si + 0.17Cr + 0.12Ni + 0.02Mo}, commonly known as 316 austenitic stainless steel.

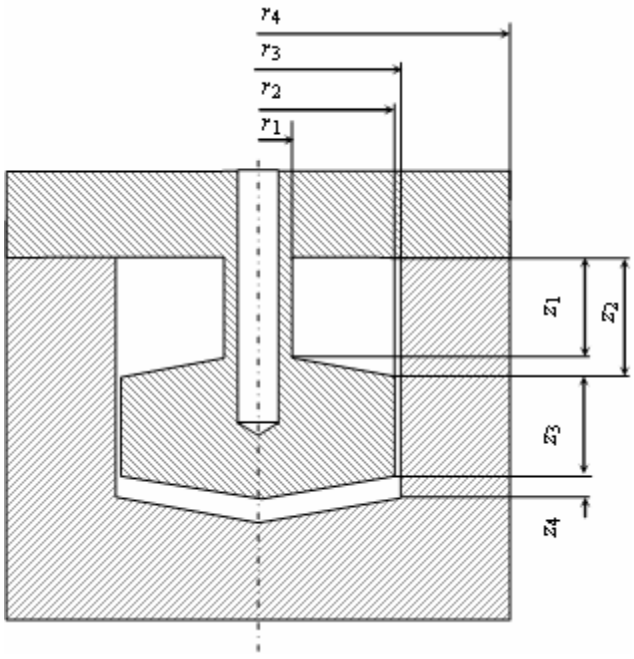

Figure 8.3: Schematic cross-section through the resonator with the dimensions r_1 = 6 mm, r_2 = 24 mm, r_3 = 25 mm, r_4 = 45 mm, z_1 = 20 mm, z_2 = 23.5 mm, z_3 = 20 mm, and z_4 = 5 mm.

The lower part, shown in Figure 8.3, formed a hollow canister with an inner diameter of 50 mm and wall thickness of 20 mm at least 48.5 mm deep. The upper part, with dimensions provided in Figure 8.3, served as a lid with a bulbous coaxial extension into the cavity supported from the lid by an extension of diameter 12 mm and length 20 mm. The bulbous portion had a diameter of 48 mm and a length of 20 mm. When assembled, the resonator had an internal volume of about 60 cm^3 and an annular gap ($r_3 - r_2$) of about 1 mm separated the bulbous extension and the inner surface of the canister. As shown in Figure 8.2, the toroidal section of the cavity acted as an inductance L and the

gap between the canister and bulbous portion acted as a capacitor *C*. All internal surfaces exposed to fluid were machined and polished to a mirror surface finish so that the surface defects were < 1 μm; an average surface roughness of 0.25 μm was achieved. The two parts were bolted together with eight stainless steel bolts 6 mm diameter by 40 mm long. The bolts were designed to be as close as possible to the sealing surface and on the smallest practical bolt circle. This improved both the reliability and pressure rating of the seal. Details of the design rules and equations for the cavity resonator, as a pressure vessel, are included in ref [142], and for the bolted joints in ref [143].

The lower surfaces of both the canister and bulbous portion were angled to enhance drainage when orientated in a gravitational field; the surfaces also acted as a parallel plate capacitor that served in the determination of the liquid volume fractions. Sample entered the cavity through the lid and, when the metering valve was open, exited through the base. When the metering valve was closed, the valve stem was flush with the inner surface. A platinum resistance thermometer (PRT) was placed inside the bulbous portion so that the sensing element was within the centre of the toroidal inductor.

8.1.1 Sealing element:

The lid was machined with an interlocking step, shown in Figure 8.2, about 2 mm across and 5 mm deep, and the step served to ensure concentric alignment

at the surface where the two parts contacted. The cavity was sealed, at the interlocking step, with a gold o-ring with a cross-sectional diameter of 1 mm.

8.1.2 Needle valve

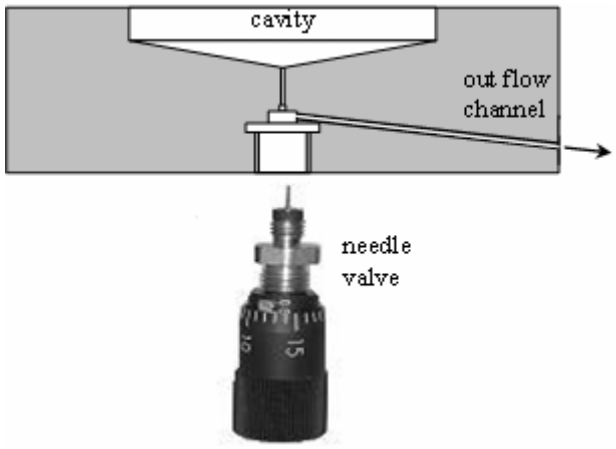

Figure 8.4: A sketch for the needle valve used to seal the outlet port of the cavity using a vernier handle to ensure a reproducible needle position after re-mixing.

To ensure that the fluid phase transition only occurred within the *LC* cavity, a needle valve was used to seal the cavity outlet such that the valve stem tip was almost flush with the internal surface so as to minimize dead volume. This needle valve was equipped with a vernier handle, as shown in Figure 8.4, to ensure a reproducible needle position after mixing.

8.1.3 Sample inlet valve:

The upper cavity inlet was sealed with a three-port air-operated bellows valve Nupro™ HB-series which can withstand 24 MPa and 477 K, and was equipped with VCR® face metal seal fittings.

8.1.4 Coupling loops:

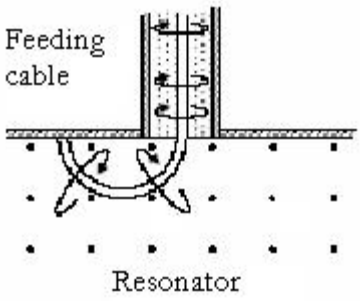

Figure 8.5: A sketch showing the coaxial cable central conductor passing through the lid as an inductive coupling loop connected to the resonator wall forming an electrical short, while the outer conductor is electrically connected to the vessel wall.

The electromagnetic energy is magnetically coupled into and out of the cavity by two coupling loops (antennae) located in the inductor section. The outer conductor of the microwave co-axial cable was attached to the outer surface of the cavity while the central conductor passed through the lid. The feedthrough within the lid was formed from a Swagelok™ compression fitting that fit the

outer diameter of the 50 Ω stainless steel PTFE insulated semi-rigid microwave cable Micro-coax™, part number UT-85-SS.

This scheme, shown in Figure 8.5, allowed the 0.51 mm diameter central conductor of the cable to be fed through the lid and be bent into a semicircular loop, of diameter about 5 mm, with its end connected to the inner surface of the lid. Contact was made by spot welding using a capacitor electrical discharge. This method proved more reliable and simpler than earlier designs that used glass-to-metal seal assemblies, eliminating the need for the difficult lid re-surfacing process usually required to remove the carbon-rich layer created during the glass melting process, which significantly decreases the corrosion resistance of the stainless steel and increases the resistance of the skin layer of the cavity lid.

The loop was orientated so that it was at an angle $< \pi/2$ with respect to the magnetic lines thus reducing the coupling, which can otherwise contribute to the resonance line width, without significant reduction in the signal-to-noise ratio. This antennae setup, located at an azimuth angle π apart, survived a pressure test of 60 MPa. The mechanical geometry and arrangement of the fluid inlet port was identical with that used for the antenna so that the antennae could be placed in different locations and thus allowing a future study of the effect of coupling.

8.2 Vector network analyser

A microwave vector network analyser (Agilent™, model 8753ES) was used to excite the resonator through one antenna and the complex forward scattering transmission fraction $\boldsymbol{S}_{21}$ was measured using the second antenna. The vector network analyzer, or VNA, is an instrument which measures the complex transmission and reflection characteristics of two-port devices in the frequency domain. It does this by sampling the incident signal, separating the transmitted and reflected waves, and then performing ratios that are directly related to the reflection and transmission coefficients of the two-port. The frequency is swept to rapidly obtain amplitude and phase information over the band of frequencies of interest. The S-parameter representation is the most common format used to represent VNA measurements; $\boldsymbol{S}_{11}$ and $\boldsymbol{S}_{21}$ are the input reflection coefficient and forward transfer coefficient (gain or loss) respectively, and, $\boldsymbol{S}_{22}$ and $\boldsymbol{S}_{12}$, are the output reflection coefficient and reverse transfer coefficient (gain or loss) respectively. Calibration of the VNA is necessary, as will be discussed, to correct for cable losses and to establish a phase reference plane. The signal was passed to and from the resonator within two Sucoflex™ flexible microwave cables, manufactured by Huber and Suhner AG, Switzerland. Each cable was fitted with a 7 mm connector at one end and an N-type at the other; this arrangement eliminated the need for additional adaptors. Prior to the start of each measurement, the network analyser and cables were calibrated over the frequency range of the

measurements in order to eliminate uncertainties arising from reflections and attenuation in both the cables and the connectors. The calibration was performed using a calibration kit model HP85032 that contains a precision 50 Ω load, a short circuit, and an open circuit. The resonance frequency f_r of the lowest order non-degenerate *LC* mode was determined from measurements at 201 frequencies spanning $f_r \pm 2g$, where g is half the resonance line-width at 0.707 times the maximum amplitude. At each frequency, the network analyser averaged the signal determined in 50 measurements prior to the calculation of the transmission coefficient $\boldsymbol{S}_{21}$ to obtain the resonance frequency f_r and line-width g.

8.3 Circulation pump:

The circulation pump, shown in Figure 8.1, was used to re-mix the mixture into one phase when a new phase was introduced after reaching the dew point. The pump draws the fluid from the bottom of the cavity and pushes it through the differential pressure gauge to the inlet within the top of the cavity. The design of this circulating gas pump was based on those used for similar purpose and reported in [144,145,146,147,148]. The circulating pump, shown in Figure 8.6, was formed from a cylinder and piston and was capable of operating at a pressure up to 40 MPa. The cylinder was machined from non-magnetic 316 stainless steel to have an outer diameter of 14.5 mm and an inner diameter of 9 mm with a smooth internal surface, while the piston was formed

from {0.8478Fe + 0.0015C + 0.01Mn + 0.0004P + 0.0003S + 0.01Si + 0.13Cr} commonly known as type 420 martensitic stainless steel.

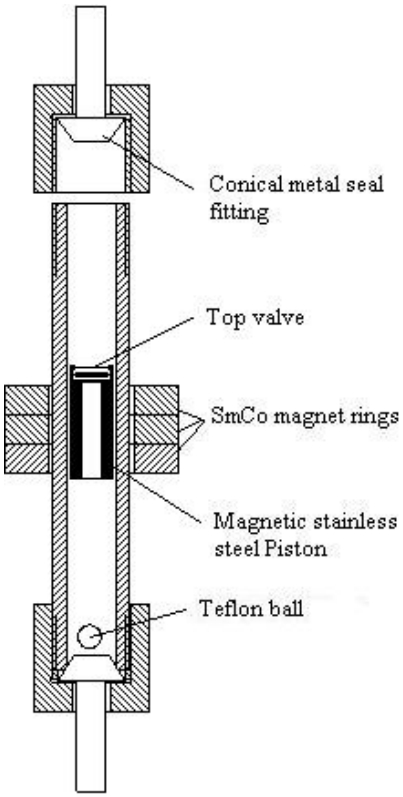

Figure 8.6: Schematic cross section through the magnetically activated circulation pump used to re-mix the fluid. The pump is formed from a cylinder with a piston fitted with a check-valve to promote flow in the upward direction. The piston was fabricated from 420 series magnetic stainless steel and forced to move by a samarium-cobalt ring-magnet mounted outside the cylinder that was fabricated from type 316 stainless steel.

A check valve was formed atop the piston from a thin sheet of stainless steel type 316 and secured in place with a pin. A ball of PTFE was placed at the bottom of the piston to act as a non-return valve. The piston was moved up and down by means of a samarium-cobalt three-ring magnet of internal diameter 15 mm attached to a variable speed electric motor placed atop but outside the thermostat. The magnet material could withstand temperatures up to 473 K without significant loss of field strength. The optimal volume flow-rate was about 30 $cm^3 \cdot min^{-1}$.

8.4 Temperature measurement

The temperature was measured with a Class A platinum resistance thermometer (PRT) with a nominal resistance of 50 Ω which provided less self-heating than a 25 Ω PRT and a better resolution than a 100 Ω PRT. This thermometer was calibrated against a standard 25 Ω platinum resistance thermometer (SPRT), which had been calibrated on ITS-90 by the Measurement Standards Laboratory of New Zealand. The triple point of the SPRT was updated by measuring its resistance in the triple point cell as shown in Figure 4.7. The uncertainty in the temperature measurements was determined as $< \pm 0.01$ K. The PRT was located in a blind hole drilled within the bulbous portion of the lid so that the sensing element was within the centre of the toroidal inductor. The dc resistance of the PRT was determined with a 4-

wire ohm measurement (Agilent 34401A). More details on the thermometer calibration parameters are included in the appendix.

8.5 Pressure Measurements

A differential pressure gauge (DPT) was used to measure the difference between the fluid pressure within the cavity and the pressure of a reference nitrogen line, as shown in Figure 8.1. The DPT used (Sensotec™ model HL-Z/6917-02ZD-03) had a full scale differential pressure 0.3 MPa, resolution 0.1 kPa, and an uncertainty ± (0.0025*p*/MPa + 0.00075). A voltage source of 10 V dc was used for excitation, and an amplifier unit was used to amplify the output from about 2 mV to about 2 V. This DPT was a high line wet/wet type (gas or liquid) that could be used to a maximum line pressure of 17 MPa. The DPT was located within the thermostat and placed directly on the top of the magnetic pump in order to flush any dead volume could be created within its internal space.

The pressure of the reference nitrogen line was measured with a Digiquartz™ Intelligent Transmitter having a resonating quartz pressure transducer Paroscientific™ model 1000-2K and a digital interface board equipped with a microprocessor-controlled counter and RS-232 serial communication port. The pressure transducer has an absolute pressure range (0 to 13.8) MPa, and an uncertainty ± 0.0014 MPa. This pressure transducer provided two continuous

frequency output signals: one corresponding to the pressure and the other one to its internal temperature. The digital board uses these two signals to temperature-compensate the pressure measurements. The pressure calibration was performed using a liquid lubricated piston/cylinder (LLPC) dead-weight pressure gauge Desgranges et Huot Instruments, model DH-21000, with an uncertainty ± (0.0001p/MPa + 0.0005). The pressure was calibrated in the range (0.1 to 9) MPa, at temperature range (298 to 350) K to compensate for the temperature effects on the DPT, and also to offset and adjust the span of the nitrogen line pressure transmitter. Results of this calibration gave an uncertainty ± 0.001 MPa. Calibration parameters were obtained from linear regression with a least square method; details are included in the appendix. At the commencement of each isochore, the nitrogen line pressure was adjusted to be at the same pressure as that in the cavity so that the DPT output was null. At each step along the isochore, the pressure was calculated by adding the DPT reading to the nitrogen line pressure.

8.6 Fluid sample

The $\{(1 - x)CH_4 + xC_3H_8\}$ was prepared gravimetrically from methane and propane supplied by BOC™ Gases, New Zealand, Limited. The supplier stated the propane minimum mass fraction purity was 0.9985 with mass fraction impurities of 0.0009 for ethane, 0.00057 for 2-methylpropane, 0.00003 for butane, and 0.00001 for propylene while for methane the mass

fraction purity was quoted as 0.9999 with a mole fraction impurity of < 0.0001 ethane. A standard Peng-Robinson equation of state was used to estimate the phase diagram of $\{(1 - x)CH_4 + xC_3H_8\}$ at $x \approx 0.6$ as well as the mass of the components required to fill the total apparatus volume of 88 cm^3.

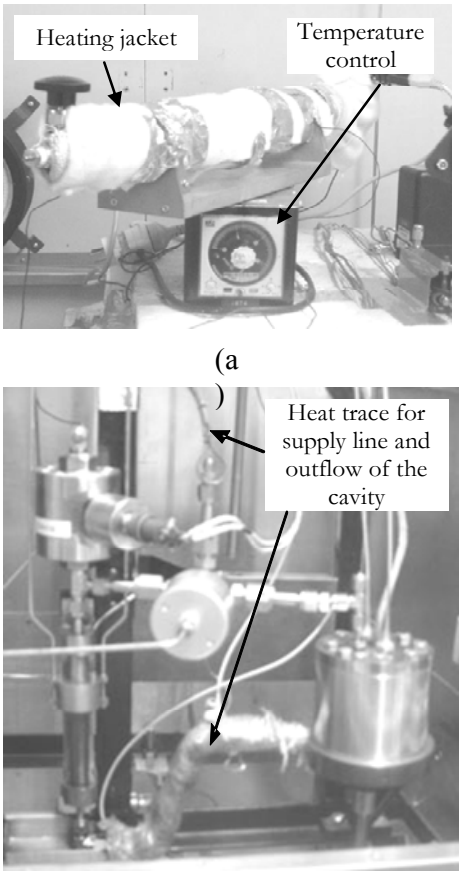

Figure 8.7: A photo showing: a) storage vessel kept in a controlled heating jacket; and b) interconnecting tubing were trace heated to $T > 373$ K.

The mixture was prepared from fluids transferred by mass into a stainless steel cylinder, Whitey™ model Dot-3A 5000, of internal volume 500 cm^3. An

electronic top-loading pan-balance Mettler Toledo™ model PE11, with a maximum operating mass of 11 kg and an uncertainty of ± 0.1 g, was used to give x = 0.5974 with an uncertainty calculated as ± 0.0013. Stainless steel spheres were placed within the sample preparation cylinder, which when shaken acted as mechanically agitators to achieve the compositional homogeneity. Also, in order to eliminate phase separation during the mixture preparation, both the storage vessel and interconnecting tubing were trace heated to T > 373 K as shown in Figure 8.7.

8.7 Data acquisition and measurement procedure:

A computer equipped with a general purpose interface board GPIB was connected to the network analyser, the Agilent 34401A multimeter used for measuring the 4-wire resistance of the PRT, and the Agilent 34401A multimeter used for measuring the voltage output of the Sensotec differential pressure transducer. The Paroscientific pressure gauges were connected to the two serial ports of the computer. The control software has been developed in Agilent Vee™ platform. Data arrays were saved in files then analysed and solved using MathCAD™ software.

To obtain a phase boundary, the following procedure was adopted: (1), the apparatus was baked at T > 373 K under vacuum; (2), the homogeneous sample was expanded from the valve atop the heat bath, in the resonator,

through tubing trace-heated to $T > 373$ K; (3), when the desired upper pressure was attained in the resonator, any condensed fluid resulting from expansion cooling, was re-combined to a compositionally homogeneous single phase with the aid of the circulation pump; (4), the apparatus was cooled to $T \approx 5$ K higher than the expected dew temperature and then the temperature was decreased in steps of about 0.25 K and allowed to equilibrate for about 5 h to attain thermal and hydrostatic equilibrium as indicated by measurements of T, p, and f_r that were fractionally consistent within their respective precision for more than 3 consecutive measurements; (5), the temperature, pressure and resonance frequency were measured and (6), steps (4) and (5) were repeated until the phase boundary was determined.

During circulation, the fluid exiting the resonator was heated to a temperature of about 393 K by trace heating elements that were attached to the outer surface of the tube between the resonator and pump. The circulation pump was operated for a total of 2.5 h in 0.25 h increments. The mixture was left overnight before reducing the pressure. When the sample was homogeneous, as indicated by measurements of T, p, and f_r, a small quantity of fluid was expanded out of the apparatus and measurements along the lower density isochore commenced.

Density and liquid volume fractions were calculated from the relative permittivity which was determined, with an uncertainty of $\delta\varepsilon = 1 \cdot 10^{-4}$, from the

measurements of the resonant frequency. The resolution and accuracy with which temperature, pressure and frequency were measured far exceeded the uncertainty in the mole fraction of the mixtures ($\delta x = 13 \cdot 10^{-4}$), which dominated the error in the determined (p,T) phase boundary as will be discussed in the results.

Chapter 9

RESULTS AND DISCUSSION

9.1 Dew points results:

9.1.1 Determination of dew points from resonance frequencies:

As stated before, the measurement of the relative permittivity is not necessary for determining the dew points, where the measurements of the resonance frequencies suffice. At each temperature, the resonance frequency, temperature, and pressure were measured. It was anticipated when dew forms in the cavity, liquid will collect at the base of the bulbous portion and, at the same time, the average density of the remaining sample, including that in the concentric cylinder, decreases and, because of the relationship between ε and ρ, results in a decrease in the capacitance with a resulting increase in the resonance frequency. These expectations were observed experimentally and are shown in the top of Figure 9.1 for the isochore with dew temperature, determined from our measurements, of T^{d} = (333.83 ± 0.23) K, listed in Table 9.1, and indicated with the vertical dashed line. In the single gas phase region, shown at temperatures to the right of the vertical dashed line in the bottom of Figure 9.1, df(gas)/dT lies between (-0.020 and 0.008) MHz·K^{-1} and is almost a linear function of temperature.

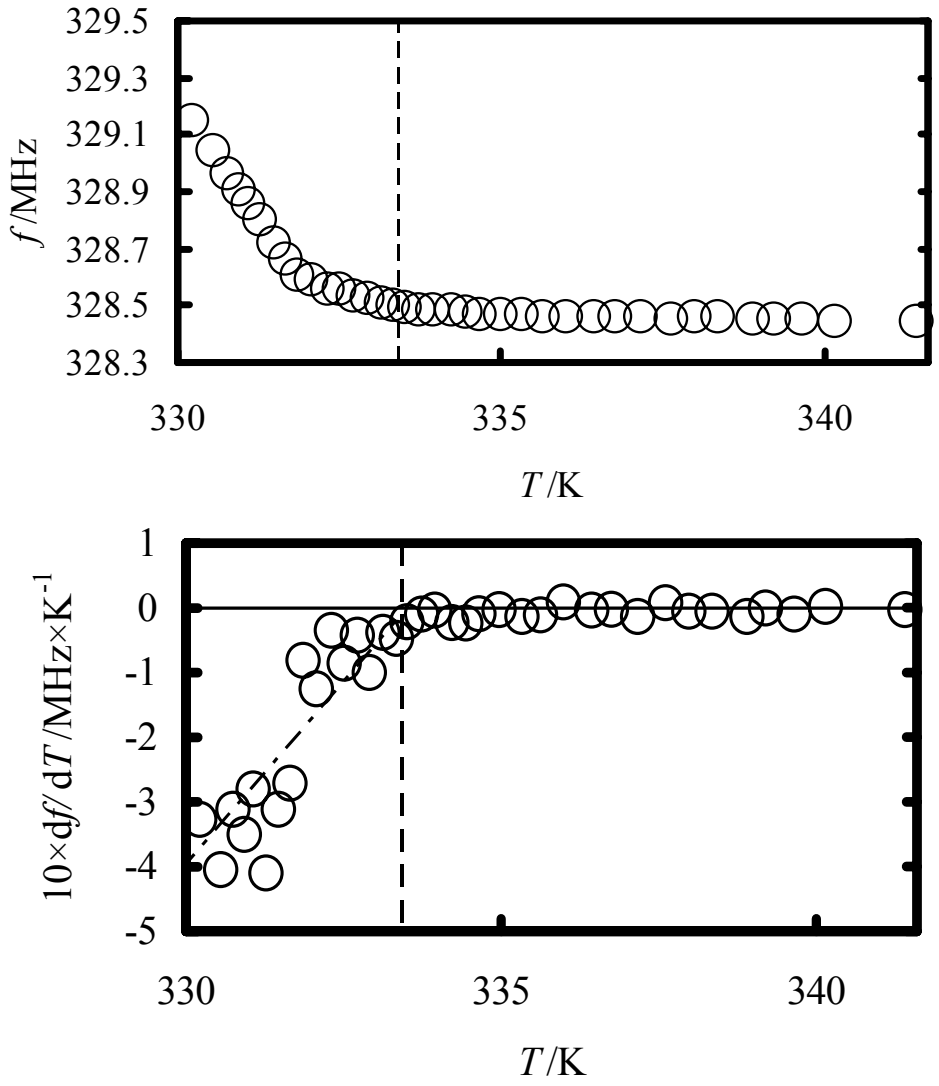

Figure 9.1: TOP: Frequency f as a function of temperature T obtained for the isochore with a dew temperature, determined from these measurements, of $T^{d} = (333.83 \pm 0.23)$ K. BOTTOM: The derivative df/dT as a function of temperature T for the measurements shown atop where the line —– –—, shown to the left of the vertical dashed line, illustrates the linear fit to the measurements obtained in the two phase region. The vertical dashed line in both figures indicates the dew temperature of $T^{d} = (333.83 \pm 0.23)$ K.

In the presence of both liquid and gaseous phases, at temperature to the left of the vertical dashed line, df(gas+liquid)/dT decreases from -(0.040 to 0.4) MHz·K^{-1} with decreasing temperature. At the dew point a distinct discontinuity in df/dT, shown in the bottom of Figure 9.1, was observed.

9.1.2 Resolution and uncertainty of measurements:

Because df/dT was nearly linear on either side of the discontinuity the dew temperature could be determined, within a fraction of the 0.25 K temperature step, from the intersection of two linear fits, shown in Figure 9.1 by the dash-dot-dash line for df(gas+liquid)/dT to the left of the vertical dashed line and df(gas)/dT ≈ 0. The uncertainty in the dew temperature was estimated to be ≈ 0.06 K, which is 0.25 times the 0.25 K step size. The corresponding uncertainty in the phase boundary pressure was also assumed to be 0.25 times dp/dT with dT = 0.25 K and this contributed < 0.005 MPa to the estimated uncertainty in the dew pressure.

The uncertainties, listed in Table 9.1, for the measured gas to liquid phase boundary (p, T) of {0.4026CH_4 + 0.5974C_3H_8} are at a confidence of 0.995 (k = 2), for the phase boundary temperature and pressure were obtained by combining in quadrature uncertainties arising from the determination of the phase boundary location (that is 0.25 times the step size) with uncertainties

arising from dT/dx, dp/dx, dp^d/dT, and the individual measurements of temperature, pressure and frequency.

Table 9.1: Experimentally determined dew pressure p^d at temperature T^d for $\{0.4026CH_4 + 0.5974C_3H_8\}$ with expanded uncertainties ($k = 2$).

T/K	p/MPa
340.38 ± 0.27	6.826 ± 0.036
337.06 ± 0.23	5.573 ± 0.027
335.69 ± 0.24	5.268 ± 0.028
333.83 ± 0.23	4.892 ± 0.026
331.38 ± 0.23	4.521 ± 0.026
329.11 ± 0.24	4.214 ± 0.028
325.99 ± 0.25	3.856 ± 0.030
324.16 ± 0.24	3.642 ± 0.028
320.95 ± 0.24	3.332 ± 0.029
315.53 ± 0.23	2.871 ± 0.026

The contribution to the uncertainty arising from the uncertainty in composition was estimated from the phase boundary measurements reported by Reamer et al. [112] that give $dT/dx \approx -81$ K while $dp/dx \approx 8.4$ MPa. For the mole fraction uncertainty $\delta x = 0.0013$, the former gives $\delta T \approx 0.1$ K (≈ 0.2 K at $k = 2$) while the latter gives $\delta p \approx 0.01$ MPa (≈ 0.022 MPa at $k = 2$) to the uncertainties listed in Table 9.1. Clearly, the $\delta x = 0.0013$ is the major source of uncertainty in this experiment. The next most significant contribution to δp arises from dp^d/dT, the slope of the dew-curve, which was estimated from a preliminary analysis

of our results. At T = 330 K our results gave $dp^d/dT \approx 0.15$ MPa·K^{-1} and this resulted in an additional contribution to the uncertainty δp between (0.0065 and 0.012) MPa {for k = 2 (0.013 and 0.024) MPa} that was also included in the uncertainty listed in Table 9.1; at $T \approx 320$ K and $x \approx 0.4$ the results reported in [112] gave $dp^d/dT \approx 0.10$ MPa·K^{-1} while at $T \approx 339$ K it was estimated from an equation of state $dp^d/dT \approx 0.30$ MPa·K^{-1}.

9.1.3 Comparison with EOS:

The dew pressures were estimated for {0.4026CH_4 + 0.5974C_3H_8}, with a molar mass M = 0.032802 kg·mol^{-1}, from a combination of the composition and temperature with 3 equations of state: (1), National Institute of Standards and Technology, Standard Reference Database 14 (NIST 14) version 4 [149]; (2), the Peng-Robinson PR cubic equation of state; and (3), the Soave–Redlich–Kwong SRK cubic equation of state. For both (2) and (3) the predictions were obtained from two equation of state packages: the Separation and Phase Equilibrium Calculations program SPECS, developed at the Centre for Phase Equilibria and Separation Processes in the Department of Chemical Engineering at the Danish Technical University (www.ivc-sep.kt.dtu.dk) and a commercially available program HYSYS marketed by Hyprotech, recently, acquired by Aspen Technology (www.aspentech.com).

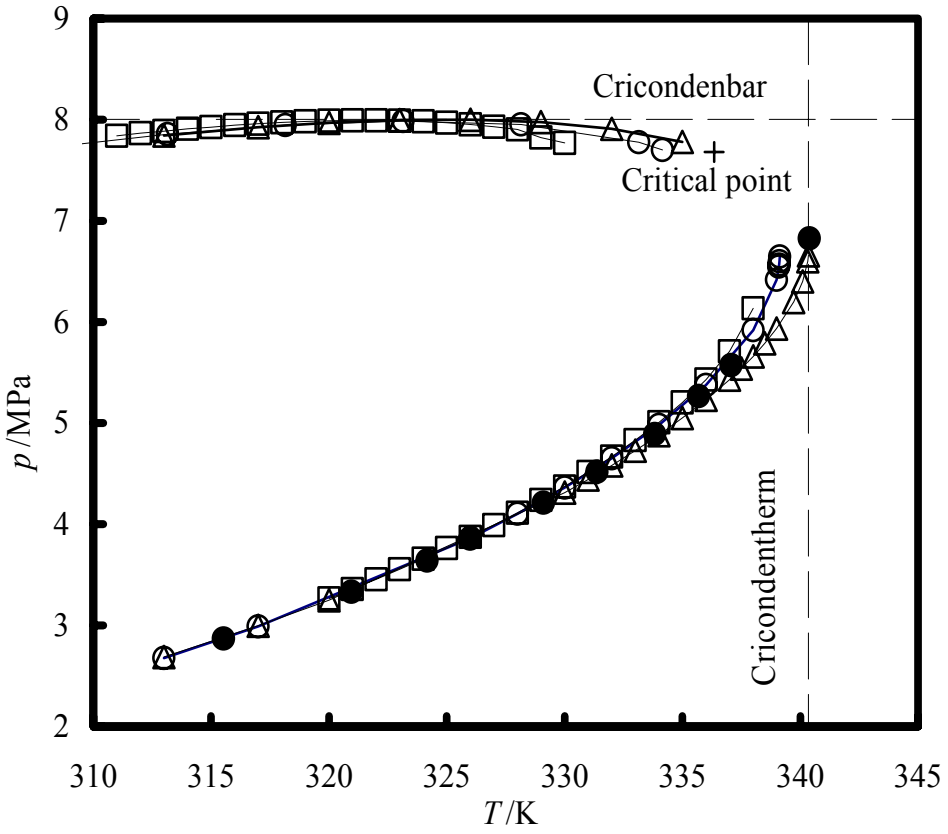

Figure 9.2: Phase envelope for $\{0.4026CH_4 + 0.5974C_3H_8\}$, pressure as a function of temperature T calculated with: ○, Peng-Robinson as implemented in HYSYS; □, REFPROP [131]; △, Soave-Redlich- Kwong equation of state as implemented in HYSYS; vertical dashed line, the cricondentherm at 340.35 K; horizontal dashed line, the cricondenbar at 8.002 MPa; +, critical point; ●, this work.

To estimate the thermodynamic properties of mixtures, NIST 14 uses a Helmholtz function for each pure component and a generalized mixture function with three parameters adjusted to represent the properties of a particular binary mixture [150]. For methane the equation of state reported by

Setzmann and Wagner [132] was used while for propane the model of the thermodynamic properties reported by Miyamoto and Watanabe [151] was used. Unfortunately, NIST 14 failed to converge and, therefore, provide a dew pressure at $T \geq 339$ K. The dew pressures estimated from the computer packages SPECS and HYSYS for both the PR and RKS equations of state differed only in the values of the binary interaction parameter: for HYSYS $k_{ij} = 0.012$ while within SPECS $k_{ij} = 0$. The dew pressure calculations performed with SPECS failed to provide a dew pressure at $T > 339.2$ K for both PR and SRK, while for HYSYS the highest temperature at which a dew-point could be determined with PR was 339.32 K and for SRK 340.35 K, which is just 0.03 K below our highest temperature, and according to HYSYS, SRK this value is the cricondentherm; HYSYS PR gave an estimated cricondentherm of 339.32 K. The dew pressure estimated from HYSYS with SRK at $T = 340.35$ K was 6.69 MPa as shown in Figure 9.2. This estimate is lower than the value listed in Table 9.1, at $T = 340.38$ K, by 0.14 MPa (about 2 %) and about a factor of 4 greater than the estimated expanded uncertainty in our measurement; this difference is greater, by about a factor of 14, than can be accounted for with $\delta T = 0.03$ K and $\mathrm{d}p^{\mathrm{d}}/\mathrm{d}T \approx 0.3$ MPa·K^{-1}. The cricondentherm shown as a vertical dashed line in Figure 9.2 is 340.35 K and the cricondenbar shown as horizontal dashed line is 8.002 MPa while the symbol (+) represents the critical point.

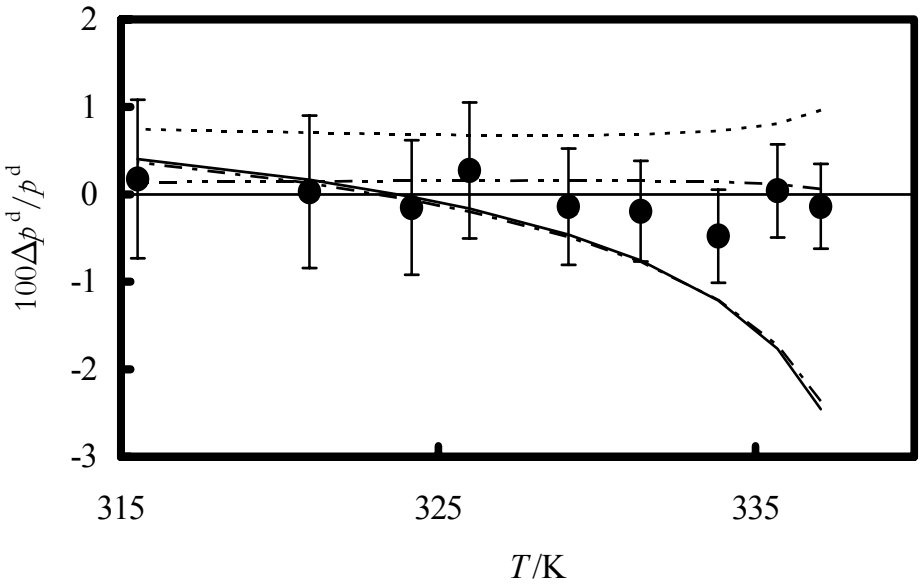

Figure 9.3: Fractional deviations $\Delta p^d/\ p^d = \{p^d(\text{expt.}) - p^d(\text{calc.})\}/p^d$ of the experimentally determined dew pressure p^d from that calculated with the Peng-Robinson equation of state with $k_{ij} = 0$ as implemented within the software package SPECS V5.0 at $T < 338$ K. None of the equations of state were able to estimate a dew pressure at $T^d = 340.38$ K and so no comparison could be made with the measurement at that temperature. ●, This work, where the error bars illustrate the expanded uncertainties ($k = 2$) listed in Table 9.1 for pressure while those for temperature are about the symbol size; - - - , NIST Standard Reference Data 14; ——–——, Peng-Robinson equation of state with binary interaction parameter $k_{ij} = 0.012$ as implemented within the software package HYSYS; ——–——, Soave-Redlich-Kwong equation of state with $k_{ij} = 0$ as implemented within the software package SPECS V5.; and ——, Soave-Redlich-Kwong equation of state with binary interaction parameter $k_{ij} = 0.012$ as implemented within the software package HYSYS.

The remaining 9 points of p^d listed in Table 9.1, at temperatures in the range (315 and 337) K, are shown in Figure 9.3 as relative deviations from, arbitrarily, the p^d estimated with PR SPECS, SRK SPECS, PR HYSYS, SRK HYSYS, and with NIST 14. The PR HYSYS estimates, shown in Figure 9.3, all lie within the estimated expanded uncertainty of our measurements. The p^d predicted by NIST 14 differ from PR SPECS by between (0.67 and 0.96) % while both SRK estimates lie 0.4 % above at T = 315 K and these differences diverge from PR SPECS and these results to be -2.5 % at T = 337 K. This difference is about a factor of 5 greater than the estimated expanded uncertainty of these measurements.

9.1.4 Comparison with previous experimental data:

There are eight known publications [104, 110 - 116] that report the dew pressure of $\{(1 - x)CH_4 + xC_3H_8\}$ as a function of $(1 - x)$ at temperatures in the range (273 to 363) K and all are shown in Figure 6.2, along with those values listed in Table 9.1. The results reported by May et al. [104] with a version of the re-entrant cavity optimised to determine ratio of the gas-to-liquid volume within the two-phase region, and those of May et al. [110], from measurements with a dual-sinker densimeter, are both for $(1 - x) > 0.75$ and cannot be compared directly with our results. Similarly, the majority of the results obtained by (p, V, T, x) methods [111 - 116] differ considerably from our mole fraction and hence cannot be compared directly with our results. However,

linear interpolation of $p^d(x, T)$ results reported in [112] to our $T(p, x)$ gave a difference less than 0.02 MPa at T = 329.11 K, 331.38 K, and 333.83 K, all well within the uncertainty cited in Table 9.1. This agreement is quite remarkable as shown in Figure 9.4.

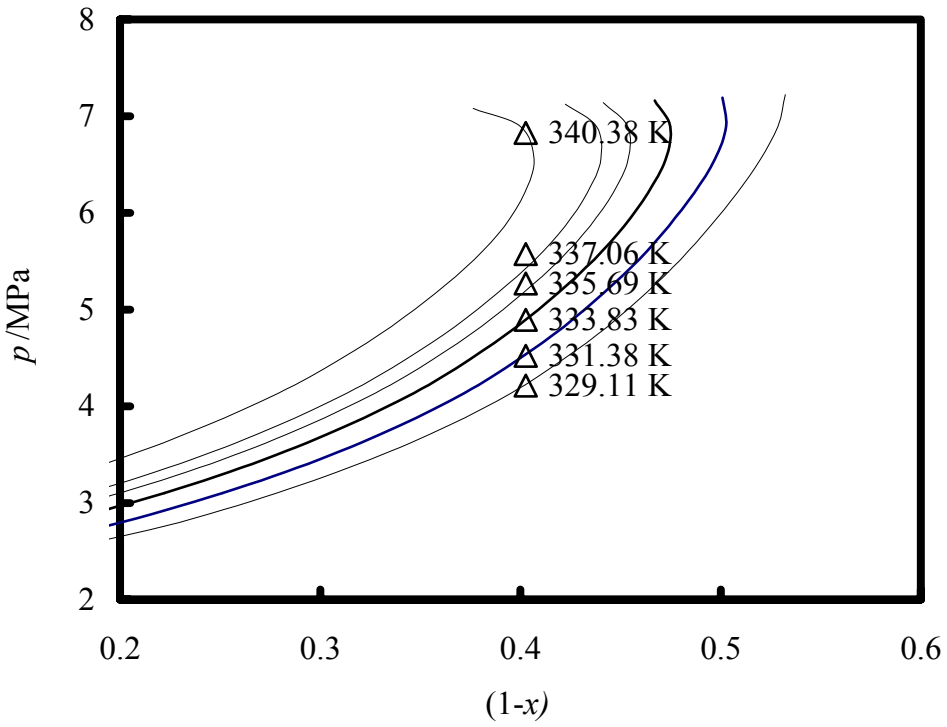

Figure 9.4: Lines of dew pressures interpolated from Reamer et al. [112] for $\{(1 - x)CH_4 + xC_3H_8\}$ as function of (1-x); △, experimental dew points at (1-x) = 0.4026 showing a remarkable agreement at lower temperatures, while the deviation increases as the temperature increases.

The difference increases as the temperature increases from 335.69 K to 340.38 K where interpolation gave a dew-pressure 0.58 MPa below our result (≈ 10 %) which is about 15 times the uncertainty given in Table 9.1. This is perhaps

not a surprising result because the p^d values reported in [112] were detected from discontinuities in the slope of isochoric (p,T) data that vanish at the cricondentherm and are small in the vicinity of it and near to criticality. Our results depend on discontinuities in the gradient of isochoric (ρ, T), which are increasingly easy to detect in the region of phase space near the cricondentherm as shown in Figure 9.2.

9.2 Density results:

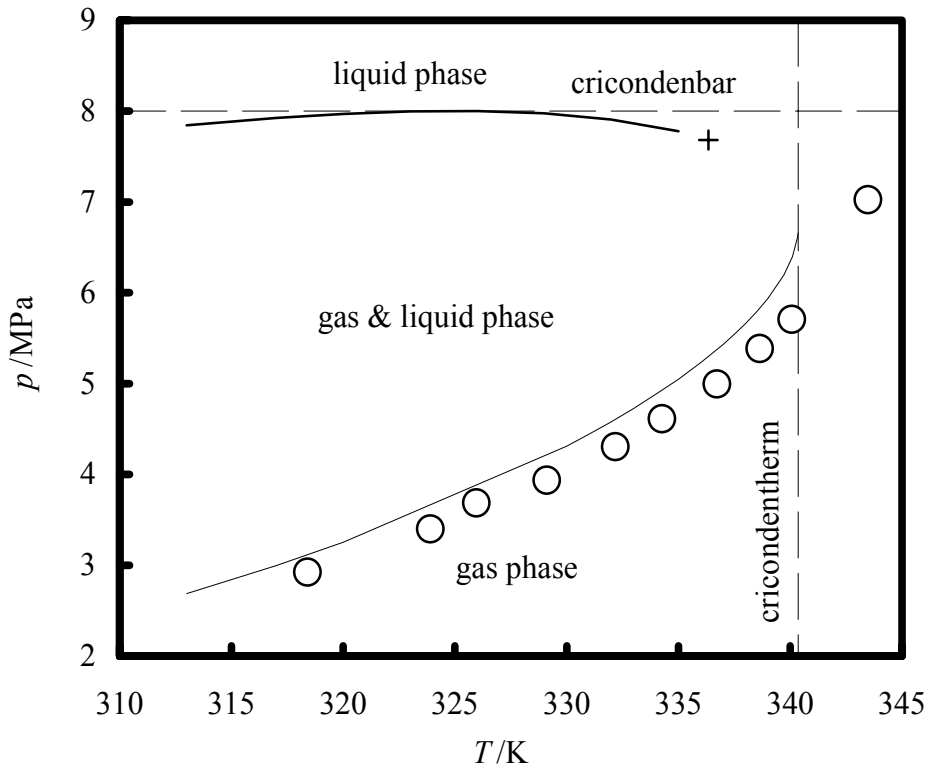

Figure 9.5: Graph showing the points at which the density was measured in the single phase (gas) region shown as circles (○); +, critical point.

There are ten points at which the density was calculated, as shown in Figure 9.5. The points were selected on each isochore about 3 K above the dew point. The experimental density, included in Table 9.2, was inferred, as discussed in Section 7.5, by two methods: 1) based on the Oster mixing rule [137], with polarizability calculations for pure CH_4 and C_3H_8 reported by Schmidt and Moldover [134]; 2) from the relative permittivity correlation reported by Harvey and Prausnitz [138]. Densities for pure CH_4 and C_3H_8 were determined with REFPROP [131], based on the equation of state reported by Setzmann and Wagner [132] for CH_4, and the correlation reported by Miyamoto and Watanabe [151] for C_3H_8.

Table 9.2: Experimental density of single gas phase points shown in Figure 9.5

T/K	p/MPa	$^{\dagger}\rho$ (expt.)	$^{\S}\rho$(expt.)
		mol·cm^{-3}	mol·cm^{-3}
343.48	7.025	0.004518	0.004428
340.07	5.706	0.003271	0.003224
338.64	5.386	0.003006	0.002967
336.73	4.995	0.002710	0.002679
334.27	4.614	0.002442	0.002416
332.18	4.303	0.002235	0.002214
329.11	3.937	0.002004	0.001987
325.96	3.686	0.001870	0.001856
323.9	3.399	0.001688	0.001676
318.4	2.925	0.001433	0.001425

† inferred from Schmidt and Moldover [134] based on Oster mixing rule [137].

§ inferred from Harvey and Prausnitz [138].

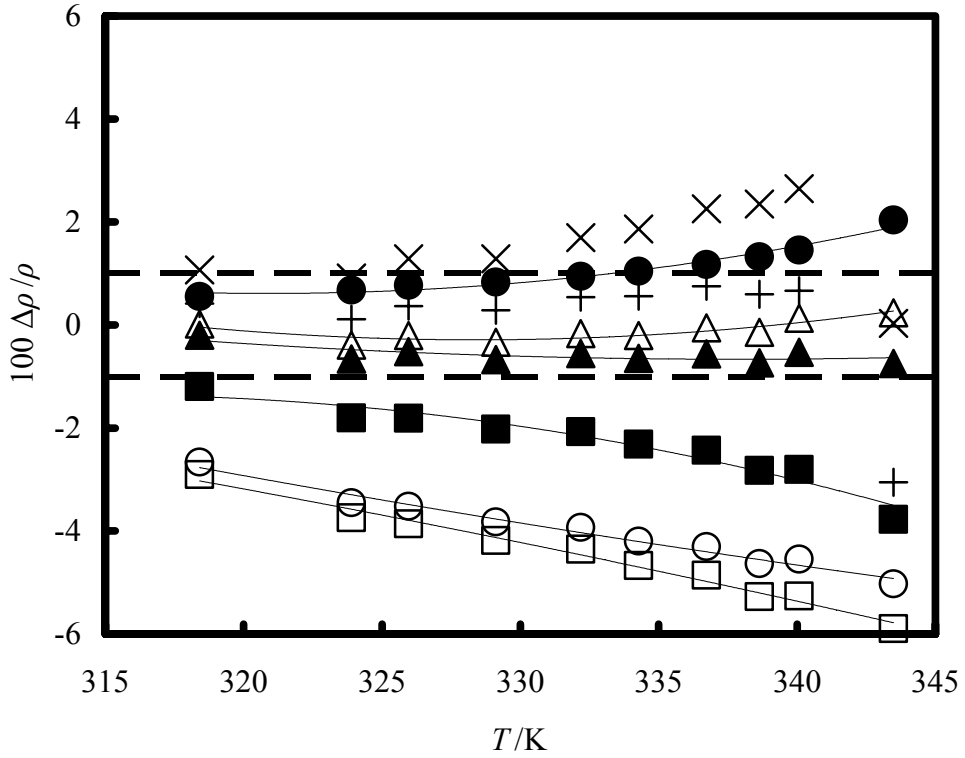

Figure 9.6: Fractional deviations $\Delta\rho/\rho = \{\rho(\text{expt.}) - \rho(\text{calc.})\}/\rho(\text{calc.})$ of the experimentally determined density ρ(expt.) with parameters from [134] based on Oster mixing rule [137] from that calculated with: □, the Peng-Robinson equation of state with $k_{ij} = 0$ as implemented within the software package HYSYS; ○, Peng-Robinson equation of state with $k_{ij} = 0.012$ as implemented within the software package HYSYS; ■, NIST standard reference database REFPROP [131]; ▲, Soave-Redlich-Kwong equation of state with $k_{ij} = 0$ as implemented within the software package HYSYS; △, Soave-Redlich-Kwong equation of state with $k_{ij} = 0.012$; ●, correlation with dielectric constant based on Harvey and Prausnitz mixing rule [138]; X, generalized corresponding state model based on the crossover cubic (Patel-Teja) EOS with $k_{ij} = -0.03606$ as reported by Kiselev [152]; +, generalized corresponding state model based on the crossover cubic (Patel-Teja) EOS with $k_{ij} = -0.04113$ as reported by Kiselev [152].

As shown in Figure 9.6, the fractional deviation from the EOS increases as temperature increases from (318 to 343) K. Densities calculated from the PR EOS with the binary interaction parameter k_{ij} = 0, as implemented within the software package HYSYS, gave the largest deviations from the experimental results which extended from (-2.7 to -6) %. The NIST standard database REFPROP [131] gave a smaller deviation (-1 to -3) % and the Harvey and Prausnitz correlation [138] gave (0.6 to 2) %. The Soave-Redlich-Kwong equation of state with k_{ij} = 0 or 0.012 gave deviations less than 0.6 %.

The density for these points was also calculated with the generalized corresponding state model, based on the crossover cubic (Patel-Teja) equation of state by Kiselev et al. [152, 153, 154], with binary interaction parameter k_{ij} = - 0.04113 and the deviations were < 0.7 % for all the points except at T = 343 K, where the deviation was about - 3 %.

9.3 Liquid volume fraction (LVF) results:

9.3.1 Cavity calibration for liquid volumes:

The liquid volume fraction was determined for 16 points in the 2-phase region (liquid + gas) from the knowledge of the normalised function $\epsilon = [\varepsilon - \varepsilon(g)]/[\varepsilon(l) - \varepsilon(g)]$ where ε was the measured relative permittivity for the mixture, $\varepsilon(g)$ the relative permittivity at saturated gas, and $\varepsilon(l)$ the relative permittivity at saturated liquid at the same temperature.

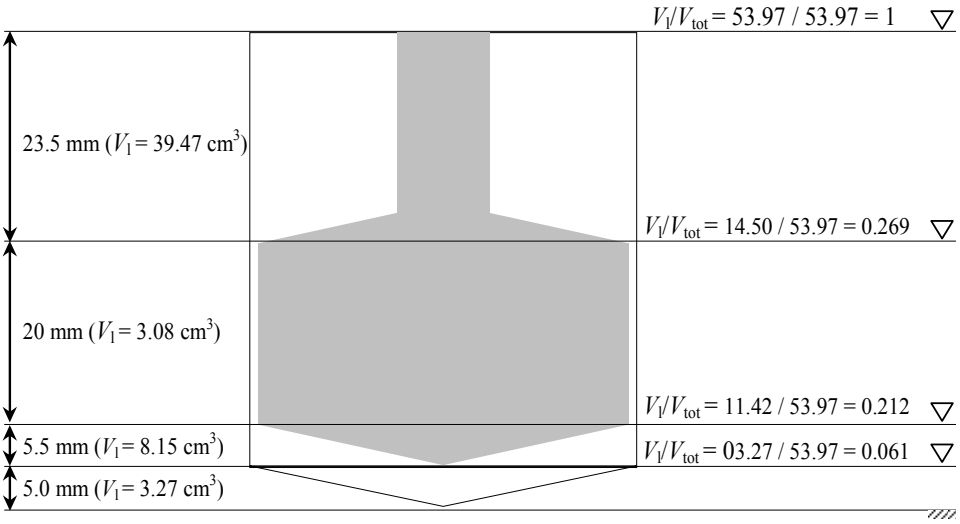

Figure 9.7: Liquid volumes V_l and corresponding liquid volume fractions V_l/V_{tot} at different sections in the cavity.

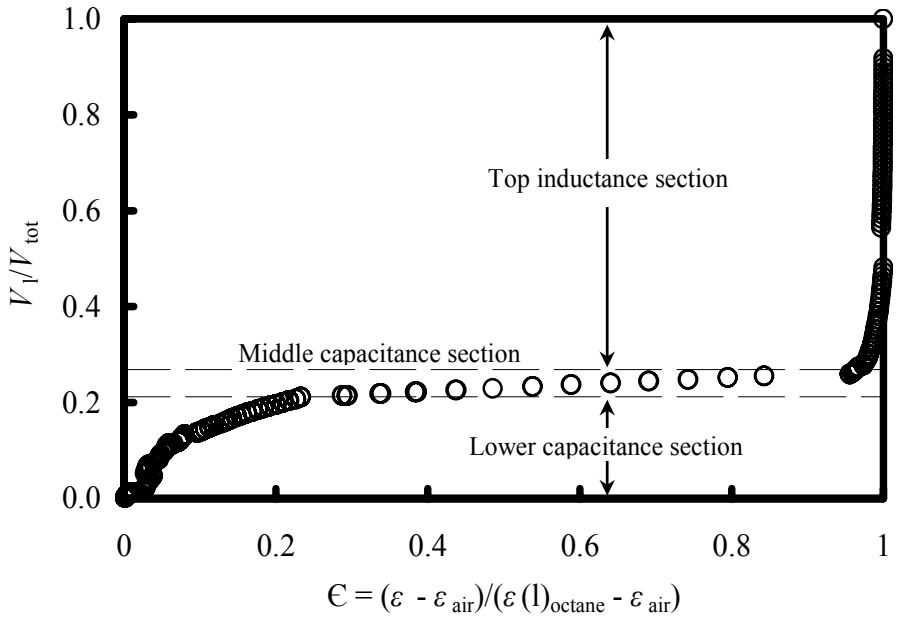

Figure 9.8: Calibration for liquid volume fractions inside the cavity using liquid octane for range V_l/V_{tot} = (0 to 1) shown in Figure 9.7, with lower capacitance section enlarged in Figure 9.9 with data fit to best trend lines.

The relationship between the function Є and the liquid volume fractions was determined from calibration with pure liquid octane at room temperature taking ε(g) for air = 1.0008, and ε(l) for liquid C_8H_{18} = 1.9476 from ref [155], where the change in the relative permittivity was measured at different octane liquid level in the cavity as shown in Figure 9.8.

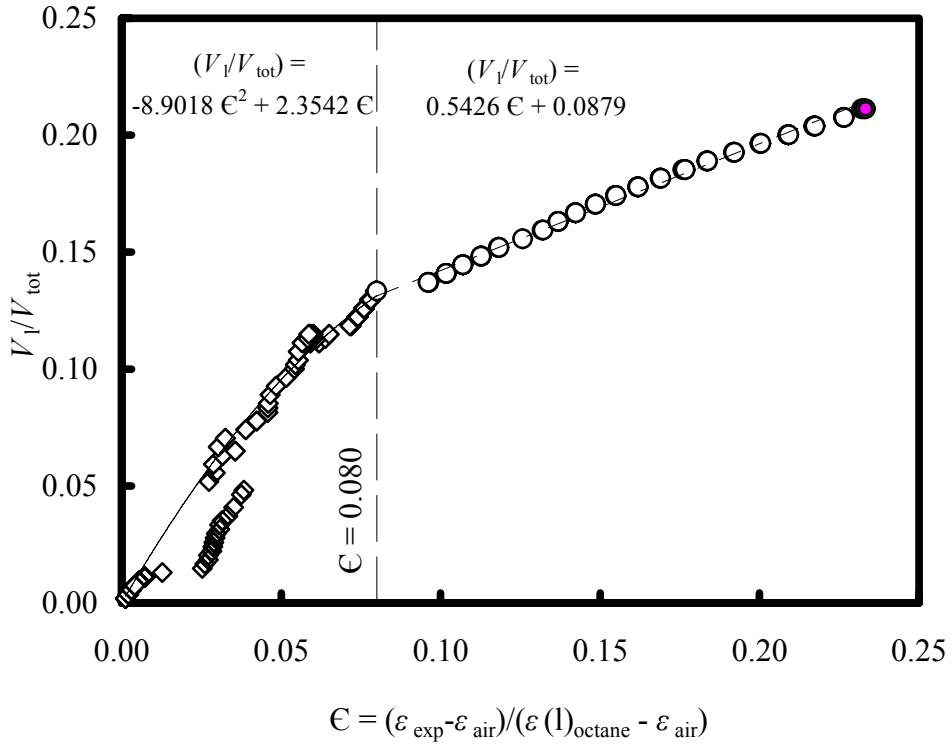

Figure 9.9: Calibration for liquid volume fractions in the lower capacitance section with range V_l/V_{tot} = (0 to 0.212) shown in Figure 9.7, divided into 2 data sets to obtain a better fit.

The rate of change of the function Є in the lower capacitance section has been enlarged in the close up Figure 9.9, and has been divided into 2 different trends

to allow the determination of V_l/V_{tot} from the best fit with calibration data of octane. Thus, as shown in Figure 9.9, $V_l/V_{tot} = -8.9018\ Є^2 + 2.3542\ Є$, for $Є < 0.08$; and $V_l/V_{tot} = 0.5426\ Є + 0.0879$, for $Є \geq 0.08$.

A discontinuity that starts at $V_l/V_{tot} \approx 0.015$ and stops at $V_l/V_{tot} \approx 0.066$ was noticed as shown in Figure 9.9. This discontinuity was observed in four different repeated calibrations. That persistent behaviour is postulated to be attributed to the surface tension effect at the contact point between the liquid and the tip of the bulb, which can occur when the fluid drains into the bottom of the cavity. That effect starts when the liquid level = 3 mm ($V_l/V_{tot} \approx 0.015$) i.e. very close to the tip, and stops at a liquid level = 5 mm ($V_l/V_{tot} \approx 0.066$) i.e. when the liquid becomes in contact touching with the tip of the bulb as shown in Figure 9.7.

9.3.2 The selection of the points:

Owing to the isochoric nature of this experiment, isotherms were plotted, as shown in Figure 9.10, and the selected points were located at the intersection with the isochore lines. However, the number of the points on each isotherm is not sufficient to use one of the points to correct $\varepsilon(l)$ for the rest of the points on the same isotherm (only 2 points). Thus, a correlation was used to calculate $\varepsilon(l)$, while $\varepsilon(g)$ was obtained from the measured relative permittivity at the dew points except for the two points, shown in Figure 9.10 at (311.21 and 316.46)

K, ε(g) was calculated using the Harvey and Prausnitz correlation [138,139]. No points could be selected at a temperature higher than the critical temperature (336.3 K) where saturated liquid data cannot be determined.

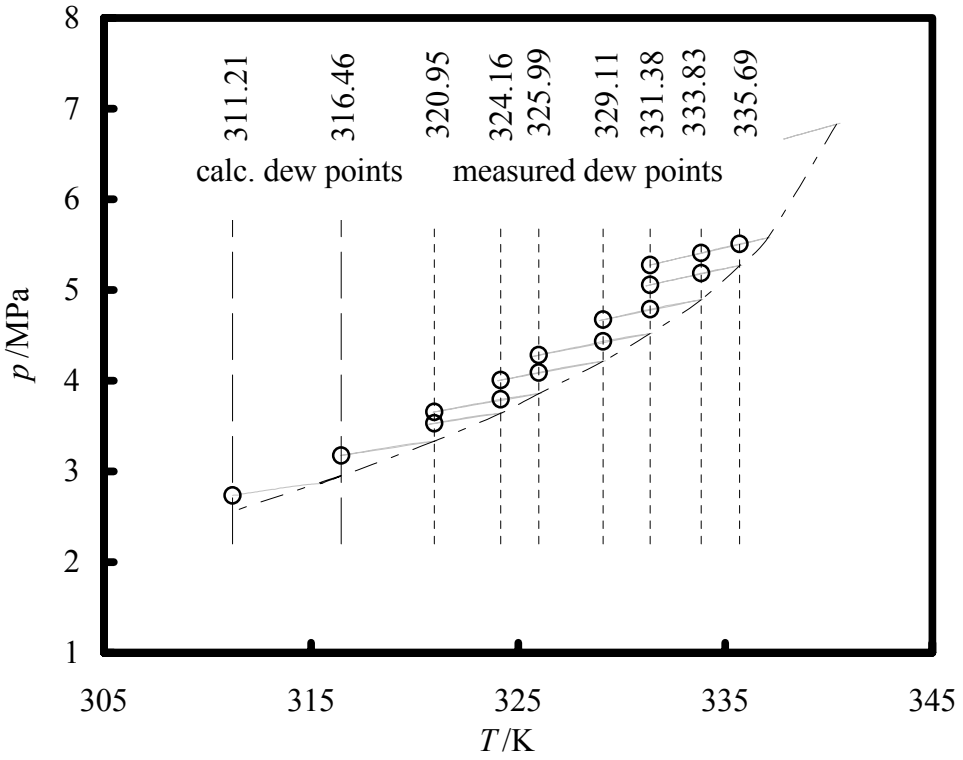

Figure 9.10: Graph showing the selected points for which the dew points were measured, hence, its corresponding relative permittivity was determined at, ─ · ─, saturated gas line, ──, isochore lines; ○, selected points; vertical dashed lines: isotherms at dew temperatures.

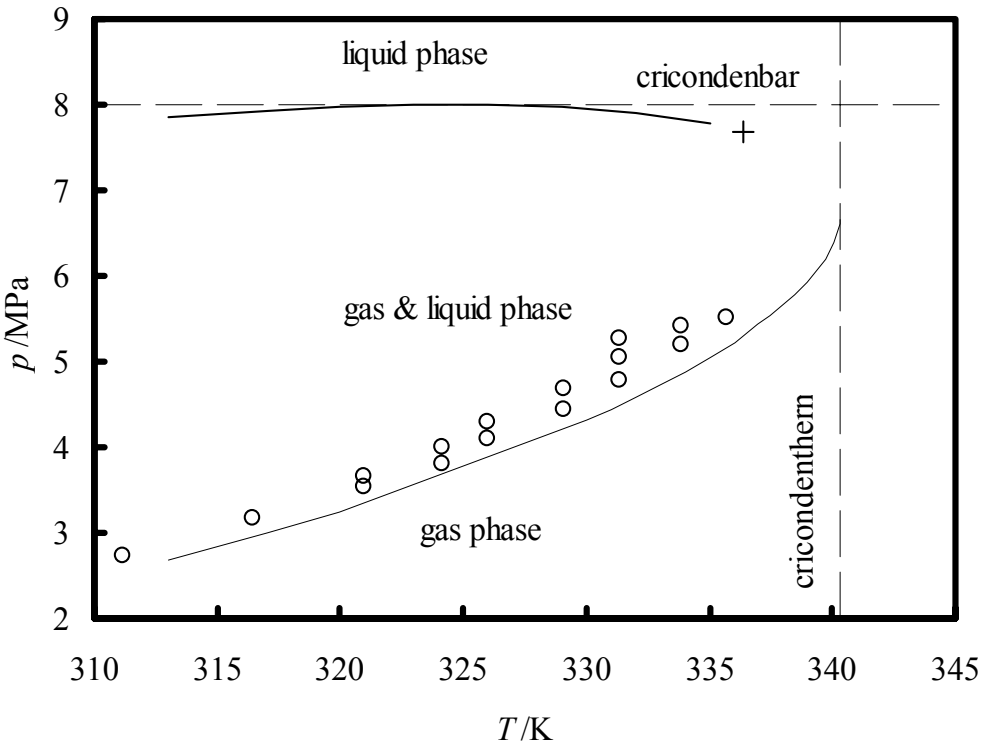

Figure 9.11: Graph showing the points at which the liquid volume fraction was determined in the co-existing phase region (gas + liquid) shown as circles (○); +, critical point.

9.3.3 Values of ε(l) *and* ε(g)

The relative permittivity of saturated liquid state ε(l) was calculated using two methods; REFPROP [131]; and the correlations of Harvey and Prausnitz [138]. As shown in Figure 9.12, REFPROP [131] failed to calculate ε(l) at 335.69 K and 331.38 K, and for the rest of the points, it gave values less than that calculated with Harvey and Prausnitz [138]. However, there was good agreement between ε(g) calculated with REFPROP [131] and that calculated from Harvey and Prausnitz [138] and with the measured values as shown in

Figure 9.12. Relative deviations of ε(g) increase from 0.1 to 1 % as the temperature increases to the critical region as shown in Figure 9.13.

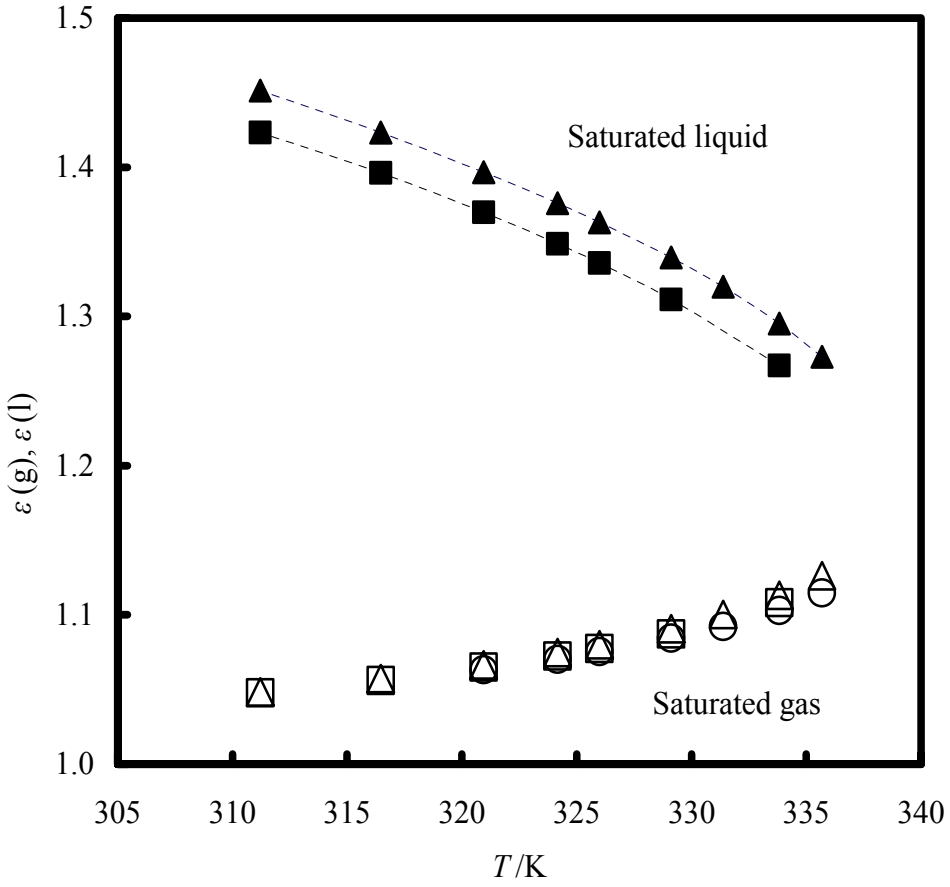

Figure 9.12: Relative permittivity at saturated gas ε(g), and saturated liquid ε(l): ▲, ε(l) calculated with equations from [138]; ■, ε(l) calculated with REFPROP [131] (failed at 331.38 and 335.69 K); △, ε(g) calculated with [138]; □, ε(g) calculated with REFPROP [131]; ○, ε(g) measured experimentally in this work.

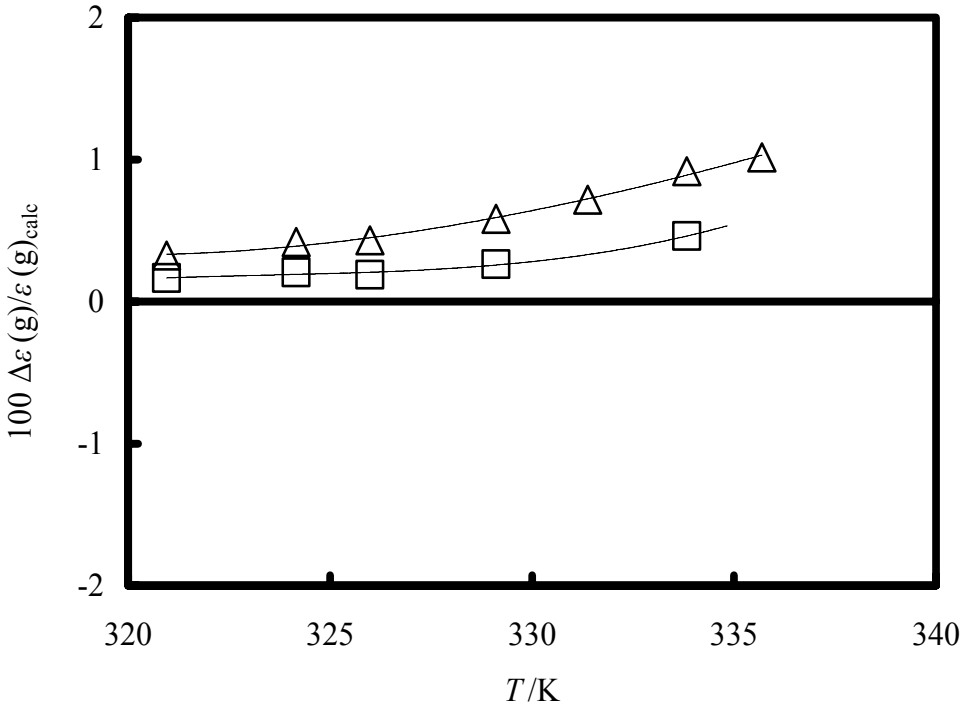

Figure 9.13: Fractional deviations between experimental and calculated $\Delta\varepsilon(g)/\varepsilon(g)_{calc}$ with $\{\Delta\varepsilon(g) = \varepsilon(g)_{calc} - \varepsilon(g)_{exp}\}$ for: △, calculated with [138]; □, calculated with REFPROP [131].

9.3.4 Deviation of liquid volume fractions from EOS:

The liquid volume fractions were determined from experimental measurements of the relative permittivity and compared with that calculated from the Peng-Robinson equation of state and Soave-Redlich-Kwong equation of state. As shown in Figure 9.14, the deviations increase from (0 to 8) % as the temperature increases from (331 to 335) K, the deviations from Soave-Redlich-Kwong equation of state are less than those from the Peng-Robinson equation of state.

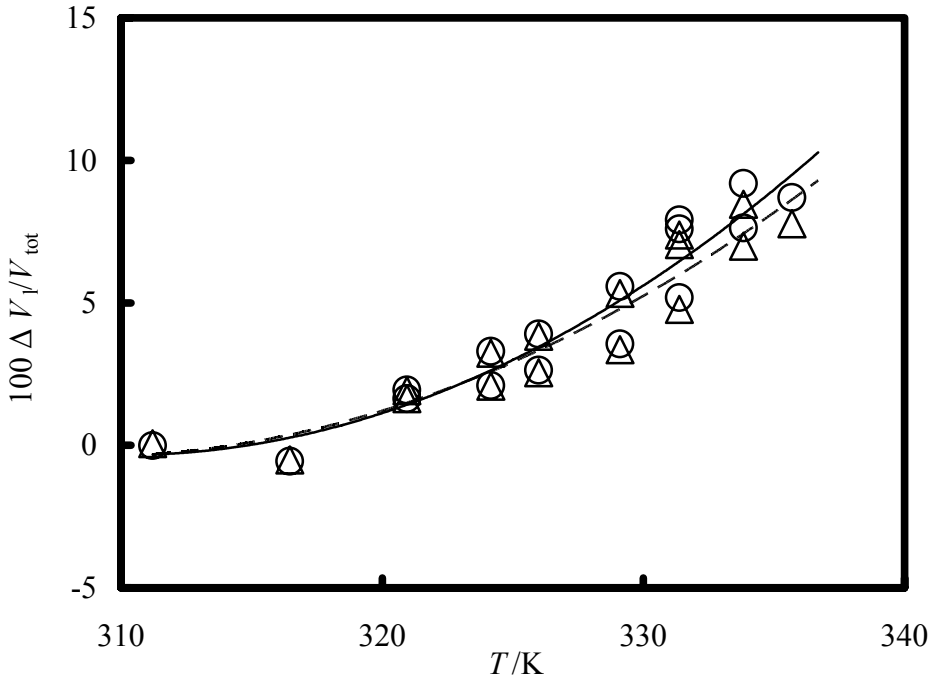

Figure 9.14: Deviation between experimental liquid volume fraction $\Delta V_l/V_{tot} = \{V_l(\text{expt.}) - V_l(\text{EOS})\}/V_{tot}$ (as a function of temperature) from calculated with: ○, Peng-Robinson EOS ($k_{ij} = 0.0$) as implemented within the software package HYSYS; △, Soave-Redlich-Kwong EOS ($k_{ij} = 0.0$) as implemented within the software package HYSYS; ──, mean deviations with Peng-Robinson EOS; ——, mean deviation with Soave-Redlich-Kwong EOS.

Results are also shown on Figure 9.15, as function of $\{\varepsilon - \varepsilon(g)\}$ which indicate how far the points are from the saturated gas line. As shown in Figure 9.15, the deviation increases as one moves further from the saturated gas line and gets closer to the saturated liquid line, i.e., as the liquid volume increases.

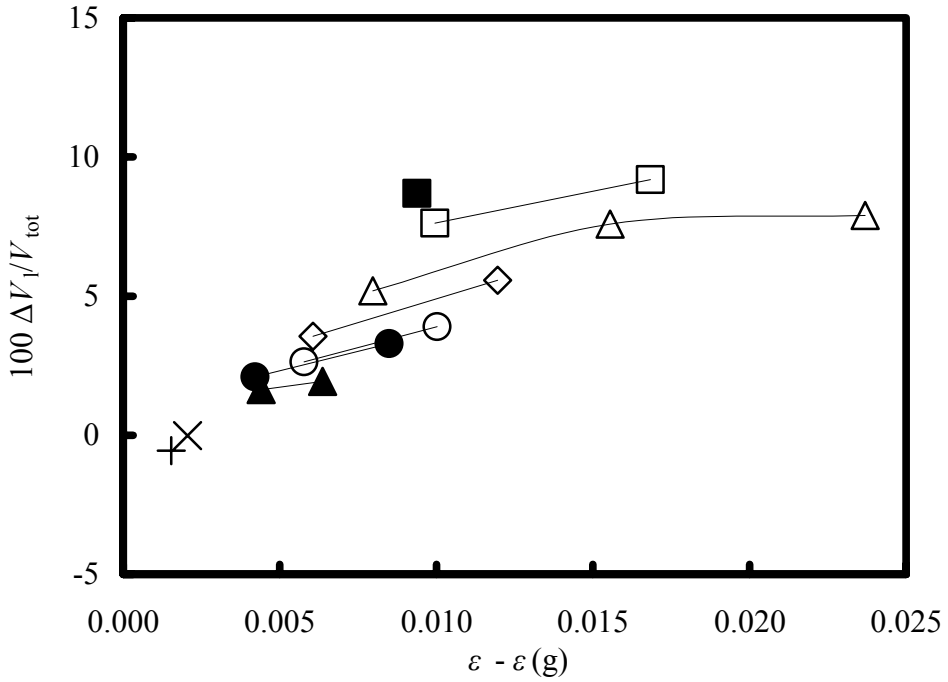

Figure 9.15: Deviation between experimental liquid volume fraction $\Delta V_l/V_{tot}$ = $\{V_l(\text{expt.}) - V_l(\text{EOS})\}/V_{tot}$ as a function of $\{\varepsilon - \varepsilon(g)\}$, calculated with Peng-Robinson EOS with $k_{ij} = 0.00$ as implemented within the software package HYSYS, X, 311.21 K; +, 316.46 K; ▲, 320.95 K; ●, 324.16 K; ○, 325.99 K; ◇, 329.11 K; △, 331.38 K; □, 333.83 K; ■, 335.69 K.

9.3.5 Minimum detectable liquid volume:

A liquid volume increment of 0.1 cm^3 was used during the calibration of the cavity with liquid octane which is equivalent to a liquid volume fraction of V_l/V_{tot} = 0.002 (that is 0.2 %), however, the cavity resonator is sensitive to liquid fractions less than that amount. The minimum detectable liquid volume fraction (detection threshold) can be determined from the resolution of the resonance frequency that is required to distinguish between two points at the

onset of condensation, or more precisely, the uncertainty of the measurements of the resonance frequency f_r at these point. At the start of the liquid volume formation in the lower section in the cavity, the gradient $dV_l/df_r \approx 0.6$, as shown in Figure 9.16, and is almost a linear function of f_r where the liquid volume increased to about 0.5 cm^3. The uncertainty in the resonance frequency was estimated as $\delta f_r < 0.005$ MHz ($k = 2$), hence, the minimum volume that can be detected is ≈ 0.003 cm^3 for which the detectable liquid volume fraction V_l/V_{tot} is better than $1 \cdot 10^{-4}$ (that is 0.01 %).

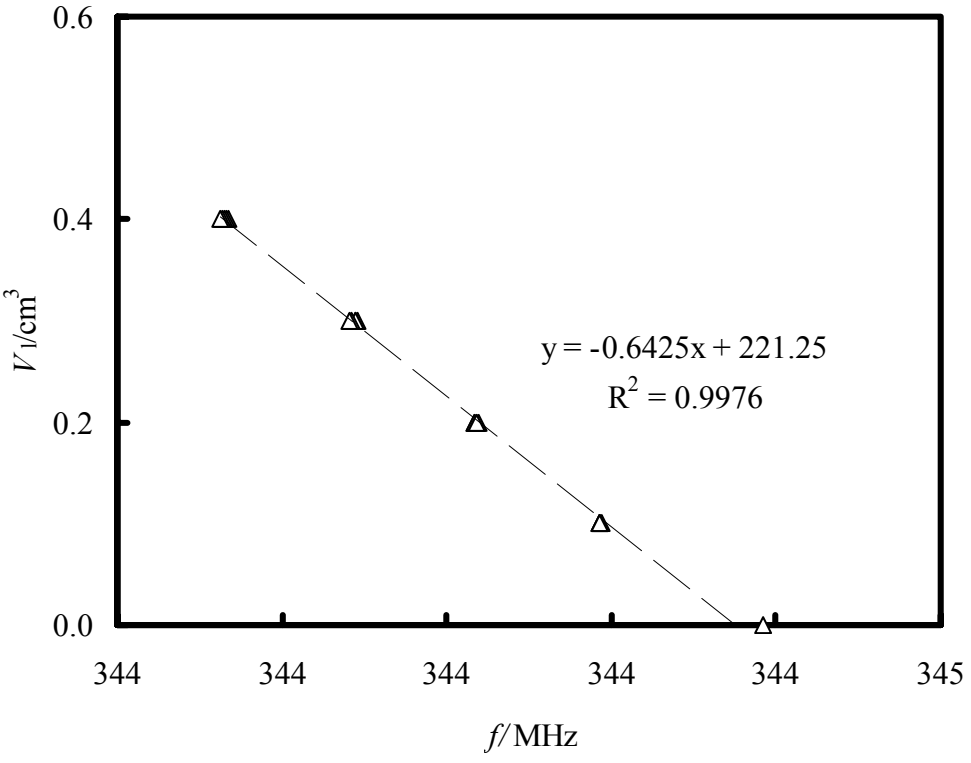

Figure 9.16: Liquid volume as function of resonance frequency measured at the first five points in the calibration with octane.

At this minimum liquid volume, the liquid level in the cavity was estimated as 0.5 mm which is about 500 times the surface roughness of the cavity. That ensures that there will be no effect from an uneven distribution of the liquid that would occur if the liquid level approaches the height of surface roughness. Furthermore, the open conical space at the bottom of the cavity reduces the possibility of inclusion of any gases that could be trapped within micro well constructions introduced in other cavities.

Part III

Conclusions and Recommendations

References and Bibliography

Chapter 10

CONCLUSIONS AND RECOMMENDATIONS

The vibrating wire viscometer and the microwave resonator, developed in this work, have been proven to provide accurate measurements of viscosity, phase boundaries, gas phase density, and volume of liquid formed in the two phase envelope.

The vibrating wire viscometer can operate remotely and is of a robust construction. The size of the wire assembly is small relative to most other vibrating wire viscometers which allow the study of high value fluids with minimal cost. The material used in making the wire holding tube was Macor® which has a linear thermal expansion coefficient about 4 times that of tungsten at T = 298 K. However, using a material with a thermal expansion coefficient similar to tungsten, such as Shapal-M®, will decrease the uncertainty in viscosity measurements ($\delta\eta$ = ± 1 %) resulting from the change in the wire tension.

The well-defined working equations for the vibrating wire viscometer are the basis for the accurate measurements with this apparatus. We found allowing f_0, the resonance frequency in vacuum, to float in the regression is important for

the accurate determination of viscosity and was included in the analysis of this work.

The wire radius was the most significant design parameter, adding about ± 2 % to the uncertainty in the viscosity from only a variation of ± 1 % in the wire radius. This sensitivity of viscosity to the uncertainty in the wire radius was the same at $\eta \approx 0.5$ mPa·s and at $\eta \approx 200$ mPa·s supporting the assumption that the wire radius is independent of the viscosity of the fluid used for its calibration.

Results obtained with the 0.15 mm diameter vibrating wire for viscosities covered the range from (0.3 to 100) mPa·s with an uncertainty of < 0.6 % and differed from literature values by < 1 %. As anticipated from the working equations, measurements showed that increasing the wire diameter to 0.150 mm allowed the measurements to be performed with fluids of viscosities up to 200 mPa·s with values within 2 % of the reference values. This difference is within the uncertainty of the measurement, which, at $\eta \approx 200$ mPa·s, was estimated as about 3 %. A recommended limit for this viscometer is 150 mPa·s with an estimated uncertainty of about 2 %.

With the 0.15 mm diameter wire, a quality factor $Q \approx 2$ was observed at $\eta \approx$ 200 mPa·s. Higher quality factor can be obtained by increasing the diameter of the wire providing the radius to the length ratio is maintained at $R/L \approx 0.001$. During the course of this work, a wire of diameter 0.2 mm was tried, but with

the same length of 40 mm. This wire gave a quality factor of 2.7 at $\eta \approx 250$ mPa·s. In order to increase the upper limit of viscosity measurements, while maintaining an acceptable uncertainty of < ± 2 %, the length of the wire and the length of magnet blocks, and, consequently, the container diameter must be increased. This is a subject for future study with a vibrating wire of diameter, perhaps, 1 mm, and possibly with different surface roughness.

The microwave cavity resonator, similar to a design reported in the literature, provided accurate measurements of the dew points, gas phase density and, in particular, has been shown to be sensitive enough to measure liquid drop out volumes accurately. The design of the magnetic pump and its location inside the heat bath significantly reduced dead volumes within the system, and provided smooth and reliable fluid circulation and mixing.

The model proposed and used to determine the resonance frequency from the measurements of the microwave forward transmission coefficient $\boldsymbol{S}_{21}$ is simpler, and more accurate than previous models. The relative permittivity was determined, with a relative uncertainty of about ± 0.01 % ($\delta\varepsilon \approx \pm 1 \cdot 10^{-4}$), from the measurements of the resonance frequency.

Accurate measurements on $\{0.4026CH_4 + 0.5974C_3H_8\}$ were obtained and compared with experimental data from literature and values calculated with

different CEOS using different software packages. Generally, the deviations increase as the temperature approaches the critical region.

The dew pressures p^d at the temperature range (315 and 337) K, calculated with Peng-Robinson cubic equation of state (using both SPECS and HYSYS), all lie within the estimated expanded uncertainty of the experimental measurements between (0.5 and 0.9) %. The p^d predicted (in the same temperature range) by NIST 14 differ from PR SPECS by between (0.67 and 0.96) %, while the Soave Redlich Kwong equation of state provides SRK estimates (using both SPECS and HYSYS) that differ from PR SPECS by 0.4 % at T = 315 K, and -2.5 % at T = 337 K.

The dew pressure calculations performed with SPECS failed to provide a dew pressure at T > 339.2 K for both PR and SRK, while for HYSYS the highest temperature at which a dew-point could be determined was 340.35 K with SRK, which is just 0.03 K below our highest temperature. According to SRK HYSYS, this value is the cricondentherm. However, the dew pressure estimated at this point (T = 340.35 K) from SRK HYSYS, was 6.69 MPa which is lower than the experimental value (where T = 340.38 K) by 0.14 MPa (≈ 2 %) which is about a factor of 4 greater than the estimated expanded uncertainty of measurements at that point (≈ 0.5 %).

The p^d measured at T = (329.11, 331.38 K, and 333.83 K) differed by less than 0.5 % from other experimental values reported in the literature, all within the uncertainty of measurements. However, the difference increases to ≈ 10 % as the temperature approaches the critical region at $T \approx 340$ K. This is perhaps because the p^d values reported in the literature were detected from discontinuities in the slope of isochoric (p,T) data that vanish at the cricondentherm and are small in the vicinity of it and near to criticality. Our results depended on discontinuities in the gradient of isochoric (ρ, T), which are increasingly easy to detect in the region near the cricondentherm.

Densities were inferred from relative permittivity measurements in the gas phase at the temperature range (318 to 343) K. Calculation with the PR gave the largest deviations from the experimental results from (-2.7 to -6) %, the NIST standard database gave deviations of from (-1 to -3) %, and the SRK gave deviations of less than 0.6 %. The calculations with the Harvey and Prausnitz correlation (based on a mixture reduced density) gave deviations of from (0.6 to 2) %. Density was also calculated with Kiselev and Ely parametric crossover equation of state (based on Patel-Teja EOS) with deviations of < 0.7 % for all the points except at T = 343 K, where the deviation was about -3 %.

Liquid volume fractions (V_l/V_{tot}) in the 2-phase region were measured from V_l ≈ (0.5 to 7) cm^3 in a total volume of $V_{tot} \approx 50$ cm^3 at different isochors. The experimental measurements differ from values obtained with the SRK by

between 0 and 3 % at $T < 326$ K, and about 8 % on approach to the critical region. The large deviations observed in the critical region were anticipated because of the known poor performance of the cubic equations of state with regard to the calculation of the liquid density in the vicinity of the critical temperature.

Liquid volume measurements also demonstrated the need for accurate data for relative permittivity along the saturated liquid line ε(l) especially near the critical region. This could be a subject for future study on liquid mixtures near the critical region.

The uncertainty in the mole fraction of the mixtures ($\delta x = \pm 13 \cdot 10^{-4}$) dominated the error in the determined (p, T) phase boundary. To decrease the uncertainty in the mole fraction either a balance with an uncertainty of ± 0.01 g should be used or a larger amount of mixture should be prepared.

Chapter 11

REFERENCES AND BIBLIOGRAPHY

[1] Kandil, M. E.; Marsh, K., N. Review of thermodynamic properties of refrigerants + lubricant oils, *Fluid Phase Equilib*., 199 (2002) 319–334.

[2] Kandil, M. E.; Marsh, K. N.; Goodwin, A. R. H., Vibrating Wire Viscometer with Wire Diameters of (0.05 and 0.15) mm: Results for Methylbenzene and Two Fluids with Nominal Viscosities at T = 298 K and p = 0.01 MPa of (14 and 232) mPa·s at Temperatures between (298 and 373) K and Pressures below 40 MPa, *J. Chem. Eng. Data*, 50 (2005) 647-655.

[3] Kandil, M. E.; Marsh, K. N.; Goodwin, A. R. H. A re-entrant resonator for the measurement of phase boundaries: dew points for {0.4026CH4 + 0.5974C3H8}, *J. Chem. Thermodyn*., 37 (2005) 684–691.

[4] Wakeham, W. A.; Nagashima, A.; Sengers, J. V., Eds. Measurement of the Transport Properties of Fluids, Blackwell Scientific Publications for IUPAC, Oxford, U.K. (1991) 8-110.

[5] Holland F. A., Bragg R. Fluid Flow for Chemical Engineers, 2nd ed., Edward Arnold, London (1995) 48-55.

[6] Assael, M. J.; Dymond J. H.; Papadaki, M.; Patterson, P. M. Correlation and prediction of dense fluid transport coefficients I. *n*-Alkanes, *Int. J. Thermophys*., 13 (1992) 269-281.

[7] Assael, M. J.; Dymond, J. H.; Papadaki, M.; Patterson, P. M. Correlation and prediction of dense fluid transport coefficients. II. Simple molecular fluids. *Fluid Phase Equilib*., 75 (1992) 245-55.

[8] Assael, M. J.; Dymond, J. H.; Papadaki, M.; Patterson, P. M. Correlation and prediction of dense fluid transport coefficients. III. n-Alkane mixtures. *Int. J. Thermophys*., 13 (1992) 659-684.

[9] Assael, M. J.; Dymond, J. H.; Patterson, P. M. Correlation and prediction of dense fluid transport coefficients. IV. A note on diffusion. *Int. J. Thermophys*., 13 (1992) 729-733.

[10] Assael, M. J.; Dymond J. H.; Patterson, P. M. Correlation and prediction of dense fluid transport coefficients. V. Aromatic hydrocarbons, *Int. J. Thermophys*., 13 (1992) 895-905.

[11] Bessel, F. W. Untersuchungen über die Länge des einfachen Secundenpendels. Abh. Königliche Akad. Wiss. Berlin (1828).

[12] Du Buat., P. L. G. Principes d'hydraulique, Paris: L'imprimerie de monsieur (1779).

[13] Stokes, G. G. Mathematical and Physical Papers; Cambridge University Press: Cambridge, U.K. (1901).

[14] Retsina, T.; Richardson, S. M.; Wakeham, W. A. The theory of a vibrating-rod densimeter. *Appl. Sci. Res*., 43 (1986) 127-158.

[15] Retsina, T.; Richardson, S. M.; Wakeham, W. A. The theory of a vibrating-rod viscometer. *Appl. Sci. Res*., 43 (1987) 325-346.

[16] Assael, M. J.; Dalaouti, N. K.; Vesovic, V. Viscosity of natural gas mixtures: measurements and prediction. *Int. J. Thermophys*., 22 (2001) 61-71.

[17] Assael, M. J.; Dalaouti, N. K.; Dymond, J. H. The viscosity of toluene in the temperature range 210 to 370 K. *Int. J. Thermophys*., 21 (2000) 291-299.

[18] Assael, M. J.; Dalaouti, N. K.; Polimatidou, S. The viscosity of toluene in the temperature range from 210 to 370 K at pressures up to 30 MPa. *Int. J. Thermophys*., 20 (1999) 1367-1377.

[19] Assael, M. J.; Oliveira, C. P.; Papadaki, M.; Wakeham, W. A. Vibrating-wire viscometers for liquids at high pressures. *Int. J. Thermophys*., 13 (1992) 593-615.

[20] Assael, M. J.; Wakeham, W. A. Vibrating-wire viscometery on liquids at high pressure. *Fluid Phase Equilib*., 75 (1992) 269-285.

[21] Assael, M. J.; Papadaki, M.; Dix, M.; Richardson, S. M.; Wakeham, W. A. An absolute vibrating-wire viscometer for liquids at high pressures. *Int. J. Thermophys*., 12 (1991) 231-244.

[22] Assael, M. J.; Papadaki, M.; Wakeham, W. A. Measurements of the viscosity of benzene, toluene, and m-xylene at pressure up to 80 MPa. *Int. J. Thermophys*., 12 (1991) 449-457.

[23] Assael, M. J.; Avelino, H. M. T.; Dalaouti, N. K.; Fareleira, J. M. N. A.; Harris, K. R. Reference Correlation for the Viscosity of Liquid Toluene from 213 to 373 K at Pressures to 250 MPa. *Int. J. Thermophys*., 22 (2001) 789-799.

[24] Assael, M. J.; Nagasaka, Y.; Nieto de Castro, C. A.; Perkins, R. A.; Strom, K.; Vogel, E.; Wakeham, W. A. Status of the round-robin on the transport properties of R134a. *Int. J. Thermophys*., 16 (1995) 63-78.

[25] Assael, M. J.; Leipertz, A.; MacPherson, E.; Nagasaka, Y.; Nieto de Castro, C. A.; Perkins, R. A.; Strom, K.; Vogel, E.; Wakeham, W. A. Transport property measurements on the IUPAC sample of 1,1,1,2-tetrafluoroethane (R134a). *Int. J. Thermophys*., 21 (2000) 1-22.

[26] Assael, M. J.; Papadaki, M.; Richardson, S. M.; Oliveira, C. M. B. P.; Wakeham, W. A. Vibrating-wire viscometery on liquid hydrocarbons at high pressure. *High Temp. - High Pressures*, 23 (1991) 561-568.

[27] Caetano, F. J. P.; Fareleira, J. M. N. A.; Oliveira, C. M. B. P.; Wakeham, W. A. The viscosity of Diisodecylphthalate, a potential standard of moderate viscosity. *Int. J. Thermophys*., 25 (2004) 1311-1322.

[28] Caetano, F. J. P.; Correia da Mata, J. L.; Fareleira, J. M. N. A.; Oliveira, C. M. B. P.; Wakeham, W. A. Viscosity measurements of liquid toluene at low temperatures using a dual vibrating-wire technique. *Int. J. Thermophys*., 25 (2004) 1-11.

[29] Caudwell, D. R.; Trusler, J. P. M.; Vesovic, V.; Wakeham, W. A. The viscosity and density of n-dodecane and n-octadecane at pressures up to 200 MPa, and temperatures up to 473 K. *Int. J. Thermophys*., 25 (2004) 1353-1366.

[30] Audonnet, F.; Padua, A. A. H. Viscosity and density of mixtures of methane and n-decane from 298 to 393 K and up to 75 MPa. *Fluid Phase Equilib*., 216 (2004) 235-244.

[31] Audonnet, F.; Padua, A. A. H. Density and viscosity of mixtures of n-hexane and 1-hexanol from 303 to 423 K up to 50 MPa. *Int. J. Thermophys*., 23 (2002) 1537-1550.

[32] Audonnet, F.; Padua, A. A. H. Simultaneous measurement of density and viscosity of n-pentane from 298 to 383 K and up to 100 MPa using a vibrating-wire instrument. *Fluid Phase Equilib*., 181 (2001) 147-161.

[33] Avelino, H. M. T.; Fareleira, J. M. N. A.; Wakeham, W. A. Simultaneous measurement of the density and viscosity of compressed liquid toluene. *Int. J. Thermophys*., 24 (2003) 323-336.

[34] Gourgouillon, D.; Avelino, H. M. N. T.; Fareleira, J. M. N. A.; Nunes da Ponte, M. Simultaneous viscosity and density measurement of supercritical CO2-saturated PEG 400. *J. Supercrit. Fluids*, 13 (1998) 177-185.

[35] Padua, A. A. H.; Fareleira, J. M. N. A.; Calado, J. C. G.; Wakeham, W. A. Density and viscosity measurements of 2,2,4-trimethylpentane (isooctane) from 198 K to 348 K and up to 100 MPa. *J. Chem. Eng. Data*, 41 (1996) 1488-1494.

[36] Padua, A. A. H.; Fareleira, J. M. N. A.; Calado, J. C. G.; Wakeham, W. A. Density and viscosity measurements of 1,1,1,2-tetrafluoroethane (HFC-134a) from 199 K to 298 K and up to 100 MPa. *J. Chem. Eng. Data*, 41 (1996) 731-735.

[37] Padua, A. A. H.; Fareleira, J. M. N. A.; Calado, J. C. G.; Wakeham, W. A. Validation of an accurate vibrating-wire densimeter: density and viscosity of liquids over wide ranges of temperature and pressure. *Int. J. Thermophys*., 17 (1996) 781-802.

[38] Padua, A.; Wakeham, W. A.; Wilhelm, J. The viscosity of liquid carbon dioxide. *Int. J. Thermophys*., 15 (1994) 767-777.

[39] Padua, A. A. H.; Fareleira, J. M. N. A.; Calado, J. C. G.; Wakeham, W. A. Electromechanical model for vibrating-wire instruments. *Rev. Sci. Instrum*., 69 (1998) 2392-2399.

[40] Correia da Mata, J. L. G.; Fareleira, J. M. N. A.; Oliveira, C. M. B. P.; Caetano, F. J. P.; Wakeham, W. A. A new instrument to perform simultaneous measurements of density and viscosity of fluids by a dual vibrating-wire technique. *High Temp. - High Pressures*, 33 (2001) 669-676.

[41] Oliveira, C. M. B. P.; Wakeham, W. A. The viscosity of R32 and R125 at saturation. *Int. J. Thermophys*., 14 (1993) 1131-1143.

[42] Oliveira, C. M. B. P.; Wakeham, W. A. Viscosity of R134a, R32, and R125 at saturation. *Int. J. Thermophys*. 20 (1999) 365-373.

[43] Oliveira, C. M. B. P.; Wakeham, W. A. The viscosity of five liquid hydrocarbons at pressures up to 250 MPa. *Int. J. Thermophys*. 13 (1992) 773-790.

[44] Oliveira, C. M. B. P.; Wakeham, W. A. The viscosity of liquid R134a. *Int. J. Thermophys*., 14 (1993) 33-44.

[45] Wilhelm, J.; Vogel, E. Viscosity Measurements on Gaseous Propane. *J. Chem. Eng. Data*, 46 (2001) 1467-1471.

[46] Wilhelm, J.; Vogel, E. Viscosity measurements on gaseous argon, krypton, and propane. *Int. J. Thermophys*., 21 (2000) 301-310.

[47] Wilhelm, J.; Vogel, E.; Lehmann, J. K.; Wakeham, W. A. A vibrating-wire viscometer for dilute and dense gases. *Int. J. Thermophys*., 19 (1998) 391-401.

[48] Charles, E.; Molenat, J.; Abachi, H.; Michel, J.; Malbrunot, P. The use of a vibrating wire viscometer in liquids. *J. Phys. E: Sci. Instrum*., 12 (1980) 829-835.

[49] Trappeniers, N. J.; Van Der Gulik, P. S.; Van Den Hoof, H. The viscosity of argon at very high pressure, up to the melting line. *Chem. Phys. Lett*., 70 (1980) 438-443.

[50] Van Der Gulik, P. S.; Mostert, R.; Van Den Berg, H. R. The viscosity of methane at 273 K up to 1 GPa. *Fluid Phase Equilib*., 79 (1992) 301-311.

[51] Van Der Gulik, P. S.; El Kharraz, M. The viscosity of liquid carbon dioxide. *Int. J. Thermophys*., 16 (1995) 145-153.

[52] Van Der Gulik, P. S.; Trappeniers, N. J. The viscosity of argon at high densities. *Physica A*, 135 (1986) 1-20.

[53] Van Der Gulik, P. S. The viscosity of the refrigerant 1,1-difluoroethane along the saturation line. *Int. J. Thermophys*., 14 (1993) 851-864.

[54] Van Der Gulik, P. S. Vibrating-Wire Viscometers. In Experimental Thermodynamics, Measurement of the Transport Properties of Fluids; Wakeham, W. A., Nagashima, A., Sengers, J. V., Eds.; Blackwell Scientific Publications for IUPAC: Oxford, U.K. (1991) 79-88.

[55] Mostert, R.; Van Der Gulik, P. S.; Van Den Berg, H. R. The working equation of a vibrating wire viscometer. *Physica A*, 156 (1989) 909-920.

[56] Mostert, R.; Van Der Gulik, P. S.; Van Den Berg, H. R. Comment on the experimental viscosity of argon at high densities. *Physica A*, 156 (1989) 921-923.

[57] Tough, J. T.; McCormick, W. D.; Dash, J. D. Viscosity of Liquid He II. *Phys. Rev*., 132 (1963) 2373-2378.

[58] Tough, J. T.; McCormick, W. D.; Dash, J. D. Vibrating wire viscometer. *Rev. Sci. Instrum*., 35 (1964) 1345-1348.

[59] Goodwin, J. M. The viscosity of pressurised 4He above the transition. *Physica*, 76 (1974) 177-180.

[60] Goodwin, J. M. A vibrating wire viscometer for measurements at elevated pressures. *J. Phys. E: Sci. Instrum*., 6 (1973) 452-456.

[61] Bruschi, L.; Santini, M. Vibrating wire viscometer. *Rev. Sci. Instrum*., 46 (1975) 1560-1568.

[62] Alvesalo, T. A.; Collan, H. K.; Loponen, M. T.; Veuro, M. C. Experimental determination of the viscosity and density of the normal component of superfluid 3He at the melting curve. *Phys. Rev. Lett*., 32 (1974) 981-985.

[63] Genta, G. Vibration of Structures and Machines, 2nd ed. Springer-Verlag, N.Y. (1992) 82-86.

[64] Timoshenko, S.; Young, D. H.; Weaver, W. Vibration Problems in Engineering, 3rd ed., Chapter 5, D. Van Nostrand, N.Y. (1955) 324-345.

[65] Cowper, G.R., The shear coefficient in Timoshenko's beam theory, *J. Appl. Mech*., 33 (1966) 335-340.

[66] Vyas, V.; Nautiyal, T. Excess molar volumes and isentropic compressibilities of binary liquid mixtures containing n-alkanes at 298.15 K. *Pramana*, 59 (2002) 663-670.

[67] Oliveira, C. M. B. P. Viscosity of liquid hydrocarbons at high pressure. Ph.D. Thesis, Imperial College of Science and Technology and Medicine, London (1991).

[68] Chen, S. S.; Wambsganss, M. W.; Jendrzejczyk, J. A. *Trans. ASME: J. Appl. Mech*., 43 (1976) 325-329.

[69] ASM Metals Handbook, 8th ed., American Society for Metals, vol. 1 (1961).

[70] Magnet Sales & Services Ltd, UK, http://www.magnetsales.co.uk.

[71] Goodwin, A. R. H.; Marsh, K. N.; and Wakeham, W. A., Measurements of the Thermodynamic Properties of Single Phases, Experimental Thermodynamics, vol. VI, Elsevier, Amsterdam (2003) pp 13.

[72] An equation developed by Professor ten Seldam, private communications with Dr. Peter S. van der Gulik, Van der Waals-Zeeman Institute, University of Amsterdam, Valckenierstr. 67, 1018 XE Amsterdam, Netherlands.

[73] Bevington, P. R., Data Reduction and Error Analysis for the Physical Sciences, McGraw-Hill, London (1992).

[74] Magee, J. W.; Bruno, T. J. Isochoric (p, r, T) Measurements for liquid toluene from 180 K to 400 K at pressures to 35 MPa. *J. Chem. Eng. Data*, 41 (1996) 900-905.

[75] Kashiwagi, H.; Hashimoto, T.; Tanaka, Y.; Kubota, H.; Makita, T. Thermal conductivity and density of toluene in the temperature range 273-373 K at pressures up to 250 MPa. *Int. J. Thermophys*., 3 (1982) 201-2015.

[76] Santos, F. J. V.; Nieto de Castro, C. A. New accurate data on the viscosity of toluene under high pressure. *High Temp. – High Pressures*, 25 (1993) 465-469.

[77] Kashiwagi, H.; Makita, T. Viscosity of twelve hydrocarbon liquids in the temperature range 298-348 K at pressures up to 110 MPa. *Int. J. Thermophys*., 3 (1982) 289-305.

[78] Harris, K. R.; Malhotra, R.; Woolf, L. A. Temperature and density dependence of the viscosity of octane and toluene. *J. Chem. Eng. Data*, 42 (1997) 1254-1260.

[79] Krall, A. H.; Sengers, J. V. Viscosity of liquid toluene at temperatures from 25 to 150 °C and at Pressures up to 30 MPa. *J. Chem. Eng. Data*, 37 (1992) 349-355.

[80] Froba, A. P.; Leipertz, A. Viscosity and surface tension of saturated toluene from surface light scattering (SLS). *Int. J. Thermophys*., 22 (2001) 41-59.

[81] Goodwin, R. D. Toluene thermophysical properties from 178 to 800 K at pressures to 1000 bar. *J. Phys. Chem. Ref. Data*, 18 (1989) 1565-1636.

[82] Harris, K. R. Temperature and Density Dependence of the viscosity of toluene. *J. Chem. Eng. Data*, 45 (2000) 893-897.

[83] Byers, C. H.; Williams, D. F. Viscosities of Pure Polyaromatic Hydrocarbons. *J. Chem. Eng. Data*, 32 (1987) 344-348.

[84] Dymond, J. H.; Robertson, J. Transport properties of nonelectrolyte liquid mixtures - VI. viscosimetric study of binary mixtures of hexafluorobenzene with aromatic hydrocarbons. *Int. J. Thermophys*., 6 (1985) 21-41.

[85] Dymond, J. H.; Awan, M. A.; Glen, N. F.; Isdale, J. D. Transport properties of nonelectrolyte liquid mixtures. VIII. Viscosity coefficients for toluene and for three mixtures of toluene + hexane from 25 to 100 °C at pressures up to 500 MPa. *Int. J. Thermophys*., 12 (1991) 275-287.

[86] Dymond, J. H.; Glen, N. F.; Isdale, J. D.; Pyda, M. The viscosity of liquid toluene at elevated pressures. *Int. J. Thermophys*., 16 (1995) 877-882.

[87] Et-Tahir, A.; Bond, C.; Lagourette, B.; Xans, P. Determination of the viscosity of various hydrocarbons and mixtures involving hydrocarbons versus temperature and pressure. A critical study of some representative models. *Int. J. Thermophys*., 16 (1995) 1309-1334.

[88] Goncalves, F. A.; Hamano, K.; Sengers, J. V.; Kestin, J. Viscosity of liquid toluene in the temperature range 25-75 °C. *Int. J. Thermophys*., 8 (1987) 641-647.

[89] Kaiser, B.; Laesecke, A.; Stelbrink, M. Measurements of the viscosity of liquid toluene in the temperature range 218-378 K. *Int. J. Thermophys*., 12 (1991) 289-306.

[90] Vieira dos Santos, F. J.; Nieto de Castro, C. A. Viscosity of toluene and benzene under high pressure. *Int. J. Thermophys*., 18 (1997) 367-378.

[91] Singh, R. P.; Sinha, C. P. Viscosities and activation energies of viscous flow of the binary mixtures of n-hexane with toluene, chlorobenzene, and 1-hexanol. *J. Chem. Eng. Data*, 29 (1984) 132- 135.

[92] Hammond, L. W.; Howard, K. S.; McAllister, R. A. Viscosities and densities of methanol-toluene solutions up to their normal boiling points. *J. Phys. Chem*., 62 (1958) 637-639.

[93] Dandekar, A. Y.; Stenby, E. H. Measurement of phase boundaries of hydrocarbon mixtures using fibre optical detection techniques. *Ind. Eng. Chem. Res*., 39 (2000) 2586–2591.

[94] Goodwin, A. R. H.; Froerup, M. D.; Stenby, E. H. Microwave detection of dew points: Results for complex mixtures. *J. Chem. Thermodyn*., 23 (1991) 713–715.

[95] Burfield, D. W.; Richardson, H. P.; Guereca, R. A. Vapour-liquid equilibria and dielectric constants for the helium-carbon dioxide system. *AIChE J*., 16 (1970) 97–100.

[96] Chan, M; Ryschkewitsch, H. P.; Meyer, H. The dielectric constant in liquid and solid ^{4}He. *J. Low Temp. Phys*., 26 (1977) 211–228.

[97] St-Arnaud, J. M.; Bose, T. K.; Okambawa, R.; Ingrain, D. Application of the dielectric constant measurements to study the influence of the small quantities of water vapour on the compressibility factor of methane. *Int. J. Thermophys*., 13 (1992) 685–697.

[98] Goodwin, A. R. H.; Mehl, J. B.; Moldover, M. R. Reentrant radio-frequency resonator for automated phase-equilibria and dielectric measurements in fluids. *Rev. Sci. Instrum*., 67 (1996) 4294–4304.

[99] Hamelin, J.; Mehl, J. B.; Moldover, M. R. Resonators for accurate dielectric measurements in conducting liquids. *Rev. Sci. Instrum*., 69 (1998) 255–260.

[100] Hamelin, J.; Mehl, J. B.; Moldover, M. R. The static dielectric constant of liquid water between 274 and 418 K near the saturated vapour pressure. *Int. J. Thermophys*., 19 (1998) 1359-1380.

[101] Anderson, G. S.; Miller, R. C.; Goodwin, A. R. H. Static dielectric constants for liquid water from 300 K to 350 K at pressures to 13 MPa using a new radio-frequency resonator. *J. Chem. Eng. Data*, 45 (2000) 549-554.

[102] Goodwin, A. R. H.; Mehl, J. B. Measurements of the dipole moments of seven partially fluorinated hydrocarbons with a radiofrequency re-entrant cavity resonator, Int. J. Thermophys., 18 (1997) 795-806.

[103] Goodwin, A. R. H.; Moldover, M. R. Phase border and density determinations in critical region of (carbon dioxide + ethane) determined from dielectric permittivity measurements. *J. Chem. Thermodyn*. 29 (1997) 1481–1494.

[104] May, E. F.; Edwards, T. J.; Mann, A. G.; Edwards, C. Dew point, liquid volume, and dielectric constant measurements in a vapour mixture of methane + propane using a microwave apparatus. *Int. J. Thermophys*., 24 (2003) 1509–1525.

[105] Peng, D-Y.; Robinson, D. B. A New Two-constant Equation of State. *Ind. Eng. Chem. Fundam*., 15 (1976) 59-64.

[106] Soave, G. Equilibrium Constants from a Modified Redlich-Kwong Equation of State. *Chem. Eng. Sci*., 27 (1972) 1197-1203.

[107] Twu, C. H.; Sim, W. D.; and Tassone, V. Getting a Handle on Advanced Cubic Equations of State. *Measurement & Control*, Aspen Technology Inc. Nov. (2002) 58-65.

[108] Reid, R. C.; Prausnitz, J. M.; Poling, P. E. The Properties of Gases and Liquids, 4th ed., McGraw-Hill, N.Y. (1986).

[109] Pitzer, K. S.; Lippmann, D. Z.; Curl, R.F.; Huggins, C. M.; Petersen, D. E. The Volumetric and Thermodynamic Properties of Fluids. II. Compressibility Factor, Vapor Pressure and Entropy of Vaporization. *J. Am. Chem. Soc*., 77 (1955) 3433.

[110] May, E. F.; Miller, R. C.; Shan, Z. Densities and dew points of vapour mixtures of methane + propane and methane + propane + hexane using a dual-Sinker densimeter. *J. Chem. Eng. Data*, 46 (2001) 1160–1166.

[111] Sage, B. H.; Lacey, W. N.; Schaafsma, J. G. Phase equilibria in hydrocarbon systems: II. methane-propane system. *Ind. Eng. Chem*., 26 (1934) 214–217.

[112] Reamer, H. H.; Sage, B. H.; Lacey, W. N. Phase equilibria in hydrocarbon systems: volumetric and phase behaviour of the methane-propane system. *Ind. Eng. Chem*., 42 (1950) 534–539.

[113] Price, A. R.; Kobayashi, R. K. Low temperature vapour-liquid equilibrium in light hydrocarbon mixtures: methane-ethane-propane system. *J. Chem. Eng. Data*, 4 (1959) 40–49.

[114] Roof, J. G.; Baron, J. D. Critical loci of binary mixtures of propane with methane, carbon dioxide, and nitrogen. *J. Chem. Eng. Data*, 12 (1967) 292–293.

[115] Wiese, H. C.; Reamer, H. H.; Sage, B. H. Phase equilibria in hydrocarbon systems: phase behaviour in the methane-propane-n-decane system. *J. Chem. Eng. Data*, 15 (1970) 75–82.

[116] Akers, W. W.; Burns, J. F.; Fairchild, W. K. Low-temperature phase equilibria: methane-propane system. *Ind. Eng. Chem*. 46 (1954) 2531–2535.

[117] Fröhlich, H., Theory of Dielectrics: dielectric constant and dielectric loss, 2nd ed., Clarendon Press, Oxford (1958).

[118] Böttcher, C. J. F. Theory of electric polarization, vol. 1, 2nd ed., Elsevier, N.Y. (1973).

[119] Marcuwitz, N. Waveguide Handbook, McGraw-Hill, N.Y. (1951) Sec. 5.27.

[120] Hamelin, J.; Mehl, J. B.; Moldover, M. R. Resonators for Accurate Dielectric Measurements in Conducting Liquids. *Rev. Sci. Instrum*., 69 (1998) 255-260.

[121] Hamelin, J. O.; Mehl, J. B.; Moldover, M. R. The Static Dielectric Constant of Liquid Water Between 274 and 418 K Near the Saturated Vapour Pressure. *Int. J. Thermophys*., 19 (1998) 1359-1370.

[122] Luiten, A. N. Wiley Encyclopaedia Elec. Electron. Eng. 17 (1999) 477–491.

[123] Dae-Hyun, H.; Young-Soo, K. Two port cavity Q measurement using scattering parameters. *Rev. Sci. Instrum*., 67 (1996) 2179-2181.

[124] Sanchez, M. C.; Martin, E.; and Zamarro, J. M. Unified and simplified treatment of techniques for characterising transmission, reflection or absorption resonators. *IEEE Proceedings*, 137 (1990) 209-212.

[125] Sanchez, M. C.; Martin, E.; Zamarro, J. M. New vectorial automation technique for characterisation of resonators. *IEEE Proceedings*, 137 (1989) 147-150.

[126] Frait, Z.; Patton, C. E. Simple method for microwave cavity *Q* determination. *Rev. Sci. Instrum*., 51(1980) 1092-1094.

[127] McKinstry, K. D.; Patton, C. E. Methods of determination of microwave cavity quality factors from equivalent electronic circuit models. *Rev. Sci. Instrum*., 60 (1989) 439-443.

[128] Kajfez, D.; Hwan, E. J. *Q*-factor measurements with a network analyser, IEEE Trans. on Microwave Theory and Techniques MTT, 32 (1984) 666-670.

[129] Bauccio, M., Ed. ASM Metals Reference Book, ASM International, Ohio (1993) pp 155.

[130] Moldover, M. R.; Buckley, T. J. Reference Values of the Dielectric Constant of Natural Gas Components Determined with a Cross Capacitor. *Int. J. Thermophys*. 22 (2001) 859-885.

[131] Lemmon, E. W.; McLinden, M. O.; Huber, M. L. Reference Fluid Thermodynamic and Transport Properties. NIST Standard Reference Database 23, Version 7.0, *Nat. Inst. Stands. Technol*., Gaithersburg, Maryland (2002).

[132] Setzmann, U.; Wagner, W. A New Equation of State and Tables of Thermodynamic Properties for Methane Covering the Range from the Melting

Line to 625 K at Pressures up to 1000 MPa. *J. Phys. Chem. Ref. Data*, 20 (1991) 1061-1151.

[133] Straty, G. C.; Goodwin, R. D. Dielectric constant and polarizability of saturated and compressed fluid methane. *Cryogenics*, 13 (1973) 712-715.

[134] Schmidt, J. W.; Moldover, M. R. Dielectric permittivity of eight gases measured with cross capacitors. *Int. J. Thermophys*., 24 (2003) 375-403.

[135] Trusler, J. P. M. Equation of state for gaseous propane determined from the speed of sound. *Int. J. Thermophys*., 18 (1997) 635-654.

[136] Muenter, J. S.; Laurie, V. W. Isotope effects on molecular dipole moments by microwave spectroscopy. *J. Chem. Phys*., 45 (1966) 855-858.

[137] Oster, G., The dielectric properties of liquid mixtures. *J. Am. Chem. Soc.*, 68 (1946) 2036-2041.

[138] Harvey, A. H.; Prausnitz, J. M. Dielectric constant of fluid mixtures over a wide range of temperature and density. *J. Solution Chem.*, 16 (1987) 857-869.

[139] Personal communication, Dr. Allan H. Harvey, Physical and Chemical Properties Division, National Institute of Standards and Technology, 325 Broadway, Boulder, Colorado 80305-3328, USA, (July 2005).

[140] Harvey, A. H.; Lemmon, E. W. Methods for the dielectric constant of natural gas mixtures. *Int. J. Thermophys*., 26 (2005) 31-46.

[141] Kirkwood, J.G. The Dielectric Polarization of Polar Liquids. *J. Chem. Phys*., 7 (1939) 911-919.

[142] Megyesy, E. F. Pressure vessel handbook, 13th ed., Pressure Vessel Publishing Inc., Tulsa, Okla. (2004).

[143] Bickford, J. H.; Nassar, S., Eds., Handbook of bolts and bolted joints, Parts III and IV, Marcel Dekker, NY (1998) 121- 423.

[144] Mansoorian, H.; Capps, E. F.; Gielen, H. L.; Eubank, P. T.; Hall, K. R. Compact, magnetic recirculating pump for wide-range temperature and pressure operation. *Rev. Sci. Instrum*., 46 (1975) 1350–1351.

[145] Ziger, D. H.; Eckert, C. A. Simple high-pressure magnetic pump. *Rev. Sci. Instrum*., 53 (1982) 1296–1297.

[146] Ruska, W. E. A.; Hurt, L. J.; Kobayashi, R. Circulating pump for high pressure and -200 to + 400 °C application. *Rev. Sci. Instrum*., 41 (1970) 1444–1446.

[147] Roger, W. J.; Fontalba, F.; Capps, E. F.; Holste, J. C.; Marsh, K. N.; Hall, K. R. Magnetic circulating pumps for use over wide ranges of temperature and pressure. *Rev. Sci. Instrum*., 59 (1988) 193–94.

[148] Hiza, M. J.; Duncan, A. G. A simple gas recirculation pump for low flow and high pressure applications. *Rev. Sci. Instrum*., 63 (1992) 5802–5803.

[149] Standard Reference Data Program, Fluid Mixtures Data Centre, Thermophysics Division, National Institute of Standards and Technology, Boulder, CO 80303.

[150] Lemmon, E. W.; Jacobsen, R. T. A generalized model for the thermodynamic properties of mixtures. *Int. J. Thermophys*., 20 (1999) 825–835.

[151] Miyamoto, H.; Watanabe, K. A thermodynamic property model for fluid-phase propane. *Int. J. Thermophys*., 21 (2000) 1045–1072.

[152] Personal communication, Dr. Sergei Kiselev, Research Associate Professor, Chemical Engineering Department, Colorado School of Mines, (November 2004).

[153] Kiselev, S. B.; Ely, J. F. Generalized corresponding state model for bulk and interfacial properties in pure fluids and fluid mixtures. *J. Chem. Phys*., 119 (2003) 8645-8662.

[154] Kiselev, S. B.; Rainwater, J. C. Extended law of corresponding states and thermodynamic properties of binary mixtures in beyond the critical region. 141 (1997) 129-154.

[155] Maryott, A. A.; Smith, E. R. Table of Dielectric Constants of Pure Liquids. National Bureau of Standards Circular, 514 (1951).

Appendix A

CALIBRATION DATA

A.1 Temperature calibration:

The temperature of the viscometer and the microwave cavity resonator was determined with two 4-wire industrial platinum resistance thermometers (PRT) of 25 Ω and 50 Ω respectively. These thermometers were calibrated against a 25 Ω standard platinum resistance thermometer (SPRT) made by Sensing Devices™ Ltd. UK. This SPRT had been calibrated, in 2000, on ITS-90 by the Measurement Standard Laboratory of New Zealand. The resistance of this SPRT at the triple point of water R (273.16 K) was re-determined, in 2002, as:

R (273.16 K) = (25.3928 ± 0.0003) Ω.

The temperature of the SPRT (T_{90}/K) was calculated based on its resistance R (273.16 K) and other fixed points included in its calibration certificate. Further information on the ITS-90 can be found in the reference: Preston-Tomas, H. *Metrologia*, 27 (1990) 3-10.

The three thermometers were inserted in an aluminium block, as shown in Figure A.1, to ensure stable and constant temperature during calibration. This block was placed in a calibration heat bath, controlled to 0.01 °C, and a

correlation was made between the actual temperature measured by the SPRT and the resistances of the thermometers under calibration at different temperatures in the range (0 to 170) °C. The data were fit to eq A.1 where the temperature t/°C was calculated from the measured resistance R/Ω as:

$$t = a_0 + a_1 R + a_2 R^2 \qquad \text{(A.1)}$$

Parameters of eq A.1 are included in Table A.1 and were optimised for a temperature range of $t \approx$ (0 to 150) °C. Deviations between the temperature measured with the standard platinum thermometer and that calculated with eq A.1 are shown in Figure A.2 and Figure A.3.

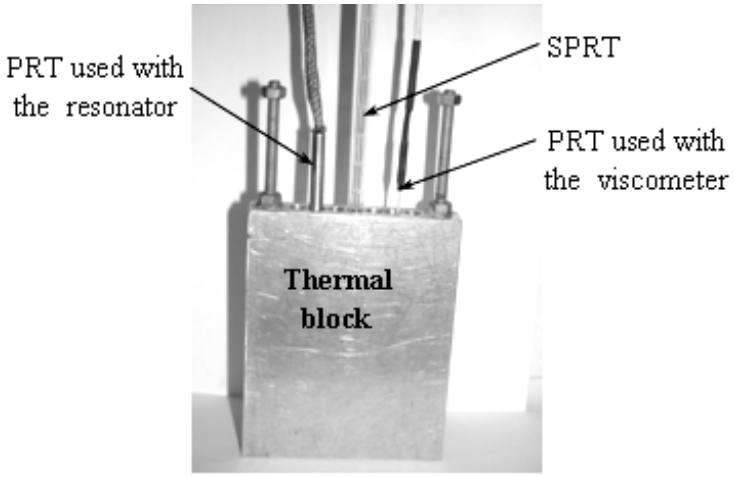

Figure A.1: Photo for the aluminium block with the SPRT (in the middle), the PRT used with the viscometer (to the right), and the PRT used with the cavity resonator (to the left).

Table A.1: Parameters for eq A.1 determined by least-squares for PRT# 1 (used with the viscometer) and PRT# 2 (used with the cavity resonator).

PRT#	a_0/°C	a_1/°C·Ω^{-1}	a_2/°C·Ω^{-2}	δt/°C
1	-240.9	8.9895	0.0156	± 0.01
2	-246.505	4.7125	0.0042	± 0.01

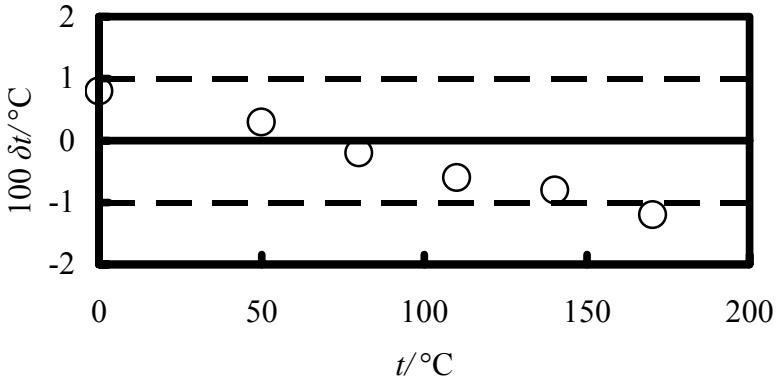

Figure A.2: Deviations between the temperature measured with the standard platinum thermometer and that calculated using eq A.1 with parameters from Table A.1 for the PRT#1 used with the viscometer.

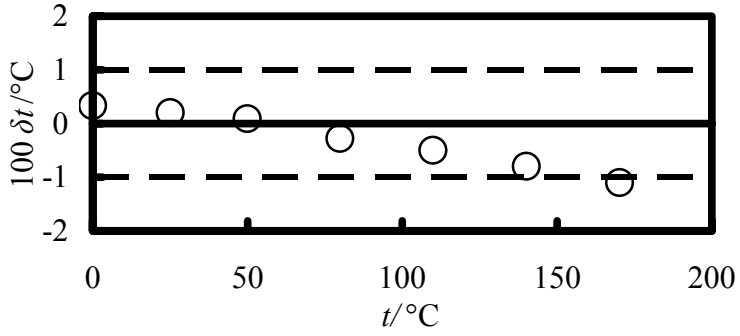

Figure A.3: Deviations between the temperature measured with the standard platinum thermometer and that calculated using eq A.1 with parameters from Table A.1 for the PRT#2 used with the microwave cavity resonator.

A.2 Pressure Calibration:

A differential pressure gauge (DPT), model Sensotec™ HL-Z/6917-02ZD-03, was used to measure the difference between the fluid pressure within the cavity and the pressure of a reference nitrogen line. The pressure of the reference nitrogen line was measured with a pressure transmitter, model Digiquartz™ 1000-2K, with an absolute pressure range (0 to 13.8) MPa, and an uncertainty ± 0.0014 MPa. The absolute pressure in the cavity resonator was calculated by adding the Sensotec DPT reading to the Digiquartz pressure reading.

The pressure calibration was performed using a liquid lubricated piston-cylinder (LLPC) dead-weight pressure gauge Desgranges et Huot Instruments, model DH-21000, with an uncertainty ± (0.0001p/MPa + 0.0005). The pressure was calibrated in the range (0.1 to 9) MPa, at temperature range (298 to 350) K to compensate for the temperature effects on the DPT, and also to offset and adjust the span of the nitrogen line pressure transmitter. Calibration parameters were obtained from a linear regression using a least square method.

A.2.1 Sensotec differential pressure calibration (DPT):

The dc output of the Sensotec DPT was measured over a differential pressure range from $\Delta p \approx$ (-3 to 3) MPa. A voltage source of 10 V dc was used for excitation, and an amplifier unit was used to amplify the output from about 2 mV to about 2 V. The data were fit to the following equation where the

differential pressure Δp/MPa was calculated from the measured output voltage V/V:

$$\Delta p = a_1 V + a_0 \quad \text{(A.2)}$$

Parameters of eq A.2 are included in Table A.12 and were optimised for a differential pressure range of $p_{(\text{differential})} \approx$ (-1 to 1) MPa. Deviations between the differential pressure measured with the standard pressure gauge and that calculated with eq A.2 are shown in Figure A.4.

Table A.2: Calibration parameters for the Sensotec differential pressure gauge included in eq A.2

a_0/MPa	a_1/MPa·V^{-1}	$\delta p_{(\text{differential})}$/MPa
0.0257	0.1229	± 0.003

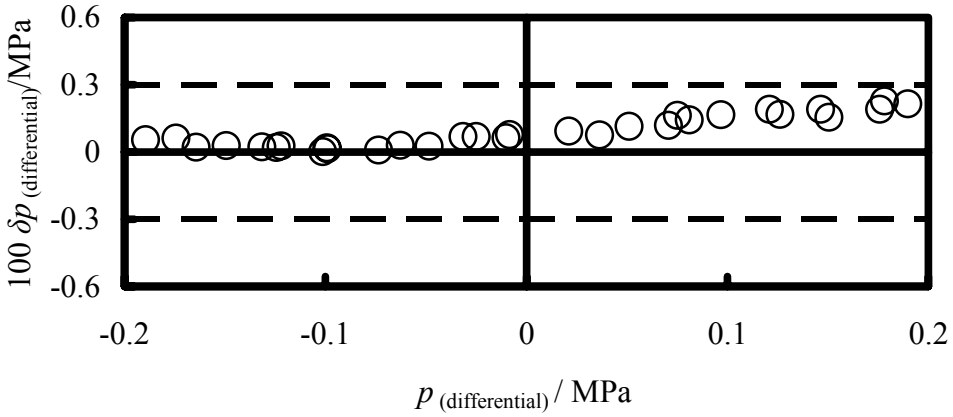

Figure A.4: Deviations between the pressure measured with the Sensotec differential pressure gauge and that calculated using eq A.2 with parameters from Table A.2.

A.2.2 Digiquartz pressure transmitter calibration:

The offset and the span of the Digiquartz pressure transmitter were adjusted after calibration over a pressure range of $p \approx$ (0.1 to 12) MPa. The pressure p (calculated with the original calibration coefficients) was adjusted using the pressure adder PA and multiplier PM obtained from best fit to eq A.3, and were entered in the Digiquartz software program. The values of the parameters PA and PM are included in Table A.3.

$$(p/\mathrm{MPa})_{\mathrm{adjusted}} = \mathrm{PM}\,(\,p/\mathrm{MPa} + \mathrm{PA}), \qquad \text{(A.3)}$$

Table A.3: Calibration parameters for the Digiquartz pressure transmitter included in eq A.3

PA	PM	δp/MPa
-0.26692	1.00026	± 0.0005

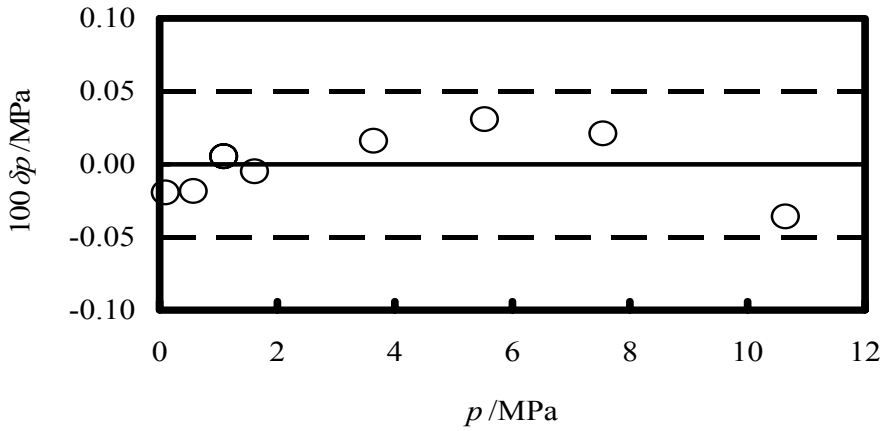

Figure A.5: Deviations between the pressure measured with the standard pressure gauge and that calculated using eq A.3 with parameters from Table A.3 for the Nitrogen line Digiquartz pressure gauge.